COBALT FERRITE PREPARED EMPLOYING POWDER TECHNOLOGY, THE POTENTIAL APPLICATIONS, THE PREPARATION AND CHARACTERISATION

By

MUSTAFA SAJJIA

Student ID: 56116667

A thesis submitted for the degree of Doctor of Philosophy

School of Mechanical and Manufacturing Engineering

Faculty of Engineering and Computing

Dublin City University

January 2013

Supervisor

Dr. ABDUL GHANI OLABI

PhD 2013

Declaration

I hereby certify that this material, which I now submit for assessment on the programme of study leading to the award of PhD is entirely my own work, that I have exercised reasonable care to ensure that the work is original, and does not to the best of my knowledge breach any law of copyright, and has not been taken from the work of others save and to the extent that such work has been cited and acknowledged within the text of my work.

.....

MUSTAFA SAJJIA

Student ID Number: 56116667

Date: January 2013

Dedication

TO MY BELOVED

MAMA

(MONEERA ZAHWEH)

&

BABA

(HUSNI SAJJIA)

Acknowledgement

First and foremost, I am grateful to Almighty Allah from the core of my heart for the fulfillment of my wish for the completion of this dissertation. I offer my sincerest gratitude to my supervisor Dr. Abdul Ghani Olabi who has supported me with his patience and diligence, his assistance and expert guidance throughout my research. I would like to express my special appreciation towards Dr. Tim Prescott and Dr. Mohamed Oubaha for their assistance. They enriched my dissertation with their tremendously erudite and inspiring scientific discussions. Numerous people deserve recognition for contribution, large and small, which made it possible for me to complete this dissertation. I would also like to thank Mr. Liam Domican, Mr. Chris Crouch and Mr. Michael May for their assistance in technical support.

I would like to thank my friends and colleagues Mr. Andrew Clarke, Mr. Habibullah Amin Chowdhury, Dr. Saiful Amri Mazlan, Dr. Nasser Ekreem, Dr. Aazir Khan, Dr. Aran Rafferty, Dr. Khaled Benyounis, Dr. Sumesh Sofin Pillai and Dr. Rafael Ramos for their implausible support regarding exchanging ideas and arguments, which facilitated in acquiring diverse knowledge in the field of magnetostrictive materials and relative topics.

In my daily work life, I have been truly blessed with a friendly and cheerful group of fellow colleagues. Consequently, I would also like to thank my friends and colleagues Mr. Ahmad Baroutaji, Mr. Hussam Achour, Mr. Muhammad Hasanuzzaman, Mr. Shahriar Hasan, Mr. Shadi Karazi, Mr. Sabawoon Shafaq and Mr. Ayad Mohamed for their suggestions, resources and encouragement. I apologise for the so many names not mentioned here; this only means that you are closer to my heart than you are to my mind.

I would like to thank the chaplaincy team in DCU specially Fr. Joe Jones for all their help and support. In addition, I would like to thank the school secretary Ms. Suzanne Dockery for all her help.

I would like to thank University of Aleppo - Syria for the financial support during my study time; without their support, this dissertation would not have been possible.

Finally, I would like to thank my siblings Mohammad, Ahmad, Mahmoud and Farah for their unconditional love and support throughout my study life. I am eternally grateful to them.

Table of Contents

Table of Contents

Table of Contents

Abbreviations

DEGDA	Di Ethylene Glycol Diacrylate
CA	Citric Acid
XRD	X-Ray Diffraction
EVA	A comprehensive and extremely versatile graphics program for easy, fast and convenient 2- and 3-dimensional XRD data evaluation and presentation
JCPDS-ICDD	Joint Committee on Powder Diffraction Standards - International Center for Diffraction Data
FWHM	Full width at half maximum
DTA/TGA	Differential Thermal Analysis and Thermo-Gravimetric Analysis
SEM	Scanning Electron Microscope
FE-SEM	Field Emission-Scanning Electron Microscope
FTIR	Fourier Transform Infrared Spectroscopy
VSM	Vibrating Sample Magnetometer
Ms	Saturation Magnetisation
Hc	Coercivity/Coercive field
Mr	Remnant Magnetisation
TB	Blocking Temperature
ZFC	Zero-Field Cooled
DoE	Design of Experiment
RSM	Response Surface Methodology
ANOVA	Analysis of Variance
PVA	Polyvinyl alcohol

List of Figures

List of Figures

List of Figures

List of Tables

Abstract

The phenomenon of magnetostriction takes place where there is a change in dimensions that spontaneously occurs in ferromagnetic and ferrimagnetic materials when an external magnetic field is applied. Cobalt ferrite, being a ferrimagnetic material, has been proposed as a suitable magnetostrictive material for some applications in the area of sensors and actuators. In such applications, speed of response with accurate displacements is important. Although cobalt ferrite has been shown to have a small magnetostrictive coefficient, which is a disadvantage, it also has a very small hysteresis characteristic. It follows that the results of using this material should be a smaller amount of energy loss and higher accuracy at high frequencies, and these benefits may outweigh this disadvantage.

In this thesis, making cobalt ferrite powder with nano-sized particles is suggested as a first step in a solution to overcoming the disadvantage mentioned above, if the particles are small enough to have only one magnetic domain. Powders were prepared employing the sol–gel technique. A particular emphasis is devoted to an understanding of the role of the chemical parameters involved in the sol–gel technique, and of the effect of the heat treatment on the structures and morphologies of the powders obtained. These were investigated by varying the initial parameters of the experiment in addition to the heat treatment temperature. The magnetic characteristics of the optimum nanoparticles were measured. The heat treatment process was simulated and optimised by means of DoE. The optimal heat treatment conditions, which facilitate the attainment of cobalt ferrite nanoparticles under low electrical operating costs, were defined.

Nanoparticles obtained employing the optimal solution were uniaxially pressed to form standard disc samples, and sintered under continuous ramp rate and single dwell time conditions. A study of the powder behaviour during this process, the density variation with pressing applied pressure, sintering temperature and dwell time, was conducted.

Chapter 1

Introduction

1 Introduction

1.1 Theoretical background

The magnetostrictive effect was first described in the 19th century (1842) by the English physicist, J.P. Joule. He observed that a sample of a ferromagnetic material, i.e. iron, changed its length in the presence of a magnetic field. Joule actually observed a material with negative magnetostriction (because, by convention, the effect refers to a decrease in length when the magnetic field is increased) but, since that time, materials with positive magnetostriction have also been discovered.

The causes of magnetostriction are similar for both types of materials. The change in length is the result of a change in the magnetic field orientation of some of the magnetic domains in the material, which happens because the domain becomes aligned with the externally applied magnetic field. This is achieved by unpaired electrons which move in orbitals around some of the atoms in these materials. These orbitals are non-circular, and their probability densities have defined geometric properties. Unpaired electrons in each of these orbital produces a magnetic field with specific magnitude and direction, and some orbitals enable the material to respond to the direction of the applied magnetic field better than other orbitals. Because the electrons in these orbitals are in incomplete shells, it is possible for them to switch instantaneously from one orbital to another, and so enable the material to respond to the externally applied magnetic field.

Because these electrons are the outermost electrons in each of the atoms concerned (the conduction electrons, if there are any, are not attached to the atoms at all) they also influence the distance between atoms; that is the distance with which one atom can approach a neighbouring atom. The responses are complex, because these orbitals (in the "d" shell in transitional elements, and in the "f" shell in the rare earth elements) also interact with other orbitals (in the "p" shell) which define the chemical properties of the element, including the basic structure and properties of the crystal lattices. The overall result is that where electrons in a magnetic domain switch from one orbital to another, there is a small change in the shape of the crystal lattice. Therefore the new orientation of the magnetic field in an individual magnetic domain causes a tendency for an extension or a contraction of the surrounding part of a sample of the material.

A magnetic domain buried deep within the rigid structure of a solid cannot easily change the lattice dimensions of its crystal structure. Local stresses will be produced in itself and in the neighbouring sections of the solid, where the crystal structure is not aligned in the same direction. There is therefore a need to supply energy to allow the changes described above to take place, and to allow that part of the material to experience the elastic energy involved in the creation of stresses and strains, which must occur as a result of the change in lattice dimensions. The change requiring the smallest amount of energy is a change in magnetic orientation of 180 degrees. Orbital switching requiring a change in magnetic orientation of 90 degrees will require the largest amount of energy.

Therefore, when a stronger magnetic field is applied to the sample, energy is transmitted to the material, and so more and more of the domains are enabled to change their magnetic orientation, to allow them to respond in the same direction as the applied magnetic field. When all of the magnetic domains have become aligned with the externally applied magnetic field, as much as the crystal lattice will allow, the saturation point has been achieved. Figure 1.1 shows the idealised behaviour of length change versus applied magnetic field, for a material with positive magnetostriction.

The property is such that a sample of greater original length will extend or contract to a greater extent than a sample with a smaller original length. Therefore it is

convenient to measure the magnetostriction as a change in length divided by the original length of the sample, and to express the property as a strain.

In the case of positive magnetostriction, where there is an extension of the sample of material in the direction of the magnetic field, there is also a contraction of the cross-section at the same time, in such a way that the volume is kept nearly constant. The size of the volume change is so small that it can be neglected under normal operating conditions.

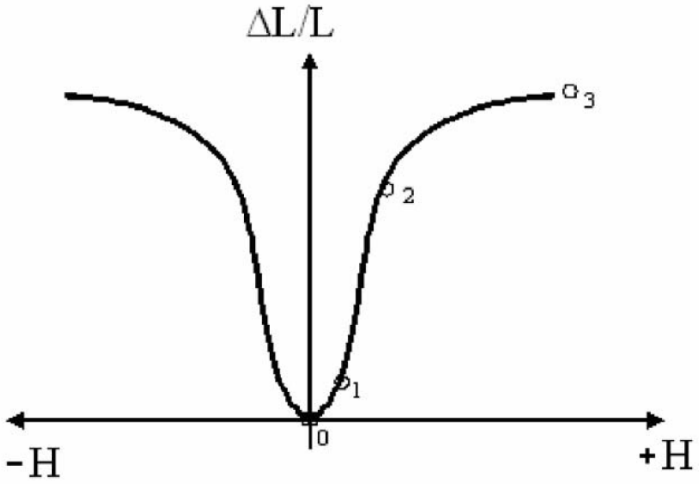

Figure 1.1 Strain versus magnetic field

When a magnetic field is established in the opposite direction, the field is assigned a negative value by convention, but the negative field produces the same elongation in the magnetostrictive material as would be produced by a positive field. The curve is therefore symmetrical about the "y" axis, or about the zero magnetic field condition. The shape of the curve is reminiscent of a butterfly and so the curves are referred as butterfly curves. Referring again to Figure 1.1, it can be seen that there are points on the curve labelled 0, 1, 2, and 3. In the region between 0 and 1, where the applied magnetic field is small, the magnetic domains show almost no common orientation pattern. Depending on how the material was formed there may be a small amount of a common orientation pattern, which would show itself as a permanent magnet bias. In the region 1-2 ideally there should be an almost linear relationship between strain and magnetic field. Because the relationship is a simple one, it is easier to predict the behaviour of the material and so most devices are designed to operate in

this region. Beyond point 2, the relationship becomes non-linear again as a result of the fact that most of the magnetic domains have become aligned with the magnetic field direction. At point 3 there is a saturation effect, which prevents further strain increase.

The behaviour of the magnetostrictive materials in various applications is complex, because the changing conditions during operation causes changes in material properties. The maximum useful magnetostrictive strain is one of the key parameters defining the resulting mechanical output in the case of a magnetostrictive actuator. Magnetostriction only occurs in a material at temperatures below the Curie temperature, but when the Curie temperature is below the temperature of the environment, the magnetostriction effect has little practical value.

1.2 Research background

In internal combustion engines, it is important the fuel systems to be efficient. They should meet the emissions targets. It is of a significant interest in engine-based research to increase the fuel efficiency and to decrease the environmental pollution. This all depends mainly on any possible improvements in the fuel injection system. It is a fact that multiple fuel injections per combustion cycle would increase the fuel efficiency and lower the NOx in addition to the particulate emissions. This must occur within a very short time. But, due to the present stroke speed limitations of magnetic solenoid valves, the current systems for reliably controlling multiple injections are limited. Moreover, multiple injections require the development of high-speed actuators.

Magnetostrictive materials have been considered to provide a potential solution for a better control of fuel injection. However, many manufacturing methods and improvements for the materials are yet to be explored. Besides, several innovations with respect to the fuel injector actuator are currently under exploration with Terfenol–D as a preferred actuator material [1].

A research project was previously conducted. The main objective was the development of a new kind of instrument for measuring electrical current which would operate with mechanical waves based on functional materials instead of magnetic flux variations [2].

Instrument transformers in devices for the measurement of voltage and electrical currents, are key elements within the modern systems of generation, transmission and distribution of electrical energy. Their principle of operation is based on magnetic flux variation. They are the basic input signals required for controlling the power flows in any electrical grid. Their importance has grown even greater in modern and complex power networks due to the tighter control required inside a sector undergoing profound changes due to world-wide electrical market deregulation.

Conventional transformers for measurement of large electrical currents in high voltage grids have secondary windings which produce proportionally reduced electrical currents (5 A, 1 A) suitable for measurement. For lines with voltage levels of more than 220 kV, that usually support currents higher than 2000 A, these inductive measurement transformers are large, heavy and expensive devices with certain risks of explosion. However, as the power of the electrical networks is steadily increasing worldwide, manufacturers of instrument transformers and electrical utilities companies are becoming ever more concerned with this problem [3].

The proposed system in the previous project consists essentially of a current sensor and the associated modules. The current sensor is formed by an emitter, and a receiver. The emitter is based on magnetostrictive materials that generate mechanical wave under the alternate magnetic field induced by the primary current to be measured. Thus the 50 Hz, or 60 Hz, electrical signals are converted into elastic (mechanical) waves that propagate through a coupling structure until they reach the receiver. The receiver is based on piezoelectric materials. These materials have the property of inverse conversion of energy. Thus, the mechanical waves are transformed into electrical signals in the receiver. These electrical signals from the receiver are then amplified and compensated through electronic circuits.

One part of the previous project was the development of the emitter material. In this study, the process of preparing, shaping and sintering the new material in order to meet the target characteristics of the emitter magnetostrictive compound was conducted. Maximum priority was assigned to the following coefficients: linear signal range (avoiding the zero crossing), thermal stability and high magnetostrictive coefficient to improve the performance of the sensor by increasing its signal-to-noise ratio.

As Terfenol–D is the most frequently used magnetostrictive material, it had been proposed due to its high magnetostrictive coefficient. However, at high frequencies, a small magnetostrictive coefficient was observed in addition to a time delay between the point when the magnetic field strength reaches its maximum value and the point when the displacement reaches its maximum value. For a rod with 8 mm diameter and 68 mm long, the displacement, under 11 MPa as pre-stress (550 N pre-load), decreased from 0.055 mm (815 ppm) to 0.04 mm (592 ppm) when the frequency of the excitation current is increased from 20 Hz up to 70 Hz. Figure 1.2 shows on the left side the displacement versus current curve and on the right side the time related data acquisition with force, displacement, current and voltage when the frequency of the excitation current increases from 20 Hz (top) to 70 Hz (bottom) [4].

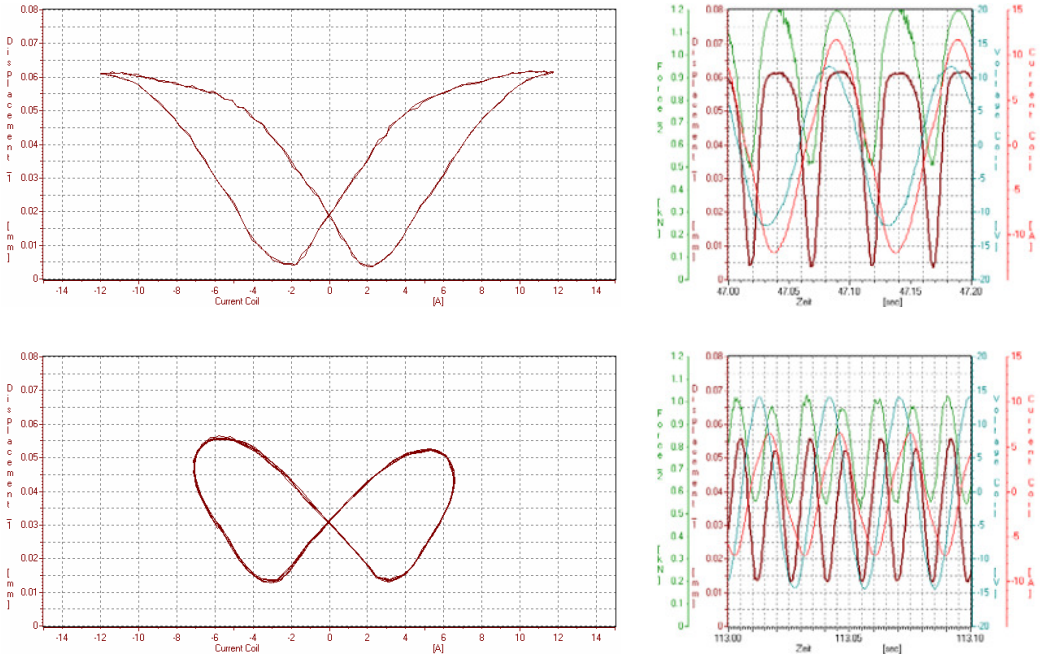

Figure 1.2 The displacement versus current curve and the time related data acquisition, left and right respectively, for 20 Hz (top) and 70 Hz (bottom) [4]

Terfenol–D suffers from the problem of eddy currents, which are electric currents induced in the material when it is exposed to an alternate magnetic field. The induced circular currents in the material produce magnetic fields opposite to the original magnetic field [5]. Therefore within the material, the local magnetic field strength will be decreased, and there is a delay in reaching the point where the maximum occurs.

This leads to a power loss and a limitation in the frequency at which the material can operate efficiently.

In many potential applications, especially in transformers, speed of response and the ability to operate at high frequencies are important. As a result, a necessity arose for the substitution of Terfenol–D with another material. Since some ferrites have high resistivities, eddy currents are not a problem when using these materials. In other words, high resistivity will reduce the eddy currents and therefore no opposing magnetic field is created.

Cobalt ferrite ($CoFe_2O_4$) falls into this category. It has been proposed as a solution to reduce eddy currents and their effects. In addition, it could be used to give a response (in the form of a mechanical elastic wave) as a magnetostrictive material and preserve the features of the original excitation current more faithfully. By using cobalt ferrite, it was anticipated that a good signal-to-noise ratio would be obtained in addition to the elimination of eddy current problem.

1.3 Motivation of study

Pure cobalt ferrite ($CoFe_2O_4$) has a very high electrical resistivity of 1×10^{7} Ωcm when compared to Terfenol–D, which has electrical resistivity of 58×10^{-6} Ωcm. However, cobalt ferrite has a smaller magnetostrictive coefficient than that of Terfenol–D. Therefore, cobalt ferrite has been employed as a solution to reduce eddy currents and their effects. As a comparison between a rod of Terfenol–D and another made from cobalt ferrite, both with 20 mm diameter and 100 mm long, under 3 MPa as pre-stress, the hysteresis loop of cobalt ferrite was found to be smaller in size than that of Terfenol–D which means that the loss of energy for each cycle is much smaller when cobalt ferrite is used as shown in Figure 1.3. Nevertheless, a relatively small magnetostrictive coefficient was observed as well as the presence of hysteresis as shown in Figure 1.4. It showed the displacement to reach 110 ppm at 140kA/m. It increased to 140 ppm when a pre-stress of 1 MPa was applied.

The cobalt ferrite rod was made from micro-sized powder. This powder with average particle size of 5.34 μm was prepared in a previous study employing a solid-state reaction method by blending both cobalt and iron oxides in a conventional ball mill then annealing the resultant mixture in a horizontal tube furnace at 1000 °C for 72 h [6].

This powder (with Ag/Ni additives) was cold iso-statically pressed into a rod using a wet-bag isostatic press (Stansted Fluid Power Ltd., UK) and sintered. This rod achieved a relative density of 91.49%. This value was higher than the value of 83.91% recorded for a rod made from the same powder but containing no additives. However, there is a necessity to improve the magnetostrictive coefficient of cobalt ferrite because it is very much smaller than the magnetostrictive coefficient of Terfenol–D.

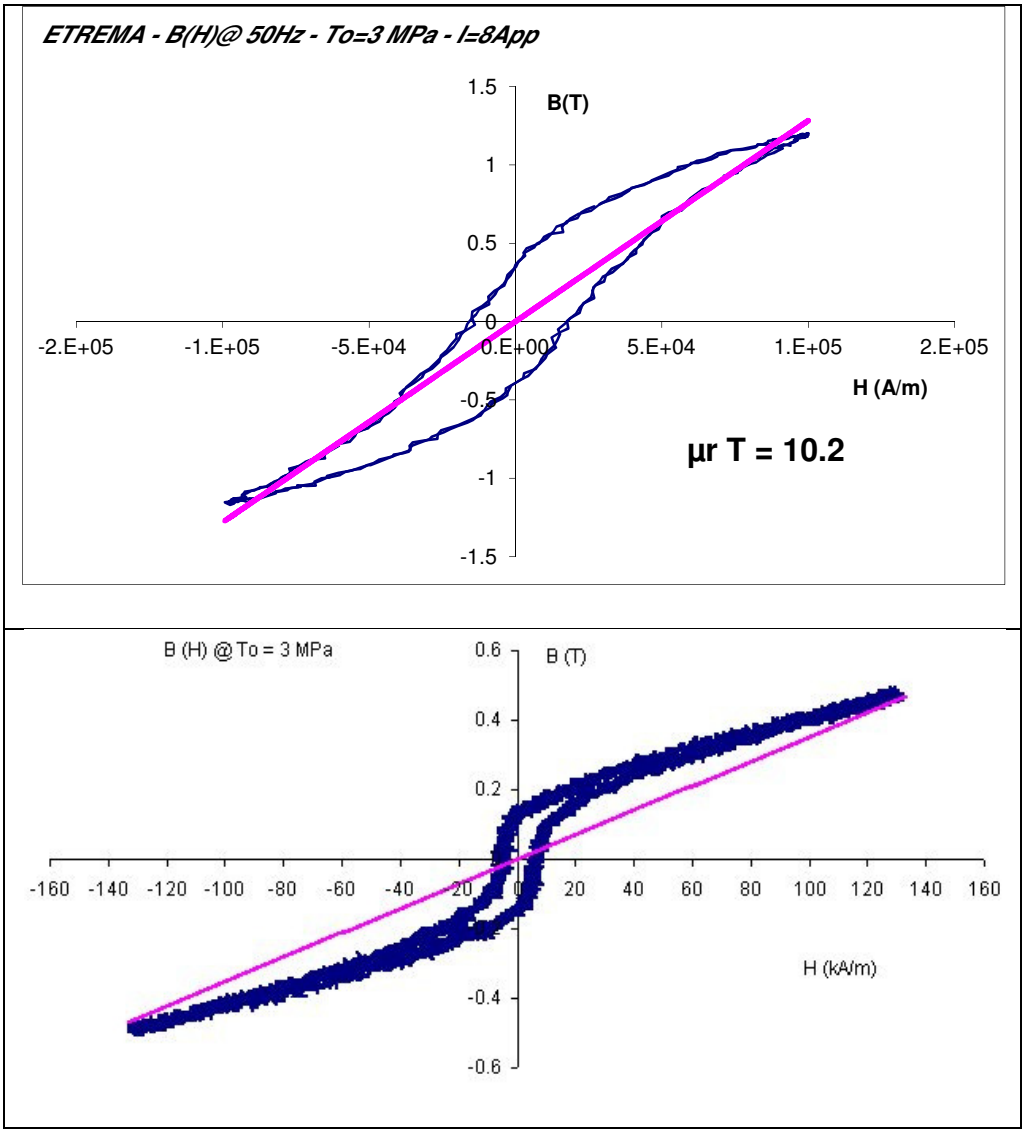

Figure 1.3 Hysteresis loops of Terfenol–D (top curve) and Cobalt ferrite (bottom curve) [7, 8]

Magnetic anisotropy is defined as the dependence of magnetic properties on a preferred direction. In other words, it is the energy necessary to deflect the magnetic moment in a single crystal from the easy to the hard direction whereas the magnetic moment in a single crystal is basically aligned towards the easy direction. However, the

easy and hard directions arise from the interaction of the spin magnetic moment with the crystal lattice (spin-orbit coupling). Magnetostriction is another effect connected to (spin-orbit coupling). As a result, the magnitude of the resultant strain is essentially dependent on two factors, the strength of the applied magnetic field and the angle between the direction of the easy axis of magnetisation and the applied magnetic field.

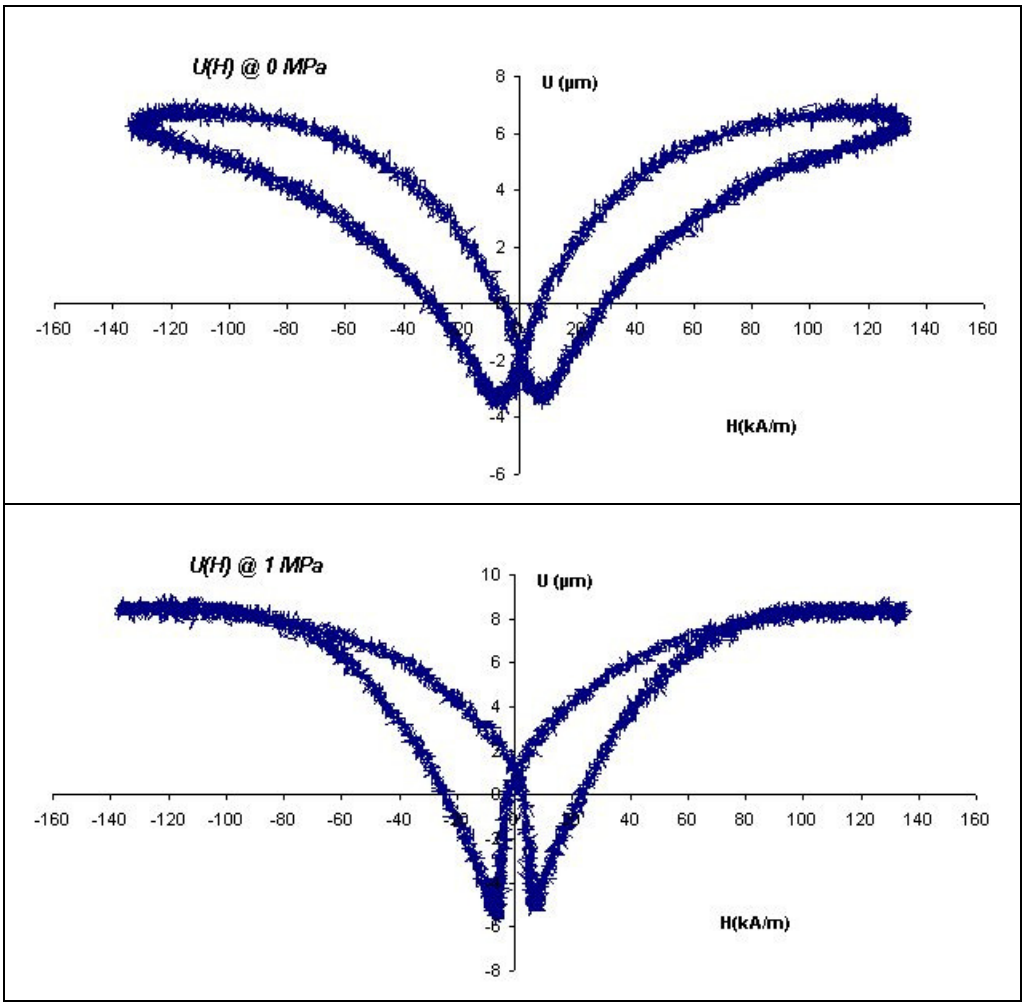

Figure 1.4 Magnetostriction versus magnetic field for cobalt ferrite [8]

Magnetostriction is mainly influenced by the magnetic and structural factors. The first factor is related to the origin of the particles the material is made from. A multi-domain particle contains a definite number of domains in which the easy axes of magnetisation are arbitrarily oriented and that is in order to lower the magnetostatic energy of the whole particle itself as shown in Figure 1.5. On the other hand, a single-domain particle has one major domain with one predominant easy axis of magnetisation as shown in Figure 1.6.

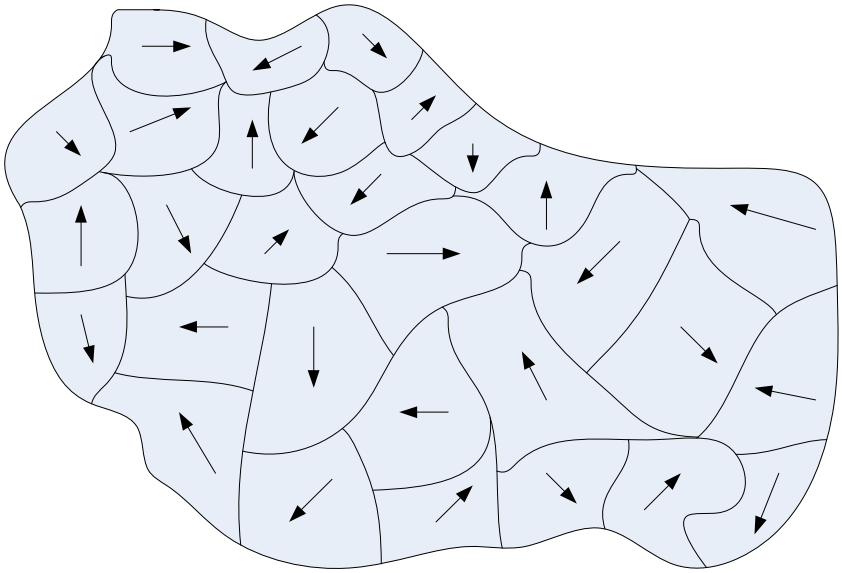

Figure 1.5 A multi-domain particle with the easy axes of magnetisation randomly oriented

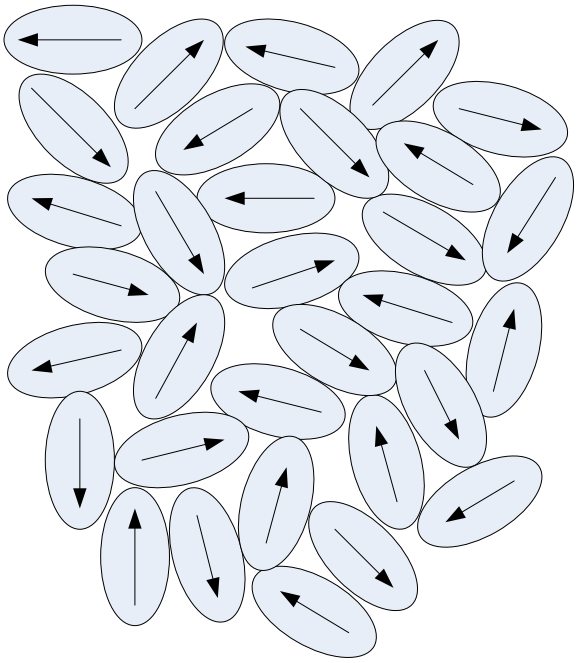

Figure 1.6 Single-domain particles with the easy axes of magnetisation randomly oriented

When the material is made from single-domain particles, there is a chance to control these particles during the preparation process and then to control the respective magnetic properties. The first step is to align the easy axes of magnetisation of these particles so that they are parallel to each other by introducing them into a magnetic field. The second step is to press these particles into a compact and sinter it at an elevated temperature. Introducing the sintered compact into an adequate magnetic field,

which must be perpendicular to the aligned easy axes of magnetisation, would deviate all grains' magnetic moments from the easy to the hard direction of magnetisation at 90° causing the magnetostriction to reach its maximum value as shown in Figure 1.7.

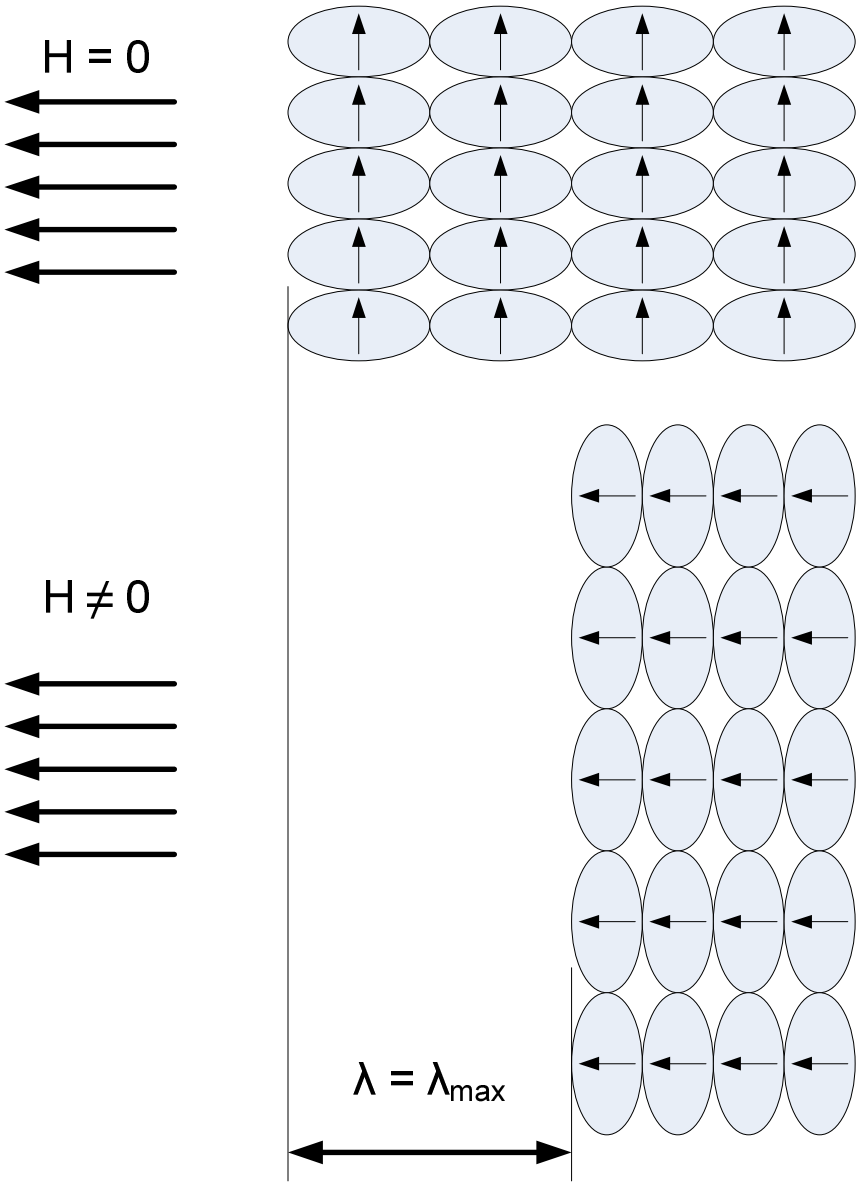

Figure 1.7 Pre-alignment of the easy axes of magnetisation maximises magnetostriction

The second factor is related to density. As mentioned above, cobalt ferrite rod, prepared (pressed and sintered) with average particle size of 5.34 µm, achieved a relative density of around 92%. This accounts for 8% porosity. The sintered compact must contain as little porosity as possible because this affects the final magnetic properties negatively and minimises the magnetostriction. Porosity (especially inside of

the grain) is an important microstructural feature limiting the movement of domain walls as shown in Figure 1.8. The intragranular porosity is more deleterious than the intergranular.

Cobalt ferrite powder with single-domain particles is proposed in this study as a solution to overcome the problem of easy axes of magnetisation being randomly directed and the problem of relatively high porosity. The study gives a potential solution for this application and for many other applications which use magnetostrictive materials such as those of industrial applications i.e. actuators, sensors.

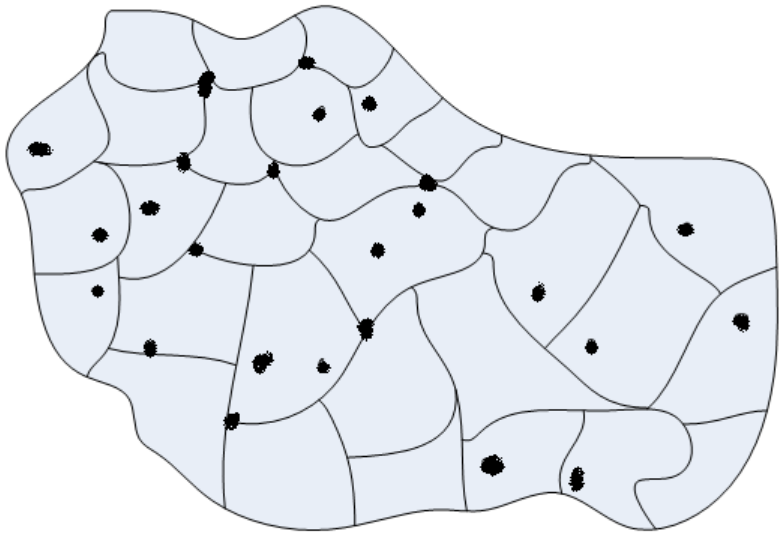

Figure 1.8 Intragranular and intergranular porosity

1.4 Research objective

The main objective of this study is the development of the magnetostrictive coefficient of cobalt ferrite material employing single-domain nanoparticles. This study will be concerned about improving the density of the material to higher values employing cobalt ferrite nanoparticles. The project will deal basically with preparing the nanoparticles employing one of the chemical routes. Structural and magnetic characterisation will be executed. A modelling and then an optimisation of the heat treatment operation (part of the preparation method) will be performed in order to obtain the material with lowest electrical operating cost. Finally, the sintering behaviour

of the nanoparticles obtained in this way will be investigated in order to achieve the highest density possible.

To sum up, the scope of this study can be summarised as follows:

A. To prepare cobalt ferrite nanoparticles $CoFe_2O_4$ in which particles should be single-domain employing the sol–gel technique

B. To characterise the prepared nanoparticles regarding the structure, morphology and magnetic properties

C. To model and optimise the heat treatment operation of cobalt ferrite nanoparticles employing Design of Experiment (DoE)

D. To study the sintering behaviour of nanoparticles employing linear ramp rate and single dwell time conditions at high temperatures

1.5 Structure of thesis

This thesis is organised in eight chapters. This chapter discusses the background of the research topic and aims of the study. Each chapter in this thesis ends with a brief summary outlining the achievements and findings that were established. The remainder of this thesis is organised as follows:

Chapter 2: The theoretical background and literature review of related research topics are elaborated in this chapter

Chapter 3: This chapter covers experimental methodology in a nutshell and includes a brief summary about characterisation equipment

Chapter 4: This chapter presents some results and includes discussions of the initial nano powder preparation process in addition to highlighting the most important findings regarding the effect of the crosslinker and the chelating agent

Chapter 5: This chapter presents further results and includes discussions of the structural and magnetic characterisations again with the most important findings, highlighted

Chapter 6: This chapter presents further experimental results and also includes discussion of the modelling and optimisation processes of the heat treatment operation. The significant findings are emphasised

Chapter 7: This chapter presents results and includes discussion of the sintering process in which nanoparticles are combined to form discs. Again the significant findings are emphasised

Chapter 8: This chapter states conclusions and explains future work

Chapter 2

Literature review

2 Literature review

2.1 Introduction

The magnetic oxide of iron is a compound in which the two fundamental oxides Fe_2O_3 and FeO have been incorporated into a crystal structure with the exact ratio of 1:1. The ceramic powders generally known as ferrites are essentially related to this so-called mixed oxides of iron with a substitution of some of the iron using one or more metallic elements, such as manganese, nickel, zinc, magnesium, cobalt, copper, rare earths, barium, strontium, and lead. The magnetic properties of these materials are determined not only by their chemical composition but also by their microstructure, i.e. grain- and pore-size distribution, total porosity (or relative density, percentage of theoretical density), and grain-boundary characteristics [9-13]. Knowledge of sintering, which determines end-product microstructure, is therefore essential for the control and optimisation of the magnetic properties sought in the finished product.

Ferrites can be made by conventional ceramic processes in which the main technological issues are (i) obtaining bodies with high relative density (very low porosity), (ii) increasing the grain size while at the same time seeking to achieve a narrow grain-size distribution, and so avoiding abnormal grain growth [6, 14].

2.2 Cobalt ferrite

2.2.1 The crystalline structure

Cobalt ferrite is a spinel and is usually assumed to have a collinear ferrimagnetic spin structure. This spinel was shown to be partially inverse with the formula (Co_xFe_{1-x}) $[Co_{1-x}Fe_{1+x}]$ O_4, where the round and square brackets indicate the tetrahedral A and octahedral B sites, respectively. The ratio, Fe(A)/Fe(B), has been found to vary from 0.65 to 0.92 for two extremes, quenched and slowly cooled samples, respectively. From these ratios, the distributions of the cations in tetrahedral and octahedral sites were determined to be as follows: $(Co_{0.04}Fe_{0.96})$ $[Co_{0.96}Fe_{1.04}]$ O_4 for the slowly cooled and $(Co_{0.21}Fe_{0.79})$ $[Co_{0.79}Fe_{1.21}]$ O_4 for the quenched cobalt ferrite [15].

The spinel structure is composed of a close-packed oxygen arrangement in which 32 oxygen ions form a unit cell that is the smallest repeating unit in the crystal network. Between the layers of oxygen ions, if we simply visualise them as spheres, there are interstices that may accommodate the metal ions. Moreover, the interstices are not all the same. Some are coordinated by 4 nearest neighbouring oxygen ions whose lines connecting their centres form a tetrahedron. These are the A sites. They are called tetrahedral sites. The other type of site is coordinated by 6 nearest neighbor oxygen ions whose centre connecting lines describe an octahedron. These are the B sites. They are called octahedral sites. In the unit cell of 32 oxygen ions, there are 64 tetrahedral sites and 32 octahedral sites. Generally, if all of these were filled with metal ions, of either 2+ or 3+ valence, the positive charge would be very much greater than the negative charge and so the structure would not be electrically neutral. It turns out that of the 64 tetrahedral sites, only 8 are occupied and out of 32 octahedral sites, only 16 are occupied. In cobalt ferrite, eight units of $CoFe_2O_4$ go into a unit cell of the spinel structure as shown in Figure 2.1. In addition to the 32 oxygen ions, there are 16 ferric ions and 8 cobalt ions. Theoretically, the ferric ions preferentially fill the tetrahedral sites, and as there is room for only half of them (eight), the remaining eight go on the octahedral sites as do the eight Co^{++} ions. The antiferromagnetic interaction orients these eight Fe^{+++} moments and eight cobalt moments antiparallel to the eight Fe^{+++} moments on the tetrahedral sites. The Fe^{+++} ion moments will just cancel, but the

moments on the cobalt ions give rise to an uncompensated moment or magnetisation [5].

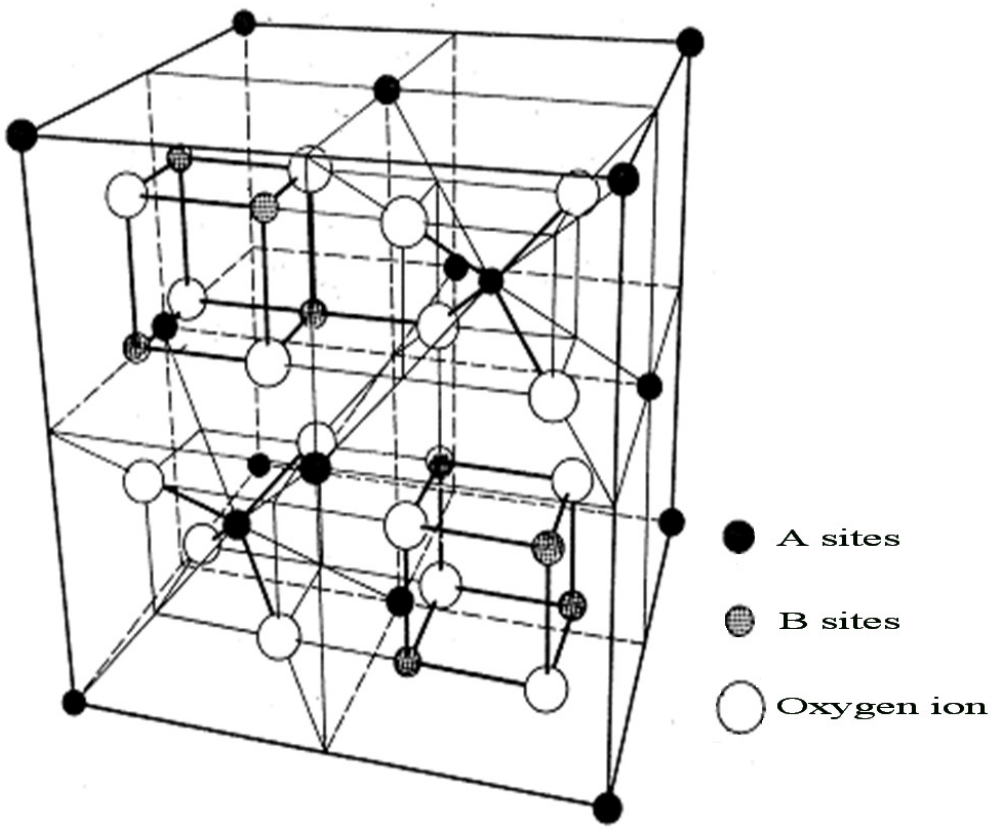

Figure 2.1 Spinel structure

2.2.2 The magnetostrictive material

2.2.2.1 Pure cobalt ferrite

Cobalt ferrite is a magnetostrictive material. It goes through a physical dimensional change when exposed to a magnetic field. This occurs because magnetic domains in the material align with the magnetic field. The mechanism of magnetostriction at an atomic level is a comparatively complicated subject matter but on a macroscopic level may be divided into two distinct processes. The first process is dominated by the migration of domain walls within the material in response to external magnetic fields. Second is the rotation of the domains. These two mechanisms allow the material to change the domain orientation which in turn causes a dimensional change as

shown in Figure 2.2. This dimensional change is isochoric, so there is an opposite dimensional change in the orthogonal direction.

Bozorth et al. [16] measured the magnetic anisotropy and magnetostriction in various single crystals of ferrites. The effect of heat treatment with and without the presence of a strong magnetic field on the crystal anisotropy and magnetostriction was investigated. Measurements were found to be related to the initial stoichiometry and dependent on the crystal direction along which they were taken. In addition, magnetic annealing was found to have a large effect on crystal anisotropy and magnetostriction of cobalt ferrite. The magnetic anisotropy of a cobalt ferrite single crystal at room temperature was found to be as high as 4×10^{6} ergs/cm^{3}. Magnetostriction is as high as 800×10^{-6}. Magnetic annealing is effective at temperatures as low as 150 °C. It causes the hysteresis loop to become square. According to Chen et al. [17], cobalt ferrite offers good mechanical properties and shows a precipitous slope of magnetostriction at low applied fields. This contributes to a high sensitivity of magnetic induction to stress, hence giving high signal-to-background noise ratios which make it suitable for sensor and actuator applications. Cobalt ferrite has been reported to show linear magnetostrictive strains up to -225×10^{-6} with a maximum strain derivative $(d\lambda/dH)_{\sigma}$ of 1.3×10^{-9} A^{-1}m under zero applied stress. This strain derivative is an order of magnitude greater than that of Terfenol-based composites 0.2×10^{-9} A^{-1}m.

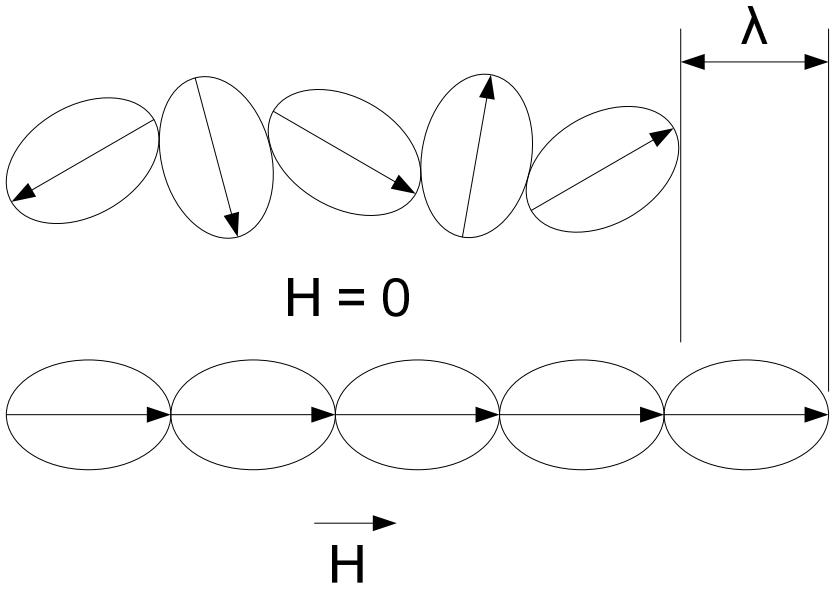

Figure 2.2 Magnetostriction mechanism

To further improve the magnetostrictive properties, it is essential to improve linearity of response by decreasing the magnetostrictive hysteresis and to increase the sensitivity of magnetisation to stress. Magnetic annealing was found to give rise to high levels of magnetostriction and $(d\lambda/dH)_{max}$ under hard axis applied fields. A sintered sample of cobalt ferrite was annealed at 300 °C in air for 36 h under a dc field of 318 kA/m (4kOe) [18]. A significant improvement in magnetostrictive properties was observed after magnetic annealing. The maximum magnetostriction increased in magnitude from -200×10^{-6} for the as-fabricated sample to -252×10^{-6}. The coercivity fields were measured to be 2.6 and 6.9 kA/m along the easy and hard axes respectively, compared to 5.4kA/m for the as-fabricated sample. The maximum strain derivative $(d\lambda/dH)_{max}$ in the applied field of around 50 kA/m increased from 1.5×10^{-9} $A^{-1}m$ to 3.9×10^{-9} $A^{-1}m$. Substituting a small amount of Mn for Fe (e.g., $CoFe_{1.8}Mn_{0.2}O_4$) increases $(d\lambda/dH)_{max}$ by 84%, substantially less than that achieved by magnetic annealing (an increase of 163%). These improved properties may degrade over time or after operation at elevated temperatures. The increase in maximum magnetostriction after magnetic annealing is attributed to the induced uniaxial anisotropy which affects domain configuration and in turn alters the measured magnetostrictive strain.

The <100> crystallographic directions are known to be equally easy axes of magnetisation. The effect of magnetic annealing is to induce a uniaxial anisotropy superimposed onto the magnetocrystalline anisotropy, making those <100> directions close to the induced easy axis more energetically favorable. As a result the domains in each grain of the annealed sample tend to align along the <100> directions of the grain that are close to the induced easy axis. When a magnetic field is applied along the hard axis of the annealed sample, domain magnetisation re-orients toward the field direction from local easy directions close to the induced easy axis. This results in a positive magnetostrictive strain along the easy axis but a negative strain along the hard axis.

2.2.2.2 Substituted cobalt ferrite

Substituting manganese Mn for Fe in cobalt ferrite reduced the Curie temperature linearly, by as much as 300 °C in the case of $CoFe_{1.2}Mn_{0.8}O_4$. It made a modest decline in saturation magnetisation (up to 20%). Maximum magnetostriction was attained with low Mn content, e.g. $CoFe_{1.8}Mn_{0.2}O_4$ while it decreased with further increase in Mn content [19]. Similar results were reported elsewhere [20, 21].

Magnetic anisotropy of Mn-substituted cobalt ferrites was found to increase substantially (to values that are of the order of magnitude 10^7 erg/cm^3) with decreasing temperature from 400 to 150 °K, and to decrease with increasing Mn content. Below 150 °K, it appeared that even under a maximum applied field of 5 T, the anisotropy of $CoFe_2O_4$ and $CoFe_{1.8}Mn_{0.2}O_4$ is so high as to prevent complete approach to saturation. Curie temperature was found to decrease linearly from 784 °K for pure cobalt ferrite to 577 °K for $CoFe_{1.4}Mn_{0.6}O_4$. The magnitude of the anisotropy of pure $CoFe_2O_4$ was found to be 2.65×10^6 erg/cm^3 at 300 °K [22].

The stress sensitivity of Mn and Cr substituted cobalt ferrite ($CoMn_xFe_{2-x}O_4$ and $CoCr_yFe_{2-y}O_4$) first increased as a result of Mn or Cr substitution, peaks at x = 0.2 and y = 0.4, and decreased below that of pure cobalt ferrite with higher Mn or Cr content. The strain derivative exhibited similar behaviour as shown in Figure 2.3. These magnetostrictive properties were measured using the strain gage method under quasi-static applied fields up to 2 T. Mn and Cr substitutions were found to reduce both magnetostriction and anisotropy of cobalt ferrite. Moreover, within certain ranges of substitute contents anisotropy was reduced more than magnetostriction and therefore the stress sensitivity was increased as it is proportional to the ratio (λ_{max}/K) of maximum magnetostriction to cubic anisotropy constant [23].

The maximum magnitude of magnetostriction of Ga-substituted cobalt ferrites ($CoGa_xFe_{2-x}O_4$) decreased monotonically with increasing gallium content over the range x = 0.0–0.8. The rate of change of magnetostriction with applied magnetic field ($d\lambda/dH$) showed a maximum value of 3.2×10^{-9} A^{-1}m for x = 0.2 which is much higher than those of Mn- and Cr-substituted cobalt ferrites even at a much lower applied field of H = 15 kA/m. This enhanced $(d\lambda/dH)_{max}$ implied high stress sensitivity. Curie temperature and anisotropy energy were reduced by the substitution of Ga for Fe at a greater rate than with Mn or Cr substitutions. The magnitude of ($d\lambda/dH$) was expected to depend inversely on anisotropy energy [24].

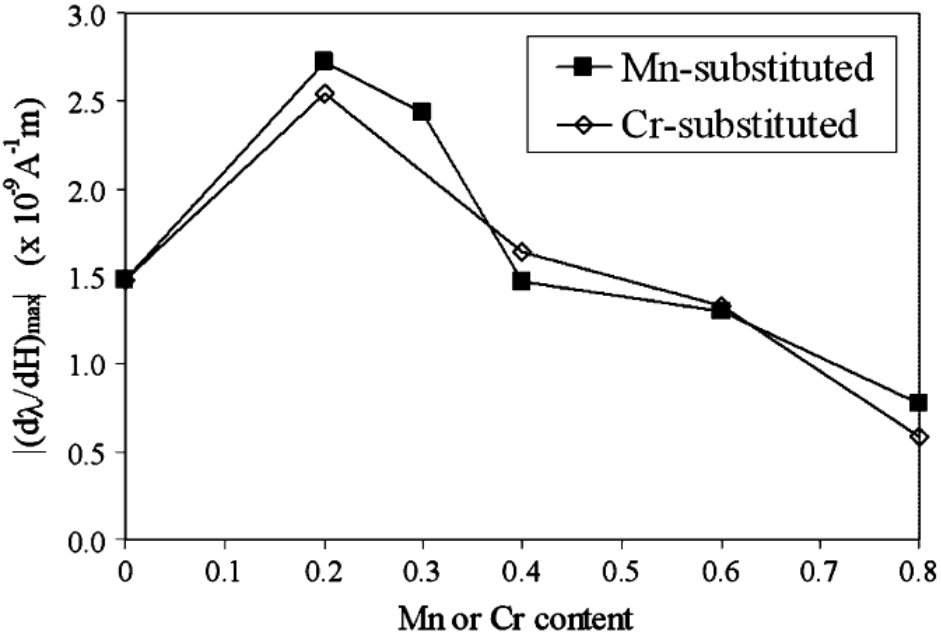

Figure 2.3 The magnitude of maximum strain derivative $|(d\lambda/dH)_{max}|$ versus the Mn or Cr content [23]

2.3 Cobalt ferrite nanoparticles

2.3.1 Introduction

Cobalt ferrite nanoparticles have recently become the subject of research interest from the point of view of the synthesis, the structure, the magnetic characterisation and the application [25-29]. In particular, the interest in cobalt ferrite has arisen due to its unique properties e.g. very high resistivity, a positive anisotropy constant and a high magnetostriction [16, 30]. In addition, cobalt ferrite possesses excellent chemical stability as well as good mechanical properties. These properties could make cobalt ferrite a potential candidate for many applications, such as high frequency magnets, information storage systems, magnetic bulk cores, microwave absorbers, magneto-optical recording media, actuators and sensors [31-34] and in biomedical applications, such as magnetic thermo-drug delivery and hyperthermia (abnormally high body temperature), magnetic resonance imaging and biosensors [35-41].

Kashevsky et al. [29] synthesised cobalt ferrite nanoparticles using a chemical precipitation process. These particles have been studied for magnetic hyperthermia. The

suspension based on cobalt ferrite nanoparticles was found not to have a toxic effect when introduced into a tumor. Kim et al. [35] prepared cobalt ferrite nanoparticles which were dispersed in water, and investigated as heating agents for magnetic thermo-drug delivery and hyperthermia. The heat generation was found to be dependent on the properties of these nanoparticles, including their composition, size and crystal structure in addition to the intensity of the AC magnetic field and applied frequency. Baldi et al. [42] concluded that cobalt ferrite nanoparticles synthesised employing the successive polyol method offer the possibility to optimise the heat release capability of magnetic fluid hyperthermia (MFH) mediators at a given frequency over a wide range, just by finely tuning the particle size.

Cobalt ferrite nanoparticles were used in a core shell system in which a magnetic core of cobalt ferrite and a shell of silica are prepared via a modified Stober synthesis [43]. The magnetic core was prepared by Massart's method employing cobalt and ferric chlorides. The monodisperse distribution could be obtained by means of fractionated precipitation. The average size of particles was found to be 14.5 nm. $CoFe_2O_4$ nanoparticles covered by a uniform silica shell have been prepared by Bonini et al. [44]. The nanoparticles were prepared by the co-precipitation of Co^{2+} and Fe^{3+} aqueous salt solutions by addition to a strong base solution. The sizes of the particles were in the range of 3-15 nm and their shapes were almost spherical.

However, methods for making cobalt ferrite nanoparticles are very diverse including the microwave hydrothermal flash method [45], the mechanochemical method [46], the combustion reaction method [47], the polymeric precursor method [48], the complexometric method [49], microemulsions [50, 51], the sol–gel technique [52], the new non-aqueous route [53], the forced hydrolysis method [54], a combustion wave method [55], the polymerised complex method [56] and chemical co-precipitation techniques [57, 58]. Nanoparticles prepared by these processes have different saturation magnetisation and coercivity values which mainly depend on particle size. Generally, the size of these nanoparticles was found to be dependent on the heat treatment temperature. The increase in the size at higher annealing temperatures might be a result of the formation of crystallite clusters. Moreover, particles come into contact with each other and under favourable energetic conditions they grow [59].

$CoFe_2O_4$ nanoparticles were synthesised via the pyrolysis of polyacrylate salt precursors prepared by in situ polymerisation of metal salts and acrylic acid [60]. The heat treatment at 500 °C for 3 h was considered to be moderate. The size of particles ranged from 20 to 30 nm which is a narrow size distribution. The size of particles was observed to increase up to 120 nm with increasing the heat treatment temperature up to 900 °C.

2.3.2 Microemulsions

Mathew and Juang [31] described in their paper the structure of various spinel ferrites, normal and inverse. They gave a short review on the various synthesis methods of spinel ferrites in microemulsion. They found that precipitation in a water-in-oil microemulsion is a very promising technique for preparing monodisperse, ultrafine particles of controlled size and morphology. The microemulsion methods have the advantages of being economical and environmentally friendly. They involve inexpensive and less toxic iron salts in addition to the reduced amount of organic solvent. Li et al. [61] prepared cobalt ferrite nanoparticles in a size range of 10-15 nm with different Co^{2+}/Fe^{3+} ratios using water-in-oil microemulsions (reverse micelles). It was found that both coercivity and blocking temperature increase with the increase of cobalt content in the ferrite structure. Similar results were observed elsewhere [62] where Co-substituted ferrite nanoparticles have been prepared by the co-precipitation method. The Curie temperature Tc and saturation magnetisation Ms were found to be lower than those found in larger samples, the “bulk” properties, and to decrease with the increase of cobalt content.

Cobalt ferrite nanoparticles of average size 4 nm have been synthesised by the reverse micelle approach as shown in Figure 2.4 [63]. The preparation of nanoparticles in nano-reactors formed employing the reverse micelle technique is an attractive technique. It overcomes the difficulties associated with agglomeration and polydispersity. Three successive transformations were detected which correspond to the loss of solvent and surfactant, the onset of the amorphous to crystalline conversion and the iso-chemical transformation which is the migration of cations between octahedral and tetrahedral sites in the inverse spinel structure. These transformations were found to be irreversible.

A microemulsion is an isotropic and thermodynamically stable phase formed by at least three components; two of them are non miscible, and a third, called surfactant, has an amphiphilic behavior. When inverse micelles are used, water nano-droplets are formed in an organic compound and used as nano-reactors in order to control particle size. These nano-droplets are surrounded by a surfactant coat that limits their size and separates them from the organic compound [64].

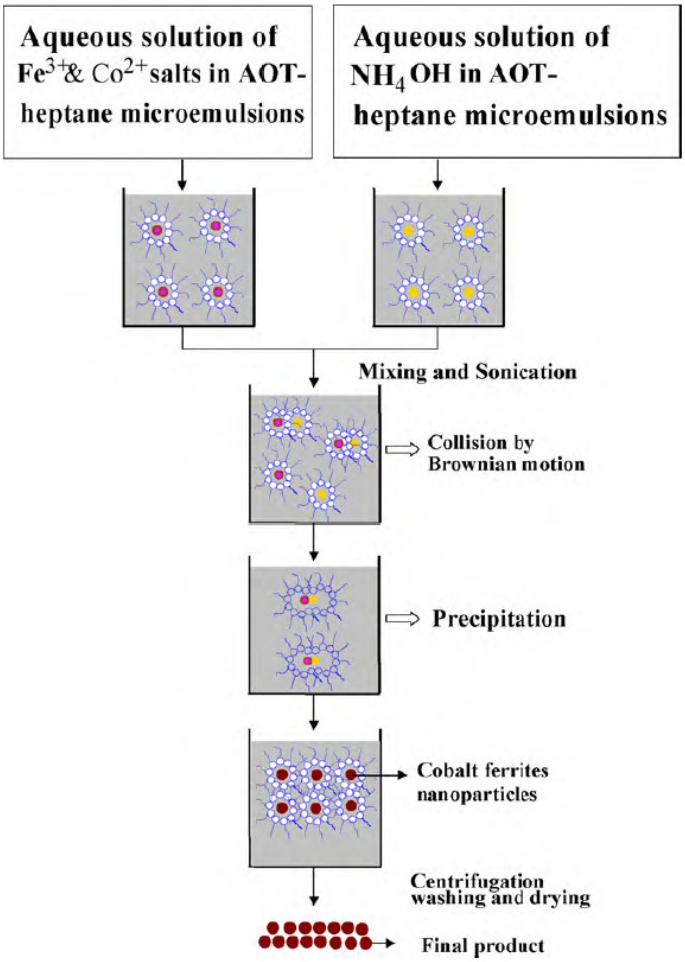

Figure 2.4 A schematic representation of the synthesis of cobalt ferrite nanoparticles using the reverse micelle method [63]

2.3.3 The control of particle size

$CoFe_2O_4$ nanoparticles were prepared by the co-precipitation method at 60 °C employing different Fe^{2+}/Fe^{3+} ratios in the initial solution. Using the Debye–Scherrer equation for theoretical predictions of size, as the Fe^{3+} in the starting solution increased, the average size of particles decreased sharply from 130 nm in a sample prepared with

only Fe^{2+} to 25 nm in a sample prepared with pure Fe^{3+}. The calculated values approximated the actual particle size as was illustrated in the SEM images. As the Fe^{3+} in the starting solution increased, the values of the saturation magnetisation Ms decreased sharply from 65.7emu/g in the sample prepared with Fe^{2+} to 19emu/g in the sample prepared with Fe^{3+}. The values of magnetic coercivity Hc decreased from 986.7 to 126.9Oe. It sharply increased to 594.1Oe in the sample prepared with Fe^{3+} [65].

Cobalt ferrite particles with a size range from a few micrometers to about 15 nm were synthesised using a modified oxidation process [27]. Particles with a size of about 36 nm showed a saturation magnetisation Ms of 64emu/g and a maximum coercivity Hc of 2020Oe at room temperature. The control of particle size was achieved by introducing various concentrations of ferric ions at the beginning of the reaction. Similarly, cobalt ferrite nanoparticles with a size range of 6.3-10.5 nm were prepared using a micelle chemical control method [66]. The particle size was thought to increase with the increase of cobalt content in the structure. XRD line broadening of the powders was observed to decrease with increasing particle size. $CoFe_2O_4$ nanoparticles with diameter of about 5 nm were prepared at 390 °C by the batch supercritical hydrothermal synthesis method [67]. The reaction time was found to have little influence on the size and morphology of nanoparticles.

The control of particle size of cobalt ferrite prepared using colloidal solutions was introduced for the first time by Moumen et al. [68]. The size of cobalt ferrite particles was found to decrease when the reactant concentration is decreased and when the concentration of the surfactant is increased. Cobalt ferrite nanoparticles have been prepared by the chemie douce approach [69]. An aqueous solution containing cobalt(II) chloride and iron(II) sulfate was heated to 90 °C and then transferred to a flask containing an aqueous solution of sodium hydroxide and potassium nitrate. The mixture was stirred at 90 °C under an air atmosphere for different periods of time (digestion time) after which a clear solution was decanted from the reaction vessel. The nanoparticles were then transferred into a large plastic beaker, washed with distilled water, dried overnight at 80 °C in air and milled using a mortar. The potassium nitrate was used as a mild oxidation agent in order to oxidise ferrous ions to ferric ions. The lattice parameter was found to increase with increasing the content of cobalt in the structure. With increasing the content of cobalt in the structure, the morphology of

nanoparticles changed from irregular to mostly spherical. The size of particles was found to increase with increasing the digestion time. Sorescu et al. [70] employed the hydrothermal method to prepare cobalt ferrite and reported a linear increase in the lattice parameter with increasing the content of cobalt in the ferrite structure.

2.3.4 The co-precipitation method

Cobalt ferrite nanoparticles have been prepared via the co-precipitation method. Cobalt and iron nitrates were dissolved in distilled water. An aqueous solution of NaOH was used as the precipitating agent. Both solutions were added dropwise from two separate burettes into a reaction vessel containing distilled water under mechanical stirring. The rate of addition was controlled in order to maintain a constant pH (8 or 10) during the process. Co-precipitation was controlled using thermostatic equipment at the desired temperature (60 or 70 °C). The precipitate was later subjected to heat treatment at 400, 500 or 600 °C for 4 h to achieve transformation into the spinel phase. The prepared particles were found to be mesoporous materials that have a particle size range of 8-45 nm with specific surface areas ranging from 99.3 to 21.4m^2/g. The particle size increased with the pH of the precipitating agent and the precipitation temperature [71]. Similar results were observed by El-Okr et al. [72].

$CoFe_2O_4$ nanoparticles were also prepared by the co-precipitation method using a microwave heating system in which the solution was heated to 160 °C and held at this temperature for 60 min [73]. The crystalline structure was obtained even though the maximum temperature during preparation was 160 °C. TEM measurements indicated that the synthesised ferrite material is composed of regular nano-sized particles. According to the Scherrer equation, the average particle size was estimated to be around 5 nm. The magnetic behaviour was characterised as superparamagnetic. Magnetisation measurements under magnetic field of 50kOe (ZFC and FC) were performed. The blocking temperature was found to be around 195 °K. The AC magnetisation was measured at applied field amplitude of 15Oe and at several frequencies between 10 and 3000 Hz. The cusp, which corresponds to the transition from the blocked state to the superparamagnetic state, was found to shift to higher temperatures as the frequency of the applied AC magnetic field is increased.

$CoFe_2O_4$ nanoparticles have also been prepared by a modified chemical co-precipitation method. Precursors were dissolved in de-ionised water with gentle heating

and then slowly poured into a well-stirred NaOH solution and left stirring for several minutes. A digestion process was performed on the mixture at 110 °C for 120 min. The gelatinous precipitate was afterwards filtered, washed several times using de-ionised water until the pH value of the solution became neutral and eventually dried at 80 °C. The as-prepared $CoFe_2O_4$ sample was heated from room temperature to 800 K and then cooled to room temperature, while magnetic data were collected in a magnetic field of 100Oe. With increasing temperature, a large drop in magnetisation occurred. This was thought to be a sharp transition to the paramagnetic state. The Curie temperature T_C was found to be 677 °K when heating up and 668.6 °K when cooling down as shown in Figure 2.5. This phenomenon was attributed to the change in the distribution of metal ions between the tetrahedral and the octahedral sites of the spinel structure. The increase in the degree of inversion is believed to cause the average exchange interaction to decrease, which in turn resulted in a decrease in T_C. Particles were found to be spherical and in the size range 20-30 nm. The value of saturation magnetisation Ms was estimated by measurement to be 61.77emu/g at room temperature [74].

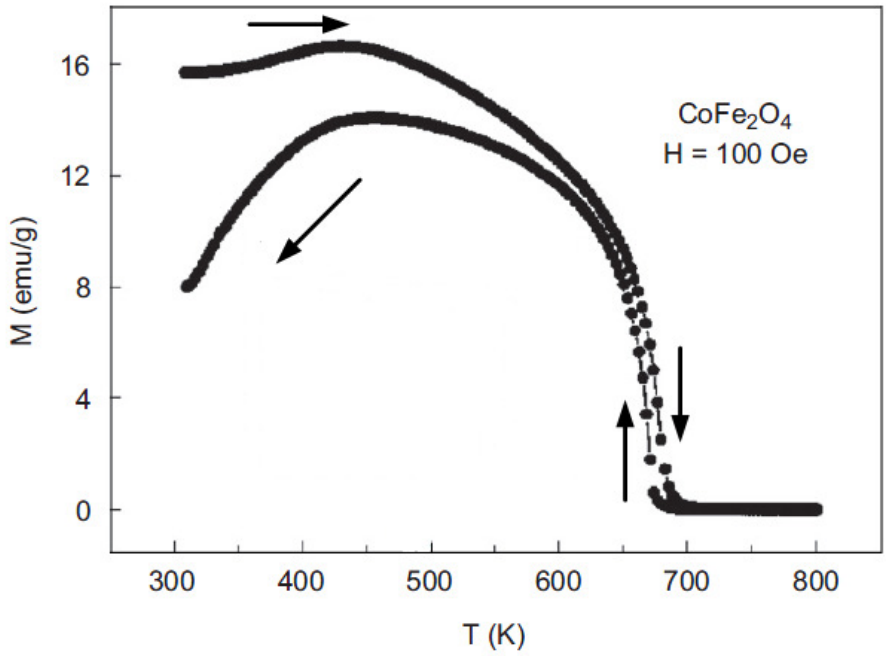

Figure 2.5 Magnetisation versus temperature curve for the $CoFe_2O_4$ particles [74]

Cobalt ferrite nanoparticles have been synthesised by both a conventional and a modified co-precipitation method. The conventional coprecipitation method was modified by controlling the addition flow rate of metal ions solution to the alkaline

solution under boiling conditions in order to enhance the magnetic properties of the particles by promoting their growth. The effects of the reaction time, flow rate and NaOH concentration in the process were investigated. Particles in the specific size range of 10-50 nm were observed in TEM images. The average size for particles with the highest coercivity of 4.6kOe was estimated to be 20 nm [75].

Cobalt ferrite nanoparticles have also been synthesised by a process involving both spraying and co-precipitation. Particles were found to have a smaller size and to be more uniform than those prepared by the regular co-precipitation. The surface area of particles was measured by BET. The results show that the specific surface area of $CoFe_2O_4$ nanoparticles prepared by spraying co-precipitation, 49.8m^2/g, is much larger than the specific surface area of nanoparticles prepared by traditional co-precipitation, 17.97m^2/g. According to the Scherrer equation, the size of $CoFe_2O_4$ nanoparticles prepared by spraying co-precipitation was calculated to be 10 nm, while that of traditional co-precipitation was calculated to be 30 nm [76].

2.3.5 The magnetic properties

2.3.5.1 Pure nanoparticles

Ai and Jiang synthesised nanocrystalline cobalt ferrite nanoparticles by a one-step sol–gel auto-combustion method [28]. It has been shown that the coercivity initially increased and then decreased with increasing annealing temperature whereas the particle size and saturation magnetisation continuously increased. Figure 2.6 shows the relation between coercivity and particle size. Also using a low-temperature auto-combustion method, cobalt ferrite nanoparticles were prepared by Xiao et al. [77]. The saturation magnetisation Ms, the remnant magnetisation Mr, and the average particle size were found to be highly dependent upon the annealing temperature. Magnetic cobalt ferrite nanoparticles were synthesised by Maaz et al. employing a wet chemical method [78]. The size of these nanoparticles was found to be dependent on annealing temperature and time due to coalescence. They found that for smaller particles the saturation magnetisation had a value that was significantly lower than the bulk value while the larger sized particles had values approaching those of the bulk.

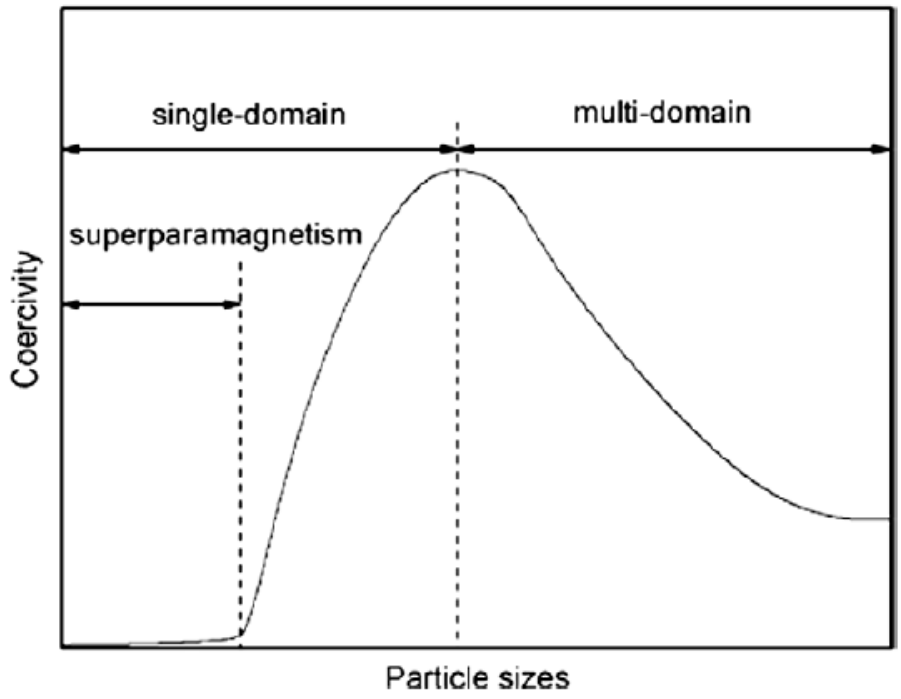

Figure 2.6 General relation between coercivity and particle size [28]

The saturation magnetisation Ms of powders is generally smaller than the bulk value and is found to decrease invariably when decreasing the particle size [72, 79]. However, when the particle size exceeds a critical diameter, multi-domain particles will usually predominate. In single-domain particles, where the particle size does not exceed the critical diameter, the spins of electrons near to the surfaces of the particles are disordered compared with those in the particle core. This is considered to be one of the surface effects that contribute to decrease the saturation magnetisation, Ms [80, 81]. Coercivity, Hc, is found to increase with decreasing particle size until a maximum value that is reached at the critical diameter corresponding to the transition stage from the multi to the single domain state. This is followed by a decrease to zero in the superparamagnetic state [28, 59, 77, 82, 83]. In the experimental arrangement described in Figure 2.6 the coercivity of cobalt ferrite nanoparticles was found to attain a maximum value at 29 nm as shown in Figure 2.7 [72].

2.3.5.2 Doped nanoparticles

The magnetic properties are not only dependent on the average particle size, the size distribution and the morphology of the particles, but also on changes in the intrinsic divalent and trivalent cation distribution between the tetrahedral and octahedral sites at

the nano scale. Tahar et al. prepared Sm- and Gd-substituted $CoFe_2O_4$ nanoparticles using forced hydrolysis in polyol [84]. The main magnetic characteristics appeared to be directly dependent on Sm^{3+} or Gd^{3+} content. A significant increase in the saturation magnetisation was achieved by doping with these magnetic ions. The magnetic properties appear to be sensitive to the cation distribution between the octahedral and tetrahedral sites.

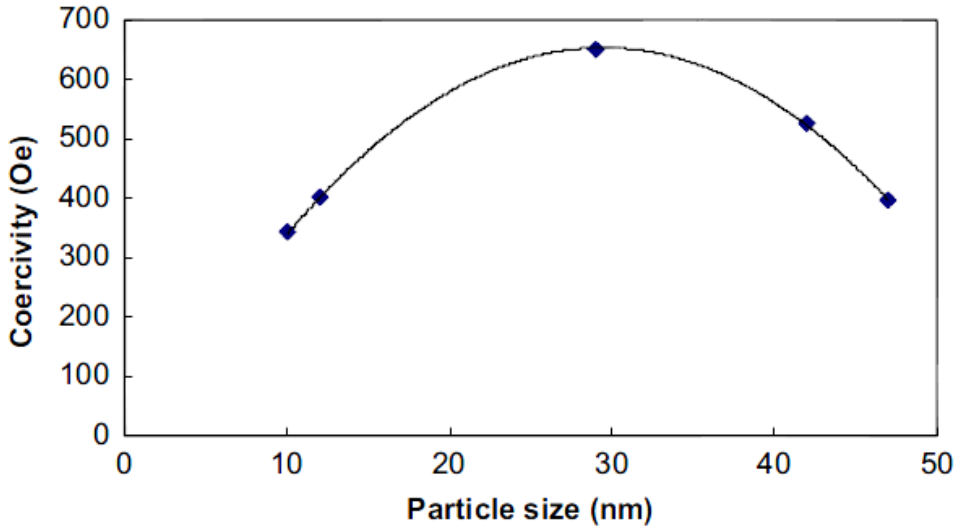

Figure 2.7 The relation between coercivity and cobalt ferrite particle size [72]

Gul et al. synthesised ferrite nanoparticles of $Co_{1-x}Ni_xFe_2O_4$, with x varying from 0.0 to 0.5, by the co-precipitation method [85]. The particle sizes were in the range of 14 – 21 nm. The Curie temperature was found to increase with Ni concentration in the structure. Both coercivity and saturation magnetisation were found to decrease linearly with increasing Ni-concentration in cobalt ferrite. The decrease in coercivity was attributed to the lower magnetocrystalline anisotropy of Ni^{2+} as compared to that of Co^{2+} ions. The decreasing trend in magnetisation with increasing Ni-concentration was attributed to the smaller magnetic moment of Ni^{2+} ($2\mu_B$) at the octahedral sites as compared to the Co^{2+} ($3\mu_B$). The blocking temperature as determined from the zero field cooled (ZFC) magnetisation curve showed a decreasing trend with increasing Ni-concentration in cobalt ferrite nanoparticles. It was believed to be related to the magnetocrystalline anisotropy of ferrites [86].

Cobalt ferrite nanoparticles doped with Mn^{2+} have been synthesised by a polyethylene glycol-assisted hydrothermal method [87]. PEG-400 was used as a

surfactant to prevent agglomeration. The blocking temperature, coercive field and remnant magnetisation were found to decrease with the increase in Mn content in the structure, while the saturation magnetisation was found to increase. Chromium doped cobalt ferrite nanoparticles have also been synthesised by polyethylene glycol (PEG) assisted hydrothermal route [88]. Since Cr^{3+} (3 μ_B) has a weaker magnetic moment than Fe^{3+} (5 μ_B), the partial replacement of Fe^{3+} by Cr^{3+} ion caused a decrease in the saturation magnetisation and coercivity in addition to a slight reduction in particle size. The addition of chromium reduced the Ms by 14% and the coercive field by 23%. Superparamagnetic nanoparticles of Cr-substituted cobalt–zinc ferrite ($Cr_xCo_{0.5-x}Zn_{0.5}Fe_2O_4$) with particle size < 10 nm, have been synthesised by a co-precipitation method [89]. The particle size, as well as the blocking temperature, decreased with increasing Cr concentration.

Cojocariu et al. prepared Cr- and Mn-substituted $CoFe_2O_4$ nanoparticles employing the co-precipitation method [90]. Chlorides were used as precursors. They were dissolved in distilled water and heated to 60 °C. Aqueous NaOH was added to the solutions to precipitate the powders. The precipitate was washed with distilled water, filtered, dried at 70 °C for 12 h in air and finally heat treated in three steps at 400, 650 and 900 °C for 5 h. A small increase in each of the saturation magnetisation, coercivity and remnant magnetisation was observed in the doped ferrites in comparison with the undoped cobalt ferrite. From the spectroscopic measurements, it was found that Co^{2+}, Mn^{3+}, Cr^{3+} ions have strong site preference for octahedral sites. The small increase of saturation magnetisation was related to the oxidation state of the manganese ions as the Mn^{2+} have no particular preference for octahedral or tetrahedral sites.

Zn-substituted cobalt ferrite nanoparticles ($Co_{1-x}Zn_xFe_2O_4$) of a monodisperse distribution were for the first time successfully prepared via the forced hydrolysis method by Duong et al. [91]. Nanoparticles with an average size of 3 nm were in the superparamagnetic state at room temperature. The blocking temperature, T_B, decreased from 221 to 142 °K with increasing Zn substitution from x = 0 to x = 0.4. The saturation magnetisation was found to increase with the increase of Zn content in the ferrite structure. This was due to the Zn^{2+} ions with zero magnetic moment replacing ions on the tetrahedral A-sites resulting in the increase of the total magnetic moment. The determined Ms value of $CoFe_2O_4$ was found to be a small amount higher than values

previously reported, even with larger particle sizes. This indicated that the nanoparticles prepared by the forced hydrolysis route have a higher crystallinity than those prepared by other methods.

Cobalt ferrite nanoparticles have also been synthesised by the emulsion method [92]. According to the DTA/TG analyses, the pure material was present at or above 600 °C. The particle size was observed to increase with increasing Nd^{3+} content between 400 and 500 °C, while it decreased with increasing Nd^{3+} content between 600 and 800 °C. The substitution of Fe^{3+} ions by Nd^{3+} ions resulted in the decrease of saturation magnetisation from 53.4 emu/g, for the pure cobalt ferrite, to 28 emu/g, for ($CoFe_{1.8}Nd_{0.2}O_4$) and the increase of coercivity from 172 to 489Oe. Substituting a small quantity of Fe^{3+} ions on B sites by the Nd^{3+} ions was believed to cause the superexchange interactions in the spinel structure to decrease. This resulted in a decrease of the saturation magnetisation. The movement of domain walls was thought to be more difficult, due to the Nd^{3+} (content residing at) concentration increasing near grain boundaries, so that the coercivity increased.

2.3.6 The effect of surface layer on magnetic properties

Toksha et al. [82] synthesised cobalt ferrite nanoparticles by a method involving both sol–gel and auto combustion with a size range between 11 and 40 nm depending on the annealing temperature and time. The saturation magnetisation Ms measured at room temperature was found to decrease with decreasing particle size. This was thought to be related to the effects of a relatively non-reactive surface layer that has lower magnetic properties. The effect of this surface layer on the magnetic properties of the whole particle increases when the particle size is very small. This leads to a decrease in the total magnetisation. For particles with 15 nm as the average size and with maximum applied magnetic field of 12kOe, the coercivity in the hysteresis loop was measured at different temperatures. The coercivity measured at room temperature (1215Oe) was lower than the value measured at 77 °K (10.2kOe). It is thought that this was due to significant growth in the magnetic anisotropy at 77 °K preventing the alignment of the moments under the applied magnetic field.

A random canting of the particles' surface spins caused by competing antiferromagnetic exchange interactions at the surface was proposed and explained by

Coey [81]. Mössbauer-effect measurements on extremely small (6 nm) crystallites of γ-Fe_2O_3 showed that the spin configuration differs from the type found in large crystallites. It was proposed that the ions in the surface layer are inclined at various angles to the direction of the net moment. The ultrafine particles could be visualised as having a core with the normal spin arrangement and a surface layer in which the spins of the ions are inclined at some angle to their normal direction, which depends on their magnetic nearest neighbours. Parker et al. [93] reported data demonstrating that the observed canting in γ-Fe_2O_3 nanoparticles (25 to 100 nm) is not a surface effect, but a finite-size effect. The surface spins still exhibit a weaker exchange than is found in the core states. Polarised neutron powder diffraction data of finely divided $CoFe_2O_4$ particles coated with oleic acid and uncoated were analysed by Lin et al. [94]. They confirmed the existence of a magnetically disordered surface layer in both coated and uncoated particles. These layers are approximately 16.9 Å thick in the uncoated particles and approximately 12 Å thick in the coated particles.

Martínez et al. [95] demonstrated the existence of a spin-glass-like surface layer that undergoes a magnetic transition to a frozen state below 42 °K in γ-Fe_2O_3 magnetic nanoparticles (9-10 nm). The core of the particle was found to be ferrimagnetic that changes its orientation by coherent rotation. The spin-glass-like surface layer slowly relaxes in the direction of the field. The origin of this spin-glass-like phase at the surface could be the existence of broken bonds and translational symmetry breaking of the lattice, generating randomness in the exchange interactions that extends to some atomic layers from the surface. The thickness of spin-glass-like surface layer is evaluated to be around 6 Å by using the random-field model of exchange anisotropy. The low temperature increase of Hc was observed and it is due to the pinning effect of the frozen spin-glass-like surface layer upon the single-domain core.

High field irreversibility in the moment versus field and moment versus temperature of coated $NiFe_2O_4$ nanoparticles with as average size as determined from x-ray diffraction data (65 Å) was observed. The onset temperature of this irreversibility is near 50 °K. It was proposed that the canted spins are on the particle surfaces. They freeze and form a spin-glass-like phase at temperatures below 50 °K. The surface spins have multiple stable configurations for any orientation of the core magnetisation, one of which is selected by field cooling [80].

Mössbauer studies of small $CoFe_2O_4$ particles revealed that a non-collinear spin arrangement exists, possibly at or near the surface of $CoFe_2O_4$ particles [96]. The particle morphology is an important factor influencing the non-collinear magnetic structure in fine particles. Mössbauer spectra at 4.2 °K were taken. Two overlapping six-line hyperfine patterns corresponding to the ^{57}Fe in B and A sites have been fitted. Mössbauer spectra were also taken with a large magnetic field 50kOe applied along the propagation direction of the γ rays at 4.2 °K. The atomic moments lie along the direction of the external magnetic field, and the polarisation conditions require the disappearance of the second and fifth lines in the hyperfine pattern. The Fe spins in small $CoFe_2O_4$ particles are canted with respect to the direction of the external magnetic field since substantial second and fifth absorption lines are obviously present as shown in Figure 2.8. This trend increases in smaller particles and is less pronounced in larger particles. From the value of the relative intensity of the 2,5 line areas compared to the 1,6 line areas, the thickness of the spin-canted surface layer of each crystallite was evaluated.

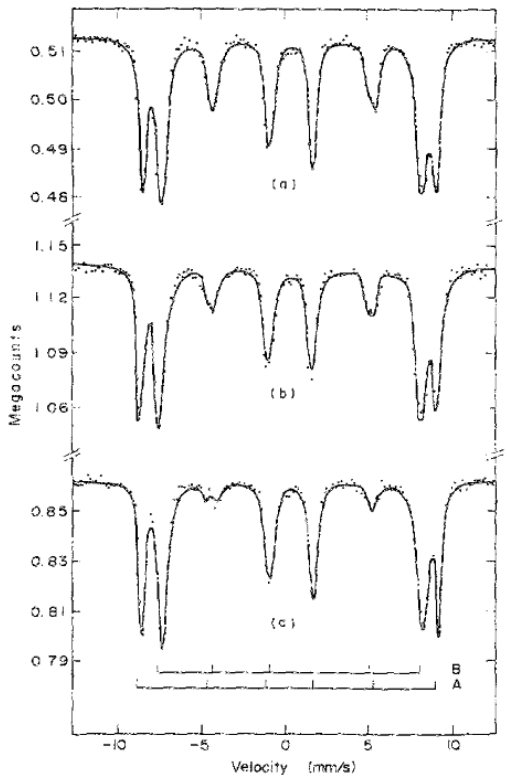

Figure 2.8 Mössbauer spectra of small $CoFe_2O_4$ particles taken at 4.2 °K in a longitudinal external magnetic field of 50kOe for three different samples [96]

2.3.7 The net magnetisation of cobalt ferrite

Cobalt ferrite particles were prepared by co-precipitation of iron and cobalt hydroxide. The precipitate was washed thoroughly, fired in a furnace at 1200 °C for 48 h and slowly cooled down to room temperature. The quenched material was obtained by quenching the powder at 1200 °C in water. A calculation of the magnetic moments, assuming that all the Fe^{3+} ions have a moment of 5 μ_B and the Co^{2+} ions have a moment of 3 μ_B, gives 3.16 μ_B and 3.84 μ_B per unit chemical formula for the slowly cooled and the quenched material, respectively [15].

Mössbauer spectra of $CoFe_2O_4$ showed that this spinel is not completely inverse and that the degree of inversion depends on the heat treatment of the material. The magnetic moments of the slowly cooled and the quenched material were 3.4 and 3.9 μ_B per unit chemical formula, respectively, in reasonable agreement with the calculated values.

The net magnetisation of a ferrimagnetic material depends on cation distribution between the octahedral and tetrahedral sublattice sites. Thus, the knowledge of cation distribution is important to understand the magnetic properties of nanoparticles. In cobalt ferrite each tetrahedral Fe^{3+} ion is surrounded by twelve octahedral ions. The replacement of one Fe^{3+} ion by a Co^{2+} ion at a B site probably does not produce a large-enough percentage change in the total superexchange interaction to cause a considerable difference in the ionic moments at higher temperatures. On the other hand an octahedral Fe^{3+} ion has only six tetrahedral nearest neighbors. If a tetrahedral Fe^{3+} ion is replaced by a Co^{2+} ion, the superexchange interaction will be reduced by an appreciable percentage. For instance, an Fe^{3+}(B) with (5Fe, 1Co) nearest A neighbours would have a more rapid decrease of the moment than one with (6Fe) nearest A neighbours. The Mössbauer spectra at higher temperatures showed broader lines whereas the broadening depends on the number of probable distributions of the iron and cobalt ions in the six nearest-neighbours A-sites. The hyperfine magnetic fields at B-site nuclei have different temperature dependences for different distributions of iron and cobalt ions in neighbouring A-sites.

Concas et al. [97] reported that the inversion degree of $CoFe_2O_4$ prepared via the sol–gel process may be evaluated using saturation magnetisation at 4.2 °K and

Mössbauer spectrum. The particle size and the thermal history are responsible for the inversion degree attained with respect to both the maximum temperature of heat treatment and the cooling rate.

2.3.8 Ferrimagnetism and superparamagnetism

Cobalt ferrite single-domain nanoparticles are known to be either in the ferrimagnetic or superparamagnetic state. In these particles, magnetisation can randomly flip direction under the influence of temperature. The typical time between two flips is called the Néel relaxation time. In the absence of an external magnetic field, when the time used to measure the magnetisation of the nanoparticles is much longer than the Néel relaxation time, their magnetisation appears to be, on average, zero. The state of these nanoparticles appears to be superparamagnetic. Furthermore, an external magnetic field is able to magnetise the nanoparticles, similarly to a paramagnet. However, the magnetic susceptibility (the degree of magnetisation of a material in response to an applied magnetic field) of these nanoparticles is much larger than that of paramagnets.

On the other hand, when the time used to measure the magnetisation of the nanoparticles is much smaller than the Néel relaxation time, their magnetisation will not flip during the measurement so the magnetisation measured will be the net of magnetic moments carried by the nanoparticles. They are said to be in the ferrimagnetic state. A transition between superparamagnetism and ferrimagnetism occurs when the measurement time equals the Néel relaxation time.

In other words, if the measurement time is kept constant and the magnetisation is seen as a function of the temperature, the temperature of the transition from superparamagnetism to ferrimagnetism is called the blocking temperature. The blocking temperature TB is known as the temperature at which the magnetic anisotropy energy barrier of a nano magnet is overcome by thermal activation, leading to the fluctuation of its magnetisation. (A magnetically anisotropic material will align its moment with one of the easy axes. An easy axis is an energetically favourable direction of spontaneous magnetisation). According to the Néel theory [84] the blocking temperature is expected to increase with K1, the magnetocrystalline anisotropy constant, and/or V, the average particle size. (The spin-orbit interaction (any interaction of an electron's spin with its

motion) is the primary source of the magnetocrystalline anisotropy. Spin-orbit interaction causes shifts in an electron's atomic energy levels (electrons in atoms and molecules can change energy levels by emitting or absorbing a photon whose energy must be exactly equal to the energy difference between the two levels) due to electromagnetic interaction between the electron's spin and the magnetic field generated by the electron's orbit around the nucleus). Above the blocking temperature TB, there is neither remanence nor coercivity and therefore no hysteresis feature, in agreement with the superparamagnetic character of the particles. Below the blocking temperature TB, $CoFe_2O_4$ nanoparticles exhibit ferrimagnetic behaviour characterised by hysteresis loops with coercivity, remanence and a saturation magnetisation.

Cobalt ferrite nanoparticles in the size range 5 to 7 nm for the use of magnetic fluid hyperthermia mediator were prepared by the successive polyol technique [42]. The Zero-field-cooled (ZFC) magnetisation curve in the temperature range (2.5-300 °K) showed a peak which refers to the mean blocking temperature TB of the assembly which was found to increase invariably with particle size. The coercive fields Hc recorded at 2.5 °K showed a decrease with decreasing particle size. At room temperature, there was no hysteresis feature observed which represents the nature of the superparamagnetic state. The same behaviour was observed in cobalt ferrite nanoparticles with an average particle size of 3 nm [51].

Moumen et al. [68] reported the superparamagnetic behaviour at room temperature for cobalt ferrite nanoparticles with 5 nm as an average particle size. A hysteresis feature was observed at a temperature of 20 °K for the same particles with a coercivity of 8.8kOe and this value decreased to 4.8kOe by decreasing the diameter of the particles from 5 to 2 nm. The details of the method of preparation of these nanoparticles for the magnetic fluid are reported elsewhere [98].

Cobalt and nickel ferrite nanoparticles with spherical-like morphology have been obtained by a solvothermal method with a size range between 5 and 10 nm [99]. An alcohol is used as both a solvent and a ligand. Cobalt ferrite nanoparticles suspensions were found to be stable in hexanol for more than one week, while the corresponding suspensions in benzyl alcohol precipitated in less than one day. The particle size of cobalt ferrite was observed to increase from 7.6 to 8.9 nm with the increase of reaction time from 24 h to 48 h, respectively. These nanoparticles were

found to exhibit superparamagnetic behaviour at room temperature. Saturation magnetisation was found to increase from 50.2 to 58.4emu/g with an increase in particle size from 5.9 to 8.9 nm.

Mössbauer spectroscopy can record the sextet hyperfine structure if the magnetisation of the nanoparticles does not flip during the measurement time which means that the relaxation time is longer than the measurement time. When the relaxation time is shorter than the measurement time, i.e. in a superparamagnetic state, only doublet spectrum is observed and this usually happens when the energy barriers in the nanoparticles are thermally overcome [100]. Li and Kutal recorded Mössbauer spectra for cobalt ferrite nanoparticles [66]. Results indicated that the intensity of the sextet pattern decreases with decreasing particle size while that of the central doublet increases. It has been shown that a stage exists in the transition from the ferrimagnetic to the superparamagnetic state when the particle size decreased from 10.5 to 6.3 nm. The hyperfine field at A and B sites was found to increase with decreasing particle size.

Cobalt ferrite nanoparticles have been synthesised in a homogeneous aqueous solution without any template and subsequent heat treatment [101]. The size of particles increased with the precipitation temperature. A particle size range between 2 and 15 nm was obtained when the precipitation temperature was in the range between 20 and 80 °C. The nanoparticles prepared at 20 °C and 40 °C were superparamagnetic at room temperature while those prepared at 60 °C and 80 °C were ferrimagnetic with magnetisation values at 10kOe of 36.0 and 58.3 emu/g and coercivity values of 39 and 193Oe, respectively. Mössbauer spectra recorded for nanoparticles prepared at 60 °C and 80 °C showed a complex hyperfine structure in which a quadrupole doublet is superimposed on a magnetically split sextet. These results could be explained by assuming that the samples being analysed can exist with two components of particles, one consisting of superparamagnetic particles, and the other of ferrimagnetic particles because of their wide particle size distribution. The blocking temperature of nanoparticles prepared at 80 °C was found to be around 550 °K.

2.4 The sol–gel technique

2.4.1 Introduction

The sol–gel technique is a versatile solution process for making advanced materials, including ceramics and organic-inorganic hybrids. In general, the sol–gel process involves the transition of a solution system from a liquid "sol" (mostly colloidal) into a solid "gel" phase. Utilising the sol–gel process, it is possible to fabricate advanced materials in a wide variety of forms: ultrafine or spherically shaped powders, thin film coatings, fibres, porous or dense materials, and extremely porous aerogel materials.

The sol–gel process, known as inorganic polymerisation, was discovered in 1846 by Ebelmann [102]. In practice, the sol–gel process is very simple at the macroscopic scale. It transforms a molecule into a material ready for shaping in one step. At the nanoscopic and microscopic scales, it is in fact a very complex process involving several transformations of very different natures of matter.

A colloid is a suspension in which the dispersed phase exhibits Brownian motion, a random movement driven by the momentum imparted by collisions with molecules of the suspending medium. A sol is a colloidal suspension of solid particles in a liquid. This type of colloid can be used to generate polymers or particles from which ceramic materials can be made. A ceramic is usually defined to be nonmetallic and inorganic. In the sol–gel process, the precursors for the preparation of a colloid consist of a metal or metalloid element surrounded by various ligands. Common precursors for any oxide include inorganic salts such as nitrates or chlorides and organic compounds such as alkoxides.

An alkane is a molecule containing only carbon and hydrogen linked exclusively by single bonds group. The general formula is C_nH_{2n+2}. An alkyl group, being a component of a molecular structure, but not necessarily having an existence on its own, is a ligand formed by removing one hydrogen from an alkane molecule. For instance, methane (CH_4) produces the methyl group (CH_3). An alcohol is a molecule formed by adding a hydroxyl (OH) group to an alkyl group, as in methanol ($OHCH_3$). An alkoxy group is a ligand formed by removing one hydrogen from the hydroxyl group of an

alcohol, as in methoxy (OCH_3). Metal alkoxides are members of the family of metalorganic compounds, which have an organic ligand attached to a metal or metalloid atom.

The sol–gel process involves hydrolysis and condensation reactions of metal precursors (salts or alkoxides) leading to the formation of a three-dimensional inorganic network. Metal hydroxyl groups (M-OH) are formed during the hydrolysis. These groups subsequently condense into strong, rigid and irreversible metal-oxo-metal bridges (M-O-M) [103-105].

Metal alkoxides are popular precursors because they react readily with water. The reaction is called hydrolysis, because the hydroxyl group in the water becomes attached to the metal atom, as in the following reaction:

$$M(OR)_2 + H_2O \rightarrow HO\text{-}M\text{-}OR + ROH$$

Where OR represents an alkoxy group and ROH represents an alcohol. Depending on the amount of water, hydrolysis may go to completion immediately.

$$M(OR)_2 + {}_2H_2O \rightarrow M(OH)_2 + {}_2ROH$$

Alternatively, partially hydrolysed molecules can link together in a condensation reaction.

$$M_2(OR)_2 + HO\text{-}M_1\text{-}OR \rightarrow (OR)M_2\text{-}O\text{-}M_1\text{-}OR + ROH$$

This can be hydrolysed, for instance,

$$(OR)M_2\text{-}O\text{-}M_1\text{-}OR + H_2O \rightarrow (OH)M_2\text{-}O\text{-}M_1\text{-}OR + ROH$$

This type of reaction can continue to build larger and larger metal or metalloid-containing molecules by the process of polymerisation. For instance,

$$M_3(OR)_2 + (OH)M_2\text{-}O\text{-}M_1\text{-}OR \rightarrow (OR)M_3\text{-}O\text{-}M_2\text{-}O\text{-}M_1\text{-}OR + ROH$$

A polymer is a huge molecule formed from thousands of units called monomers that are capable of forming at least two bonds. An oligomer is a molecule of intermediate size between a polymer and a monomer. The number of bonds that a monomer can form is called its functionality, f. If a polyfunctional unit with $f > 2$ is

present, the chains can be joined by crosslinks to form a three-dimensional structure. There will be no limit on the size of the molecule that can form.

If one molecule reaches macroscopic dimensions so that it extends throughout the solution, the substance is believed to be a gel. It is a substance that contains a continuous solid skeleton enclosing a continuous liquid phase. Gelation can occur after a sol is cast into a mold, in which case it is possible to make objects of a desired shape. Bond formation does not stop at the gel point. The network is initially compliant, so segments of the gel network can still move close enough together to allow further condensation. Smaller polymers or particles continue to attach themselves to the network.

Drying by evaporation under normal conditions results in a dried gel called a xerogel. Most gels are amorphous, even after drying, but many crystallise when heated. The final heat treatment pyrolyses the remaining organic or inorganic components and forms the crystalline powder. This, of course, is especially useful if the gel only contains the substance which one is attempting to prepare, and substances that can be removed by oxidation or evaporation. If it contains other substances, these must be removed by washing before the evaporation.

If this is carried out with precursors to yield cobalt ferrite, the xerogel would be a dry solid containing the cobalt ferrite in an amorphous form. The structure would still contain the remains of the original linkages of the polymer chains or skeleton, and these linkages might be arranged randomly in all directions. Heating the xerogel gives to the components, particularly the cobalt and ferric ions the possibility of migrating to sites to reduce the internal energy of the solid. Therefore on heating ions will migrate to the most favourable sites, forming close packed structures with the maximum neutralisation of electrostatic charges, regardless of the original structure of the polymer. This is why crystals of cobalt ferrite grow. However by controlling the amount of heating, the rate of this process can be controlled and stopped when the crystals are still very small.

2.4.2 Nanoparticles synthesis

Among the various liquid-phase chemical techniques, reported in the literature and employed for the synthesis of cobalt ferrite nanoparticles, the sol–gel process is probably the most effective being a feasible route to achieve high purity and

homogeneity and develop crystalline nanoparticles. This process offers the possibility of a generalised approach to the production of both single and complex oxide nanoparticles [106].

The sol–gel method has been employed to fabricate $CoFe_2O_4$ particles by Lee et al. to be used as high-density magnetic recording media [107]. The typical spinel structure was obtained when powders were annealed at or above 350 °C. The increase in the annealing temperature yielded an increased sharpness of the major peaks of XRD patterns, indicating the growth of larger particles. A decrease in the coercivity and, in contrast, an increase in the saturation magnetisation was observed with the increase of annealing temperature. The magnetic behaviour was found to be related to the size of crystalline particles and the temperature of measurement. Particles annealed at 350 °C were found to be in the ferrimagnetic state at room temperature with a size range between 6 and 20 nm. Some particles were in the superparamagnetic state, existing side by side with those in the ferrimagnetic state.

Nanoparticles of cobalt ferrite having an average particle size of 40 nm were also synthesised employing the sol–gel method [108]. Cobalt and ferric nitrates were used as precursors with ethylene glycol as the solvent. The temperature of the sol was increased up to 60 °C to obtain a wet gel which was then dried at 90 °C. The amorphous powder was annealed at 800 °C during the heat treatment process by which the crystalline nanoparticles were obtained. The coercivity and remnant magnetisation were found to increase in value when decreasing the temperature of measurement down to 100 °K. These nanoparticles were found to be in the ferrimagnetic state at room temperature.

Cobalt ferrite nanoparticles doped with aluminum $CoFe_{2-x}Al_xO_4$ (for x = 0.00, 0.25, 0.50) have been synthesised by the sol–gel route [109]. The precursors were dissolved in de-ionised water. Citric acid was added to the prepared aqueous solution to chelate the metal ions. A solution of ammonia was added to neutralise the solution. Drying was carried out by heating at 100 °C. The powder was then annealed at 800 °C for 6 h with a heating up rate of 5 °C/min to obtain the spinel phase. The crystallite size as calculated using the Scherrer formula was in the range 18-23 nm. It decreased with increasing concentration of Al^{3+} ions. The lattice parameter and the Curie temperature were found to decrease as well with increasing concentration of Al^{3+} ions. The decrease

in lattice parameter was thought to be due to the substitution of the smaller Al^{3+} ions (0.51 Å) in place of the larger Fe^{3+} ions (0.64 Å) in the system. The decrease of Curie temperature from 667 to 528 °K with the increase in Al^{3+} concentration was explained as a result of the modification of the A–B interaction strength due to the change of Fe^{3+} concentration between A and B sites, reducing thereby the A–B superexchange interaction. The powder was dried and annealed at 550 °C for 8 h in a separate investigation reported elsewhere [110]. The highest value of saturation magnetisation and coercivity was observed for the pure cobalt ferrite and it decreased as the aluminum content increased in the structure.

Chromium substituted cobalt ferrite nanoparticles ($CoCr_xFe_{2-x}O_4$, $0 \leq x \leq 1$) have been synthesised using the sol–gel auto combustion method [111]. The precursors were dissolved separately in distilled water. The individual solutions were then mixed together and the pH value of the solution was adjusted to about 6. The solution was then slowly heated and stirred until gels were formed. The resultant powder was annealed at 400, 600 and 1000 °C for 2 h to obtain the crystalline nanoparticles. The value of saturation magnetisation was found to decrease from 77 to 13emu/g with the increase of Cr^{3+} concentration in the structure. This was believed to be due to the smaller magnetic properties of the Cr^{3+} ions substituting for the Fe^{3+} ions in the octahedral sites. This resulted in the weakening of the A–B superexchange interaction. The value of coercivity decreased with the increase in Cr^{3+} concentration. This was attributed to the decrease in the anisotropy field. The lattice parameter was found to decrease slightly with the increase of Cr^{3+} concentration because the ionic radii of the Cr^{3+}(0.63 Å) and the Fe^{3+}(0.67 Å) ions are almost the same.

Cu doped Co ferrite nanoparticles ($CoFe_{2-x}Cu_xO_4$, $0.0 \leq x \leq 0.5$) have been prepared by the sol–gel method [112]. Metal nitrates were used as precursors. They were dissolved in de-ionised water and a few drops of ethyl alcohol were added. The solution was constantly stirred until the gel formation. The temperature was kept at 65 °C during stirring. The formed gel was annealed at 200 °C for 24 h to form a fluffy loose powder. The resultant powder was then heated to, and maintained at, 800 °C for 8 h to remove any organic residuals present in the material with 10 °C/min as the heating up and the cooling down rates. The lattice constant was found to increase with increasing concentration of Cu^{2+}. This was thought to be due to the difference in the

ionic radii between the Cu^{2+} ions (0.70 Å) and the Fe^{3+} ions (0.67 Å). The saturation magnetisation was found to decrease with Cu^{2+} doping. The reason was related to the smaller magnetic moment of Cu^{2+} ($1\mu_B$) as compared with the Fe^{3+} ions ($5\mu_B$). Dysprosium doped Co–Zn ferrites were synthesised by a sol–gel auto combustion method reported in detail elsewhere [113]. The particle sizes were found to be in the range between 30 and 40 nm. The lattice constant decreased with increasing Dy concentration while the sizes of the particles increased.

The sol–gel process has been employed to prepare composite materials containing highly dispersed magnetic cobalt ferrite nanoparticles as core particles in a silica matrix [114, 115]. The cobalt ferrite nanoparticles were observed to interact with the silica matrix through Si–O–Fe bonds according to the IR spectrum. This interaction reaches its maximum when the temperature is raised to 600 °C. Above this temperature, the interaction disappeared with the breakage of the Si–O–Fe bonds [116]. Silva et al. has found that the size of cobalt ferrite particles formed in the silica matrix increases with an increase in the heat treatment temperature, leading to an increase in the saturation magnetisation and coercivity [117]. Particles stopped exhibiting superparamagnetic behaviour above 400 °C when the particle size reached approximately 10 nm.

$CoFe_2O_4$ nanoparticles embedded in an amorphous SiO_2 matrix with a size range between 3 and 15 nm have been synthesised by the sol–gel method [118]. Coercivity was found to increase with particle size. Due to the wide size distribution of the $CoFe_2O_4$ particles which were annealed at 1000 °C, the simultaneous occurrence of both sextet and doublet spectra were detected at room temperature. Particles annealed at 900 °C were all superparamagnetic as indicated by Mössbauer spectroscopy. A deviation from the ideal inverse spinel structure was observed.

2.4.3 Other applications

The sol–gel process has been employed to prepare nanocrystalline $CoFe_{1.9}RE_{0.1}O_4$ [Where RE refers to a rare earth element, which can be either Gd, Tb or Dy] films [119]. Doping with magnetic RE ions was found to increase the coercivity of the cobalt ferrite. Cheng et al. used the sol–gel method to prepare nanocrystalline thin films of cobalt ferrite with doping with foreign ions [120]. The morphology and grain

size of the thin films were dependent on the annealing temperature. The magnetisation, the high coercive force and the sizes of the nano grains obtained make the technique a promising approach for recording applications. Lee et al. prepared porous cobalt ferrite magnets using a sol–gel process in which polymer colloidal spheres were used as sacrificial templates to enable 3-D ordered pores to be formed [121]. The porous cobalt ferrite showed enhancements in coercive field and magnetisation compared with the bulk congener. Preliminary experiments have shown that porous cobalt ferrites can separate magnetic ions selectively from a solution containing various magnetic and non-magnetic ions.

2.5 Sintering

2.5.1 Introduction

Sintering is the process whereby the pores between particles or grains are eliminated. Before sintering these pores exist in the body of a specimen which has been pressed or formed into a definite shape. Sintering causes the shrinking of the shape of the body, with the shrinkage being driven by surface tension. It is achieved by raising the temperature of the material to almost the melting point, so that the surfaces of the grains become soft, and begin to show the characteristics of a liquid. In the process, some of the grains grow, while others decrease in size and disappear altogether. The initially random convex shapes of the grains also change, causing the surfaces to become more flat, so that each grain fits into place with its surrounding neighbours with no space between. This causes the elimination, or almost causes the elimination of the pores between the grains. The most general form of industrial sintering consists in the following stages: a non-isothermal heating up period until the sintering temperature is reached; an isothermal “dwell” period during which the sintering temperature is maintained until the maximum density is reached; a relatively slow cooling down period to room temperature.

It has been suggested that the rate of sintering activity of ferrite powders can be improved by two main routes. The first is the preparation of powders with nano-sized particles which should result in higher surface energy in the pressed compact specimen prior to sintering, and thus provides a higher driving force for densification and grain growth [122]. It is true that compacts containing nano-sized particles begin to sinter at

much lower temperatures. The second is the addition of sintering additives [123]. Different sintering additives have been proposed to enhance the densification behaviour of Ni-Cu-Zn ferrites, e.g. PbO [124]. Densification at low temperatures, bismuth oxide Bi_2O_3 has been used [125].

The changes in dimensions, which normally occur during sintering, are measured as length or volume changes before and after sintering as follows:

$$\Delta l = l - l_0 \quad or \quad \Delta V = V - V_0$$

The zero (value) suffix refers to the original state.

Since shrinkage occurs, the length and volume changes are negative

From these, as a percentage, the linear or volume expansion is determined as follows:

$$S_L = \frac{\Delta l}{l_0} . 100 \quad or \quad S_V = \frac{\Delta V}{V_0} . 100$$

Again, negative values refer to shrinkage.

Shrinkage curves are measured using a high-temperature Dilatometer. They show the effect of temperature and time. Because the shrinkage rate may be much slower than the heating up period, and the thermal conductivity of the material may be very low, different parts of the sample being tested may be at different temperatures, and so different rates of heating can produce different shrinkage curves. In the case of ferrites, the sintering atmosphere can also produce different effects. All of these factors need to be considered. In a Dilatometer test, the linear expansion/contraction movement is transferred directly to a low-friction probe placed in contact with the end of the specimen, and this enables the measurement to be made. The results of the measurements are recorded continuously, processed in the computer and shrinkage curves are produced.

2.5.2 The densification and grain growth

Generally, when increasing the sintering temperature, a shorter sintering time is sufficient to achieve the constant relative density. The point at which relative density reaches its maximum value coincides with the onset of nonuniform grain growth. In fact, in the early stages of sintering at a certain temperature, rapid densification occurs

with slow grain growth. However, when the relative density approaches its maximum value, grain growth begins to increase more rapidly while the rate of densification slows down. In addition, grain growth becomes more pronounced at higher sintering temperatures, but the effect on the densification rate is not so dramatic. This suggests that it is important to adopt a thermal cycle in which the temperature is increased to a high value with just a short dwell time employed at this temperature. That is to favour rapid densification. Subsequently, the temperature should be decreased and a second dwell time introduced, to encourage densification and discourage grain growth to the greatest possible extent, and enable the total densification process to approach values close to the theoretical density [126].

The feasibility of densification with the minimum of grain growth relies on the suppression of grain-boundary migration while keeping grain-boundary diffusion active. This has been called "The kinetic window" of opportunity. Grain growth is observed to be more prolific at a higher temperature. This suggests that grain-boundary migration may involve an activation process that has higher activation energy than grain-boundary diffusion. Therefore, it is more active at higher temperatures but is suppressed at lower temperatures. However, if the temperature is too low, grain-boundary diffusion may be suppressed and so the densification would be reduced. Doping with additives, e.g. Nb_2O_5 or MgO, has the effect of shifting the kinetic window to a higher or lower temperature respectively [71]. In one investigation, it was concluded that, by exploiting the kinetic window, it is possible to achieve dense, nano-structured materials of grain sizes between 25 and 50 nm starting from nano-sized powders in the size range between 5 and 10 nm. In the same way, in a separate report, fully dense cubic Y_2O_3 was prepared by a two-step sintering method. In the final-stage grain growth was suppressed by exploiting the difference in kinetics between grain-boundary diffusion and grain-boundary migration. The sample was firstly heated to a higher temperature to achieve an intermediate density, then cooled down and held at a lower temperature until it became fully dense [127].

Kumar et al. divided the sintering process of WC nano powders into four stages [128]. In the first stage, a rapid increase in the densification rate of the compact happens. The shrinkage has two components: one arising from inter-agglomerate and another from intra-agglomerate densification. The end densities increase to around 80%

from an initial density. At the end of this stage, most of the bridges between agglomerates disappear, the clusters impinge upon each other and a microstructure characterised mainly by agglomerate and continuous pore distribution is reached. The initial rapid shrinkage is followed by an almost constant density regime characterised by the clusters shrinking in upon themselves. The shrinkage of the compact, if any, occurs purely by intra-agglomerate densification. The microstructure evolves into well demarcated agglomerate boundaries. Following the formation of stable agglomerates, intra-agglomerate shrinkage cannot proceed further although sintering by grain growth occurs to a small extent. From this point, the sinterability of inter-agglomerate pores controls the densification rate. Many of the large pores are found to be surrounded by more than the critical number of grains. As a result, the net shrinkage strain rate decreases due to two simultaneous forces opposing densification: large co-ordination number with surrounding grains and a small amount of grain growth within the agglomerates. The relative density decreases since the large pores start to grow. Following the small dip in shrinkage strain rate, there is a passive period over which the system tries to evolve by massive grain growth within the agglomerates. This leads to a breakup of the agglomerate identity into large grains and the stable inter-agglomerate pores start to sinter. The pores start to shrink rapidly, surpassing the grain growth rate. The concurrent grain growth supports shrinkage until the open pores are eliminated and the closed pore structure appears.

2.5.3 Sintering of cobalt ferrite

$CoFe_2O_4$ powder prepared by a traditional ceramic route was pressed into discs and sintered under vacuum at a pressure of 10^{-5} Torr ($1.33*10^{-3}$ Pa) in a series of experimental trials [129]. In each trial the final density was measured. It was found to increase with an increase in either the sintering temperature or the dwell time. A relative density of 96.8% was achieved when sintering at 1200 °C for 24 h. The vacuum sintering resulted in the development of other oxides (CoO) which seemed to come into existence alongside the spinel structure, but were not part of it, due to the non-oxidising nature of the vacuum in the sintering environment, which had a reducing effect on the material. The reaction was due to the breakdown of the ferric part of the structure to produce oxygen:

$$CoFe_2O_4 \rightarrow CoO + Fe_2O_3$$

$$2Fe_2O_3 \rightarrow 4FeO + O_2$$

The first reaction is reversible, but, if it occurs on even a small scale, the second reaction will occur and it is not reversible because the oxygen would be carried away in the vacuum system. Once FeO is formed, it will react with any free Fe_2O_3 to form Fe_3O_4, and further destroy the structure of the cobalt ferrite.

The magnetostriction amplitude was reduced by the detrimental effect of these extra non-magnetostrictive oxides. The coercive field was found to decrease with increasing sintering temperature and time. Higher sintering temperature and longer sintering time were thought to result in larger grains and consequently a lower coercive field. Larger grains, on their own, would probably not reduce the magnetic properties. However, larger grains would produce poorer mechanical properties (poorer homogeneity and a loss in ductility). This could cause cracking as the specimen cooled (because of temperature gradients across the specimen leading to different rates of contraction), and the cracks would produce poorer magnetic properties. This is one major reason why one cannot achieve high densities simply by prolonging the sintering time or increasing the temperature.

In another study, cobalt ferrite powder was prepared by a solid-state reaction route. Uniaxially pressed disc samples, were sintered under one-step conditions in a series of experimental trials. These disc samples were made from powders with different particle size distributions. The sintering conditions were kept the same at 1450 °C for 3 h. In each case the final value of the relative density was measured, and when the average particle size of the starting material was 14.17 μm, the final relative density was 87.51%. The relative density after sintering was found to increase by around 4% when the average particle size of the starting material was 5.34 μm instead of 14.17 μm. No further increase in the relative density was observed when the particle size was further reduced [6].

The observed improvement in densification was explained to be due to the fact that open interconnected porosity had not been completely eliminated in the disc samples until the end of the sintering dwell time. However, when starting with powders with smaller average particle sizes, the densification process did not improve with the formation of specimens with even higher relative density. This was explained to be due

to the fact that, although the porosity still existed in the sample in regions far from the surface of the sample, the pores were no longer connected through the layers near the surface of the sample with the atmosphere in the sintering equipment. In other words the pores were no longer “open” but “closed”. Therefore, since the pores were filled with gas, there was no way for the gas to be expelled from the pores inside the sample and into the atmosphere of the sintering equipment.

It was concluded that decreasing particle size below 5.34 μm, coupled with a one-step sintering temperature profile, would not result in any further improvement in increasing the relative density.

It will be appreciated that when a sample is being heated up in a furnace, the temperature of its surface will always be higher than the temperature near the centre of the sample, because the heat is transferred from the sintering equipment to the sample mainly by radiation, and it reaches the centre of the sample by conduction. Since the thermal conductivity of ceramic samples is usually poor, there will be a significant difference between the temperature at the surface and the temperature near the centre of the sample. It follows that there will also be a significant difference in the rate of densification between the surface layers of the sample, and the regions underneath, near to the centre of the sample. As a result of this, the porosity near the surface will be lower than at the centre. Before the sintering process was started, the pores near the centre of the sample would have been connected to a network of passageways through the outer layers near the surfaces of the sample with the atmosphere surrounding the sample. However, during the sintering process, there is a danger that the porosity in the surface layers will be reduced so such an extent that the connecting passageways will become closed, isolating the pores deeper down in the sample and preventing them from communicating with the atmosphere surrounding the sample. The result of this is that the deeper pores become closed, and there is no way for the gas which fills them to be expelled from the material, and the porosity will remain unchanged whether the sintering time is extended, or the temperature increased.

A possible way to overcome this problem is to raise the temperature rapidly to a value where previous measurements have indicated that densification can take place. Then after a short dwell time the temperature is lowered again. During this cooling period, the centre of the sample will be at a higher temperature than the surface of the

sample. It follows that the rate of densification will also be greater at the centre of the sample than at its surface. It may be possible to design a temperature profile which allows the densification process at the centre of the sample to catch up on the densification process near the surface, and even to achieve lower levels of porosity at the centre compared with near the surface. Once this has been achieved, it will be safe to increase the temperature again and allow the pores near the surface to be eliminated, without the risk that pores deeper inside the sample are becoming blocked. The solution to the problem therefore involves a two-stage sintering operation.

This approach was adopted by the same investigators. The first stage was carried out at the temperature where previous measurements had indicated that the densification rate peak occurred. The second stage was carried out at 1450 °C. It had been anticipated that during the final stage of sintering, all of the porosity would have been eliminated, and this could have happened if all the pores had been connected to fast, short diffusion paths along grain boundaries. However, this sintering profile was applied to a rod prepared by micro-sized powders with 5.34 μm as the average particle size, although a slight increase in relative density was observed, with a final value around 92% being achieved, this result indicates that further refinement of the temperature profile may be necessary for still higher densities to be reached with successful removal of all porosity.

2.6 Summary

The magnetic properties of ferrites have been described in detail. However it is significant that they are determined not only by their chemical composition but also by their microstructure. Solution phase chemical methods to prepare cobalt ferrite nanoparticles are very diverse. The microemulsion method is a very promising technique for preparing monodisperse, ultrafine particles of controlled size and morphology. However, the sol–gel process is probably the most effective and feasible route to achieve high purity and homogeneity and develop crystalline nanoparticles. Most of the chemical methods to prepare cobalt ferrite nanoparticles produce amorphous powders. A heat treatment operation must be applied to the amorphous powders to obtain crystalline nanoparticles. The sizes of these nanoparticles are found to be mainly dependent on the temperature and the time of the heat treatment operation.

Sintering is the process which determines the features of the end-product microstructure. It involves heating the powder compact at a certain rate, and holding it at the highest temperature until the maximum density is reached. It is thought that the densification can be improved by the introduction of nanoparticles to replace micro-sized particles because this should result in higher surface energy in the material. Therefore, a more powerful driving force for densification would be available, but grain growth might still be a problem.

The requirements for investigating whether cobalt ferrite nanoparticles could overcome the difficulties encountered in sintering, can be achieved by introducing nanoparticles prepared employing the sol–gel technique. These nanoparticles must have a polydisperse size distribution. According to the literature, the maximum temperature adopted during the heat treatment process may have resulted in the unnecessary enlargement of the particles. This temperature needs to be reduced to a minimum value. With that aim in view, response surface methodology (RSM) is one of the optimisation techniques which analyses the quantitative data collected from experimental trials, predicts the responses of interest and finds their optimum values. It is used to simulate the heat treatment process and optimise it in order to specify the optimum conditions.

2.7 The contribution of the chapter towards the aims and scope of the investigation

The principal reason for investigating whether nano-sized particles of cobalt ferrite can be made remains the same. If particles with only a single magnetic domain can be made, there should be an opportunity to make discs and rods in which all the crystal axes are aligned in the same directions. This would change the magnetostriction characteristics significantly. As shown by Bozorth et al. [16], the magnetostriction of cobalt ferrite varies from a small positive value to a large negative one, depending on the alignment of the applied magnetic field with the crystal axis. Therefore when the crystal axes are not aligned, the overall magnetostriction observed is an average value because some of the parts of the sample are contracting and some are expanding, and the result is a small negative value. If rods could be fabricated with the crystal axes aligned, the magnetostriction in one direction could be almost as high as that shown by Bozorth et al. for a single crystal after magnetic annealing. While still not as high as

commercial samples of Terfenol D, it would be sufficiently close to make it a significant alternative to this material, especially when its other properties are taken into consideration.

However it is also true that the magnetic properties of rods of cobalt ferrite are often poor because of the difficulty in achieving a low porosity during sintering, when the starting material is micro-sized particles of cobalt ferrite. There are grounds for expecting that some of the difficulties encountered during sintering might be overcome if the starting material were to be nano-sized particles of cobalt ferrite. This is an entirely separate advantage of nanoparticles, and it is also of great importance.

It is therefore of great interest to know whether cobalt ferrite nanoparticles can be made which are sufficiently small to have only a single magnetic domain. However, the processes required to fabricate these nano-sized particles into discs or rods while maintaining their crystal axes aligned are expected to be very complicated and expensive and beyond the scope of this initial study. On the other hand the possibility that nano-sized particles might be able to overcome the difficulties encountered in sintering cobalt ferrite is also very interesting, and because it can be pursued without the same requirements for expensive equipment, it has been included in this investigation.

Chapter 3

Materials' characterisation

3 Materials' characterisation

3.1 Introduction

This chapter explains in a nutshell the methodology of the work that has been carried out and is presented in this thesis. It gives a brief introduction to the equipment that has been used to prepare the material (the cobalt ferrite nanoparticles) and perform the characterisation process. The work in this thesis can be divided into four main parts:

- The synthesis and characterisation of the cobalt ferrite nanoparticles
- The structural and magnetic analyses of the nanoparticles
- The modelling and optimisation of the heat treatment operation
- The sintering behaviour of the nanoparticles

3.2 Methodology

In this study, the sol–gel technique was employed and it was followed by a heat treatment operation to develop the cobalt ferrite nanoparticles. The parameters of the experiment have been systematically varied to investigate their effects on the morphology and other properties of the material being prepared. The heat treatment operation was modelled and optimised by means of DoE in order to achieve the best properties with the lowest electrical operating cost. Finally, the sintering behaviour of the nanoparticles was investigated in order to achieve the highest density.

3.3 Characterisation

A magnetic stirrer was used to prepare homogenous solutions before and after blending. This is shown in Figure 3.1. Drying was carried out using a laboratory oven shown in Figure 3.2. After the amorphous powders had been prepared, they were ground using the mortar and pestle shown in Figure 3.3. After drying the amorphous powders, A Horizontal Tube furnace (Carbolite Ltd., Sheffield, UK) was used to carry out the heat treatment operation on them with 10 °C/min as the heating/cooling ramp rates under ambient atmosphere. This is shown in Figure 3.4.

The structural characterization of all powders was carried out by measuring their XRD patterns employing an X-ray diffractometer (D8 ADVANCE-BRUKER) using Cu-K_α radiation. The equipment is shown in Figure 3.5. This method is used to determine the atomic and molecular structure of the resultant materials, in which the crystalline atoms cause a beam of X-rays to diffract into many specific directions. By measuring the angles and intensities of these diffracted beams, it can produce a picture of the density of electrons within the crystal. From this electron density, the mean positions of the atoms in the crystal can be determined, as well as their chemical bonds, their disorder and various other information. Every crystalline substance gives a pattern; the same substance always gives the same pattern; and in a mixture of substances each produces its pattern independently of the others. The X-ray diffraction pattern of a pure substance is, therefore, like a fingerprint of the substance. Figure 3.6 shows an example of XRD Pattern, the outcome of this method.

The equipment is connected to a computer with a package of associated software programmes called DIFFRAC PLUS Evaluation. One of these software programmes called EVA, which has a database of the XRD patterns of a comprehensive range of compounds arranged in the order of the periodic table with a significant number of their possible alloys, was used to determine the identity and provide an indication of the concentration of each phase in the samples. This is usually done by comparing the XRD patterns obtained by the equipment with that of pure cobalt ferrite taken from the database. If other phases are present, they will be shown as different lines in the spectrum, and also sometimes by the different sizes of the peaks in the pattern. Other possible candidate compounds can then be considered by comparing their XRD patterns as given in the database, with the extra lines obtained experimentally.

Figure 3.1 Magnetic stirrer

Figure 3.2 Drying oven

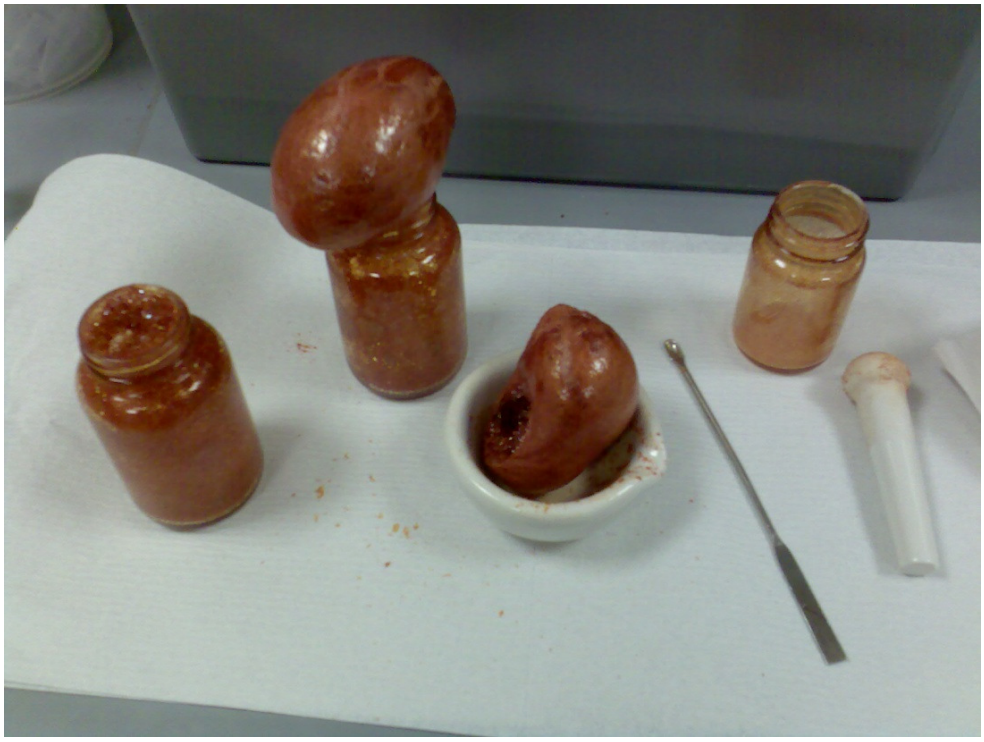

Figure 3.3 Mortar and pestle

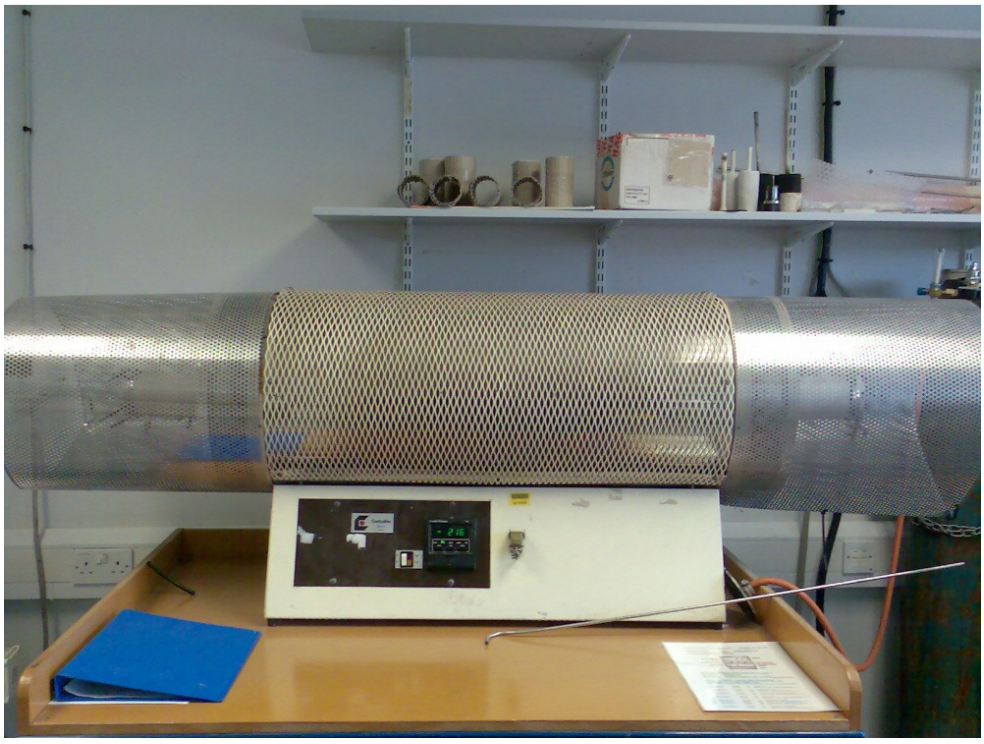

Figure 3.4 Horizontal tube furnace

DTA/TGA is a powerful thermo-analytical technique. It combines a DTA and a TGA into one instrument that performs both DTA and TGA on the same sample of amorphous powder at the same time. The resulting DTA and TGA curves are simultaneously plotted on a dual Y-axis graph so the DTA's fingerprint and the TGA's

weigh loss/gain characteristics are directly compared as the test sample is heated and cooled. The equipment is shown in Figure 3.7.

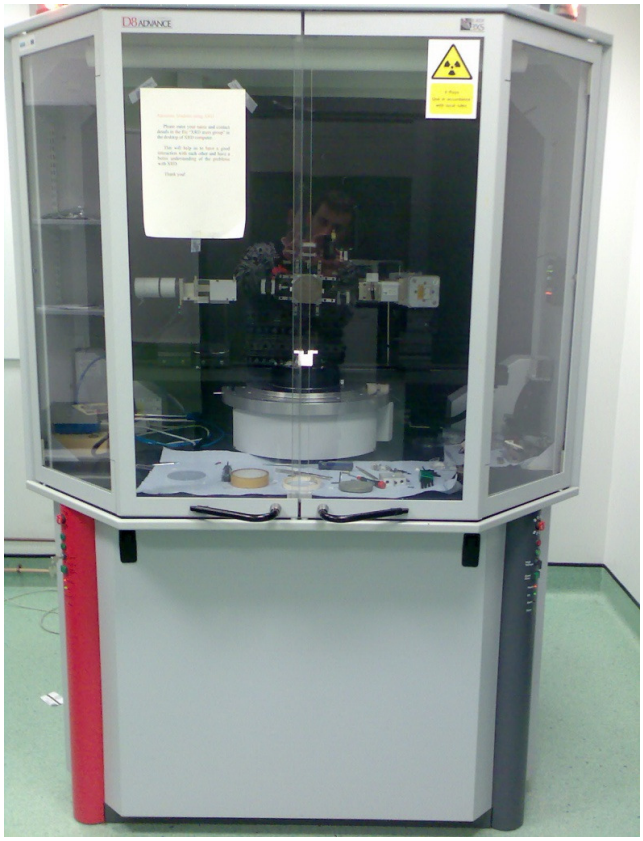

Figure 3.5 The XRD equipment

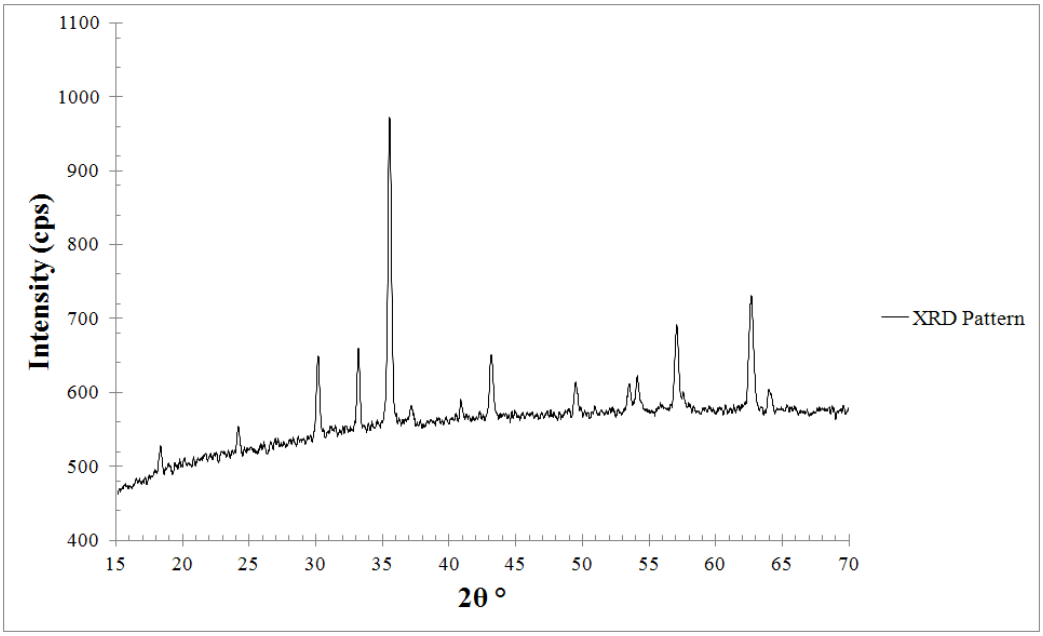

Figure 3.6 An example of XRD Pattern

Differential Thermal Analysis (DTA) and Thermo-Gravimetric Analysis (TGA) were performed in air to determine the temperatures at which the decomposition and oxidation of the crosslinker and the chelating agent take place. The curves were obtained using heating/cooling rates of 10 °C/min under ambient atmosphere to investigate and identify the purity of the materials. Figure 3.8 shows an example of a DTA/TGA graph.

Scanning Electron Microscope (SEM) is a type of electron microscope that produces images of a sample by scanning it with a focused beam of electrons. The electrons interact with electrons in the sample, producing various signals that can be detected and that contain information about the sample's surface topography and composition. The equipment is shown in Figure 3.9.

For conventional imaging in the SEM, specimens must be electrically conductive, at least at the surface, and electrically grounded to prevent the accumulation of electrostatic charge at the surface. Cobalt ferrite, as a nonconductive material, tends to charge when scanned by the electron beam which causes scanning faults. Therefore, samples of powders were coated with an ultrathin coating of electrically conducting material (gold) deposited on the sample by low-vacuum sputter coating.

The morphology of the materials (homogeneity and particle size) was observed by the SEM, and a chemical analysis was carried out using a Field Emission arrangement fitted to the Scanning Electron Microscope (FE-SEM). Figure 3.10 shows an example of SEM Image.

FTIR is the acronym for Fourier Transform Infrared Spectroscopy. FTIR is a spectroscopic technique that utilises lower energy radiation to induce vibrational and rotational excitation of atoms and groups of atoms within molecules. Because of the variety of symmetry of atomic groups and their differences in atomic masses and electronic structure, the absorption patterns for a specific species will be unique, which allows for their identification.

When photons interact with a molecule, the molecule may respond by absorbing the photons and subsequently the energy of the absorbed photons cause the molecule to vibrate in a higher energy level. In order to be infrared active, the dipole moment must change during a vibration. Absorption occurs when the incoming IR radiation that is

interacting with a molecule has sufficient energy to raise the vibrational energy level of the molecular system to the next allowed level. The frequencies of absorption are determined by the masses of atoms, the force constant of bonds, and the geometrical shapes of the molecule. FTIR was used to investigate the molecular structure of some of the prepared materials for comparison reasons. Figure 3.11 shows an example of FTIR spectrum image.

The magnetic properties (hysteresis loops) were recorded at both room temperature and 10 °K using a Vibrating Sample Magnetometer (VSM) with a maximum magnetic field of 50kOe and 20 mg of powder used in each determination. The temperature dependence of the magnetisation curve under zero-field cooled conditions was also recorded. However, VSM is a scientific instrument that measures magnetic properties. It permits precision magnetic moment measurements to be made in a uniform magnetising field as a function of temperature and magnetising field. The sample is placed inside a uniform magnetic field to magnetise the sample. This equipment is shown in Figure 3.12. The sample is then physically vibrated sinusoidally. The induced voltage in the pickup coil is proportional to the sample's magnetic moment. The induced voltage is measured and the hysteresis loop of the material is obtained. Figure 3.13 shows an example of the resultant hysteresis loop.

Cobalt ferrite nanoparticles were pressed into disc samples using a uniaxial press (Moore & Son, Birmingham, UK) with a maximum possible load of 50 tonnes. This is shown in Figure 3.14. A pressure of 20 kg/cm^2 was applied for 20 s.

The disc samples after pressing, as an example, shown in Figure 3.15, were sintered using a continuous ramp rate, and a single dwell time conditions using a Chamber Furnace (Carbolite, UK). This furnace is shown in Figure 3.16.

Figure 3.7 DTA/TGA equipment

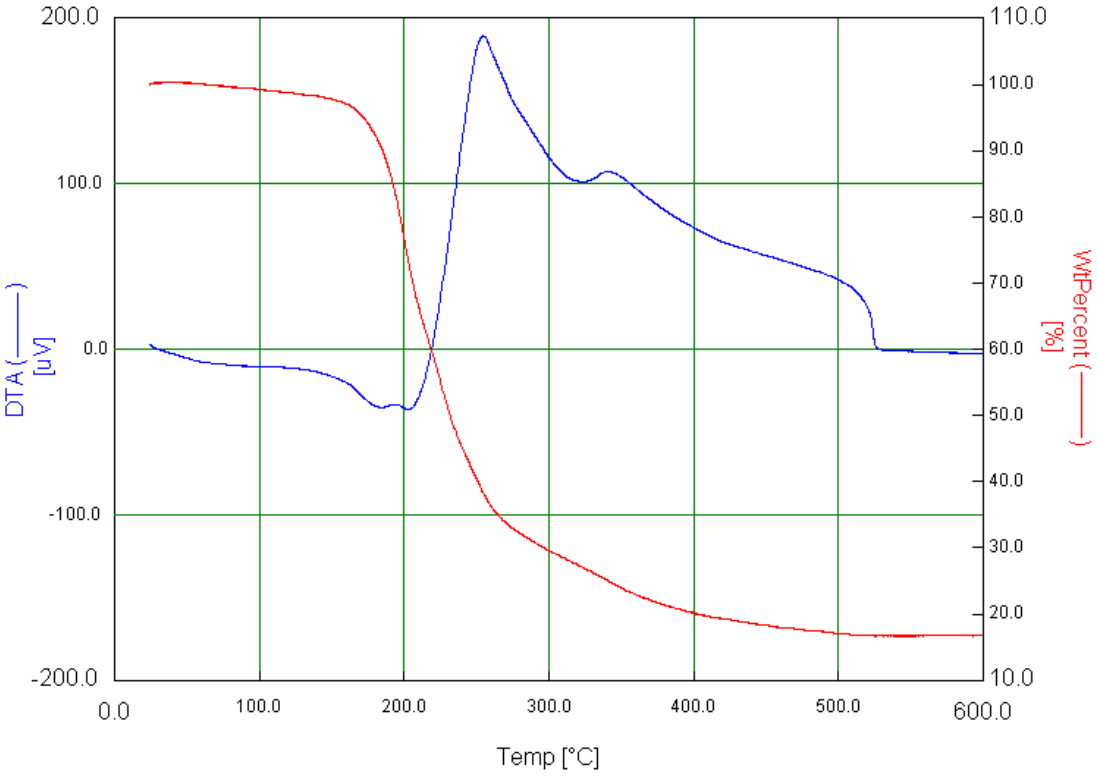

Figure 3.8 An example of a DTA/TGA graph

Figure 3.9 The SEM

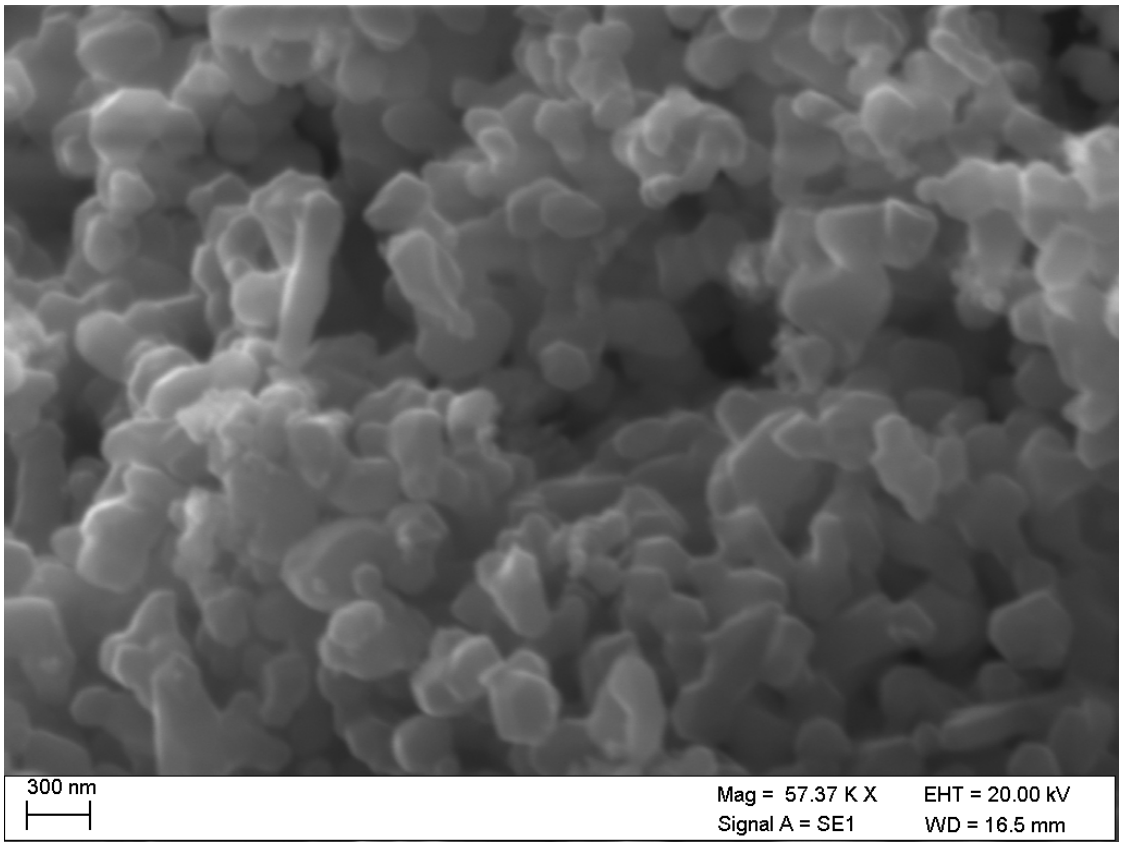

Figure 3.10 An example of SEM Image

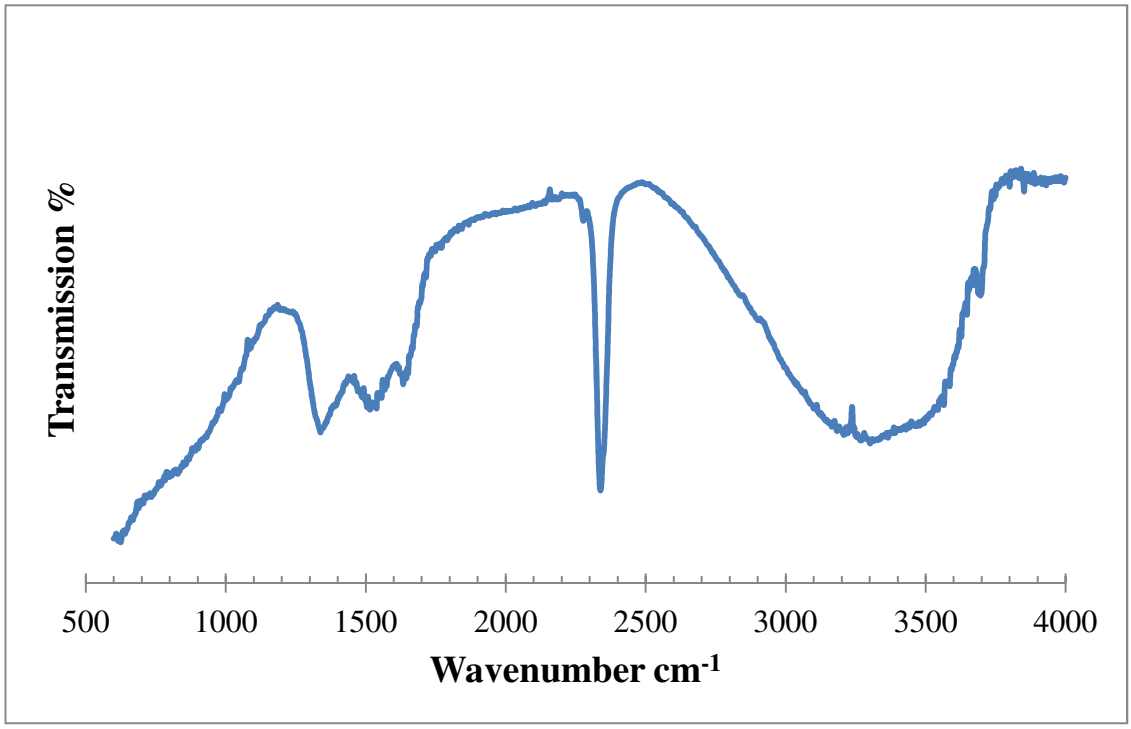

Figure 3.11 An example of FTIR spectrum

The density of sintered disc samples was measured employing an Archimedes Method Kit (Sartorius AG, Germany) as shown in Figure 3.17. The analysis measures the sample weight in air W (a) and in water, W (fl), and then the Buoyancy G is calculated, being the difference in weight [W (a) – W (fl)]. Density of water ρ (fl) was calculated according to temperature during experiment (SEE APPENDIX B). The density is then calculated employing the following equation:

$$\rho = \frac{W\,(a).\,[\rho\,(fl) - 0.0012\ g/cm^3]}{0.99983\ G} + 0.0012\ g/cm^3$$

Density measurements were also performed on sintered disc samples using an AccuPyc 1330 V1.02 helium gas Pycnometer (Micromeritics, USA). This equipment is shown in Figure 3.18. The analysis measures the sample volume, from which the density is calculated after the sample weight has been entered as an input into the computer programme. The relative density of each specimen was calculated as the quotient of bulk density to true density. The true density was experimentally determined on samples of powder using the same Pycnometer. The value of relative density is expressed as a percentage.

Figure 3.12 VSM equipment

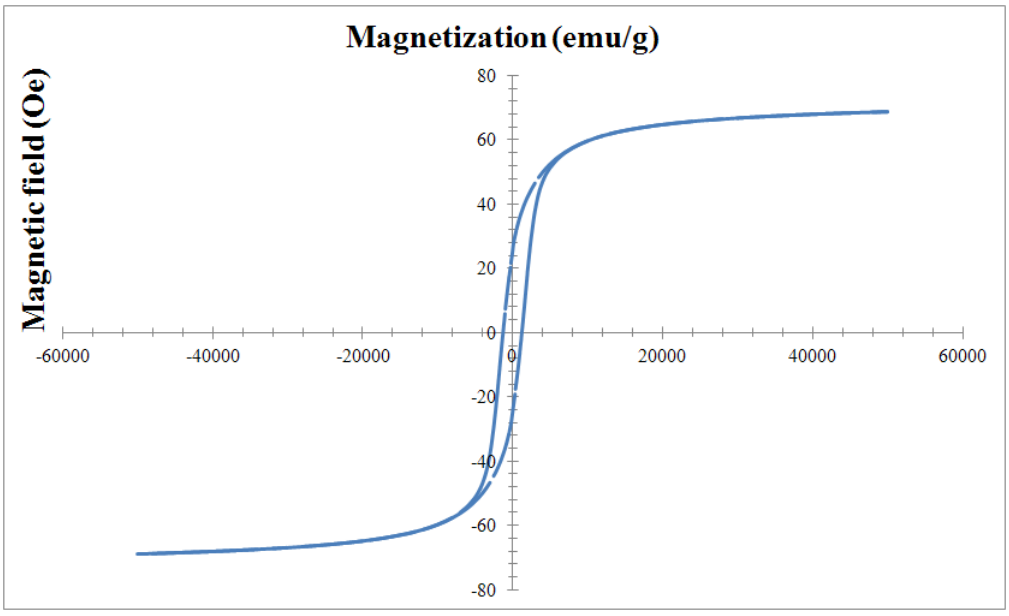

Figure 3.13 An example of a hysteresis loop obtained by VSM

Figure 3.14 The Uniaxial Press

Figure 3.15 Disc sample

Figure 3.16 The Chamber Furnace

Figure 3.17 Archimedes Method Kit

As the Archimedes Method Kit was used to measure the density of sintered disc samples, the measurements were believed to be a corrected form of values calculated employing the geometrical method as water could perfectly surround the sintered disc samples. It gave a good indication about the accuracy of the calculated geometrical densities.

Figure 3.18 The Pycnometer

3.4 Summary

The different items of equipment used to perform the characterisation of the materials used in the investigation have been described. Equipment used to carry out the various process operations which have transformed the starting materials into new forms, such as mixing, drying, pressing and heating have also been described.

After the different characterisations and processes had been performed, the results have been presented in the following four chapters which are followed by a chapter with conclusions and suggestions for future work. Each chapter includes a discussion section which focuses on the interim findings.

Chapter 4

The synthesis and characterisation of cobalt ferrite nanoparticles

4 The synthesis and characterisation of cobalt ferrite nanoparticles

4.1 Introduction

To prepare cobalt ferrite (single-domain) nanoparticles with a polydisperse distribution, there is firstly a need to understand the sol–gel technique. There is a necessity to acquire a fundamental understanding about the influence of the various chemical parameters on the structure and morphology of the final materials. Therefore, the aim of this chapter is to address this gap in understanding by concentrating in particular on the nature of the hydrolysis reaction and also on the effects of both the crosslinker and the chelating agent. Conclusions regarding the influence of the composition of the starting solution and of the subsequent heat treatment are drawn with reference to macroscopic observations of the materials and in conjunction with the respective XRD patterns.

4.2 Experimental

4.2.1 Material development

The sol–gel synthesis was based on the formation of a stable and homogenous sol obtained from a mixture of Cobalt (II) nitrate hexahydrate, ($Co(NO_3)_2$. $6H_2O$, ≥99%, Fluka) and Iron (III) nitrate nonahydrate, ($Fe(NO_3)_3$. $9H_2O$, ≥98%, Sigma-Aldrich). The precursors were used as received without any further refinement. 0.1M Sodium

hydroxide solution and de-ionised water were used as a catalyst and a reactant respectively. Di (ethylene glycol) diacrylate (DEGDA, Sigma-Aldrich) and citric acid (CA, Sigma-Aldrich) were employed as the crosslinker and the chelating agent respectively. The role of the crosslinker was to bring closer together the different inorganic particles and to improve the homogeneity of the solution. The chelating agent on the other hand reacts with both precursors by blocking their reactive functions achieving a remarkably homogeneous mixture.

The investigation of the effects of the crosslinker and the chelating agent was carried out to provide a good understanding about their influence on the structure and morphology. In all studies, the molar ratio $Co(NO_3)_2.\ 6H_2O$:$Fe(NO_3)_3.\ 9H_2O$ was kept constant at 1:2 and the hydrolysis was brought to 100% completion.

Two main procedures as shown in Figure 4.1 (a) and (b) were employed in this study. In the first procedure, Figure 4.1 (a), after the $Co(NO_3)_2$ and $Fe(NO_3)_3$ had been separately dispersed in a solvent and stirred for an hour both solutions were mixed together at that stage, followed by the addition of the reactant and the catalyst. The mixture was then left stirring for 24 hours. Later when appropriate, the crosslinker was added. And then the sol was stirred for a further 15 hours. In the second procedure, Figure 4.1(b), after the $Co(NO_3)_2$ and $Fe(NO_3)_3$ had been separately dispersed in a solvent and stirred using magnetic stirrers for an hour, the chelating agent was added and the two mixtures were stirred for two more hours. Both solutions were then mixed together and stirring was continued for 24 more hours. Stirring allowed the hydrolysis and condensation reactions to take place. All sols obtained by these procedures were stable and homogeneous showing the success of the sol–gel synthesis.

A beaker containing the sol was placed in a drying oven set at 100°C, and left there for 12 hours. The first thing which happened to the sol in the drying oven was that the liquid was gradually removed by evaporation. Without any stirring, some solid gradually formed on the walls of the beaker as the level of the surface of the liquid went down. As the sol gradually became more and more concentrated, the sol changed into a gel. Then as the gel lost more and more liquid by evaporation the gel became dry. It would be only at this stage that its temperature would have approach the 100°C. When the beaker was removed from the drying oven, the solid from the bottom and side walls of the beaker have been scraped off, before using a mortar and pestle to break up the

solid. The amorphous powders were then annealed in a Horizontal Tube Furnace (Carbolite Ltd., Sheffield, UK) between 600 and 1000 °C. The samples were ground using a mortar and pestle once after drying, and once more after the heat treatment. Details of all the procedures are listed in Table 4-1 with related synthesis parameters and conditions.

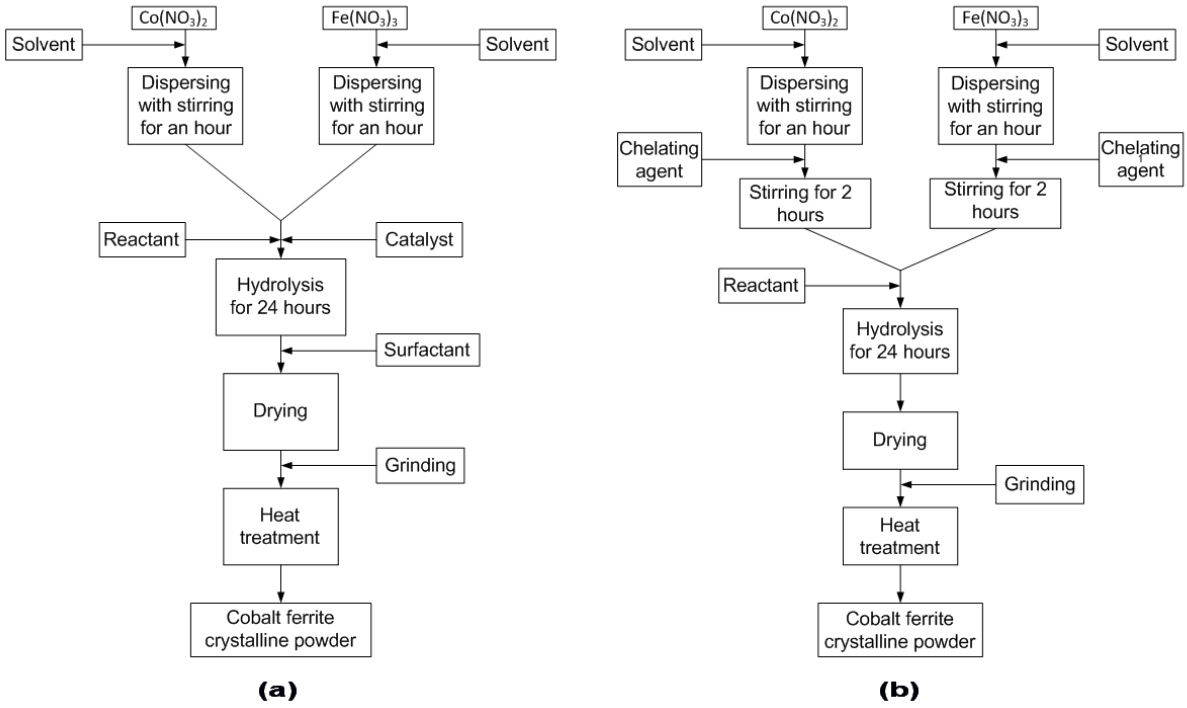

Figure 4.1 Materials preparation

Samples (1-9) were prepared employing the first procedure (a), and samples (10-14) were prepared employing the second procedure (b). 0.1M Nitric Acid solution was used as a catalyst for samples 3 and 4 to investigate a possible different effect when changing the catalyst from a base to an acid in contrast with samples 5 and 6 respectively.

4.3 Results

4.3.1 XRD patterns

According to the literature [6, 74], the cobalt ferrite pattern exhibits eight peaks. These peaks are located between 2θ°=15 and 2θ°=70 as follows: 18.289, 30.085, 35.438, 37.057, 43.059, 53.446, 56.975, 62.587. The respective intensities of

these peaks expressed with respect to the most intense peak located at 2θ°=35.438 are as follows: 10%, 30%, 100%, 8%, 20%, 10%, 30%, 40%, where the related Miller indices are: (111), (220), (311), (222), (400), (422), (511), (440), respectively. A validation of the equipment/results was done (SEE APPENDIX C). EDX analysis done on samples showed that the prepared samples contained elements such as Co, Fe, and O. There were no other elements detected (SEE APPENDIX D).

Table 4-1 Samples with their initial parameters and conditions

Sample	Solvent	Molar ratio (%) Crosslinker/Metal ions	Molar ratio (%) Reactant/Metal ions	Molar ratio (%) Chelating agent/Metal ions	Heat treatment temperature in degree Celsius (for 10 hours)
1	2-Propanol	-	100	-	600
2	2-Propanol	50	100	-	600
3	de-ionised water	-	-	-	600
4	de-ionised water	50	-	-	600
5	de-ionised water	-	-	-	600
6	de-ionised water	50	-	-	600
7	2-Propanol	300	100	-	600
8	2-Propanol	300	100	-	800
9	2-Propanol	300	100	-	1000
10	2-Propanol	-	100	100	600
11	2-Propanol	-	100	100	600
12	de-ionised water	-	-	100	600
13	de-ionised water	-	-	100	1000
14	de-ionised water	-	-	200	600

The XRD patterns of samples 1 to 6, as shown in Figure 4.2, show all peaks related to the $CoFe_2O_4$ phase proving the attainment of the cobalt ferrite structure. However, additional peaks were observed in these XRD patterns demonstrating the presence of other phases beside the cobalt ferrite structure. These have been attributed to the following impurities, hematite (Fe_2O_3), iron oxide (Fe_3O_4) in addition to the cobalt oxides (Co_3O_4) and (CoO) with (JCPDS-ICDD) file numbers of (89-2810), (26-1136), (42-1467) and (71-1178) respectively as identified using EVA software programme. In other words, there is no doubt that the cobalt ferrite structure is attained

as XRD patterns show. However, the formation of iron oxides in these samples indicates the formation of cobalt oxides in the same samples because the stoichiometry was unaltered. This is because if, for instance, iron oxide formed and cobalt oxide did not form, that situation could only occur if there were a change in the initial stoichiometry. The presence of the oxides indicates that the reaction between the constituents was incomplete. The results vary; however samples 2, 4, and 6, which were made when the crosslinker was added, contain about 20% less impurity than samples made without the crosslinker.

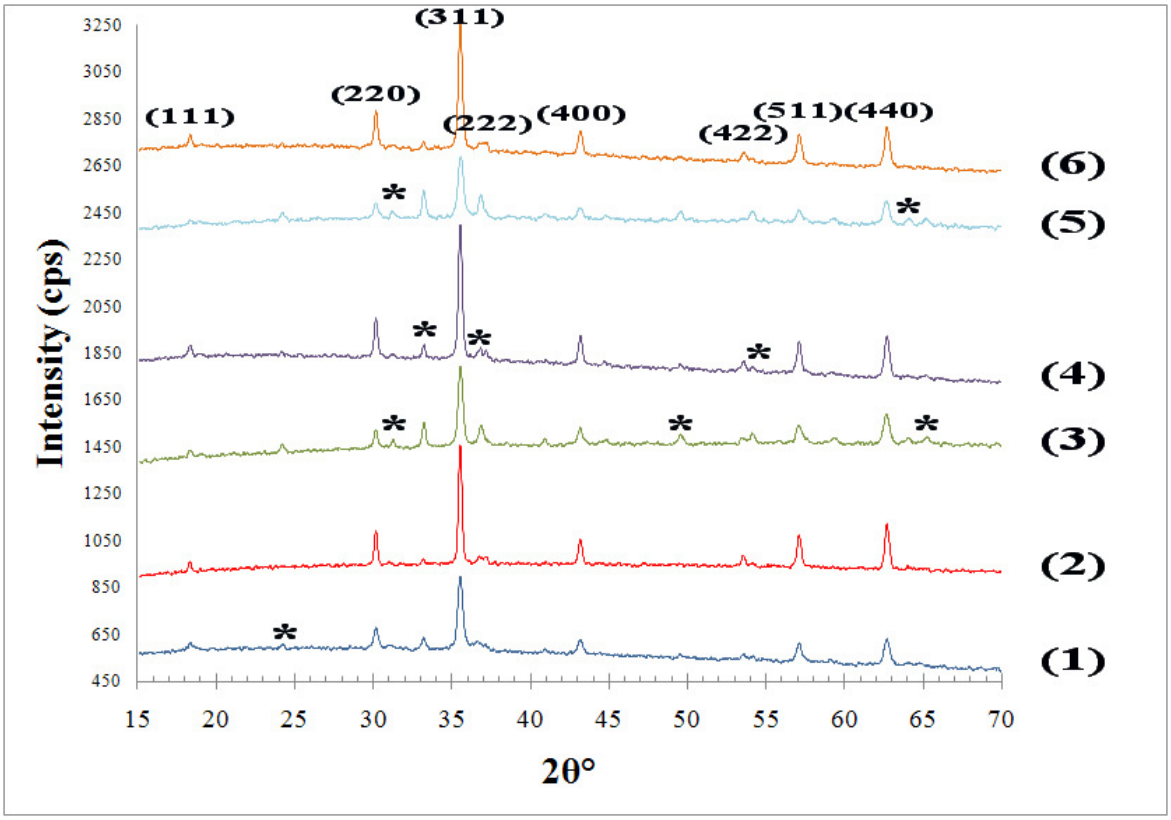

Figure 4.2 XRD patterns of samples (1-6)

XRD patterns of samples 7 to 9, which were prepared with 3 moles of the crosslinker for 1 mole of mineral ions (Co+Fe), are shown in Figure 4.3. These patterns are very similar to those of samples 2, 4, and 6, indicating the negligible effect on the resultant level of impurity structure of increasing the amount of crosslinker added. In addition, heat treatment at higher temperatures (800 and 1000 °C) for 10 hours did not significantly contribute to any reduction in the amount of impurities, even though these impurities seem to be due to incomplete reactions.

XRD patterns of samples 10 to 13 prepared using citric acid as a chelating agent with molar ratios of 1:1 for the metal ions to citric acid ratio (stoichiometric molar ratios) are shown in Figure 4.4. A further step of centrifugation at 4000 rpm for 20 minutes was applied to sample 11 in order to remove the supernatant, and to increase the rate of reactions promoting the gelling process in the heavier material at the bottom of the centrifuge tubes.

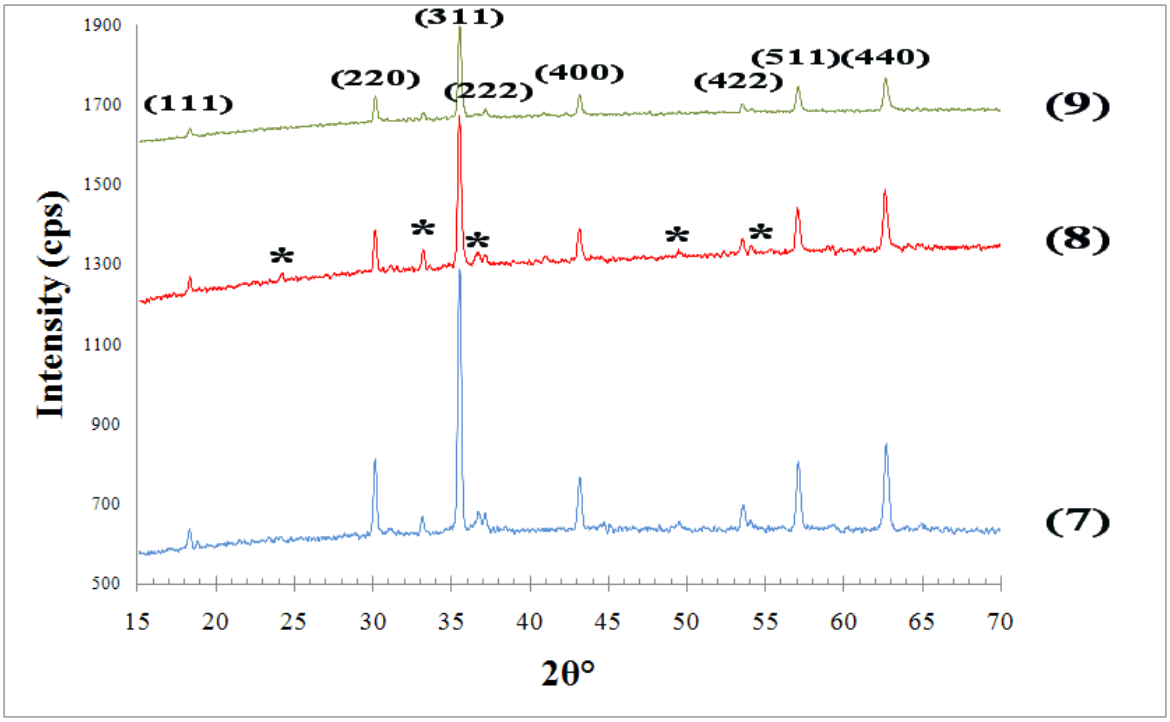

Figure 4.3 XRD patterns of samples (7-9)

A quantitative analysis reveals that sample 10 and 12 contain approximately 1% of impurities whereas sample 11 contains over 75% of impurities demonstrating the strong modification of the initial stoichiometry due to centrifugation. On the other hand, sample 13 is composed of 100% pure $CoFe_2O_4$ indicating that the increase in the annealing temperature caused the disappearance of impurity phases in this particular formulation.

The XRD pattern of sample 14, which was prepared employing a more thorough chelation of the mineral ions, is shown in Figure 4.5. This was to investigate the effect of completely isolating the cations from further reactions during the sol development process. The effect could only be determined by making observations on the powder after it had been produced. However, it can be unequivocally demonstrated that the

cobalt ferrite structure was obtained as a single phase, which exactly matches the JCPDS-ICDD file number 22-1086. Heat treatment at 600 °C for 10 hours was enough to obtain the pure cobalt ferrite structure with this composition, which leads to the conclusion that the chelating agent had an important effect in reducing the temperature needed for the heat treatment to bring about the cobalt ferrite structure.

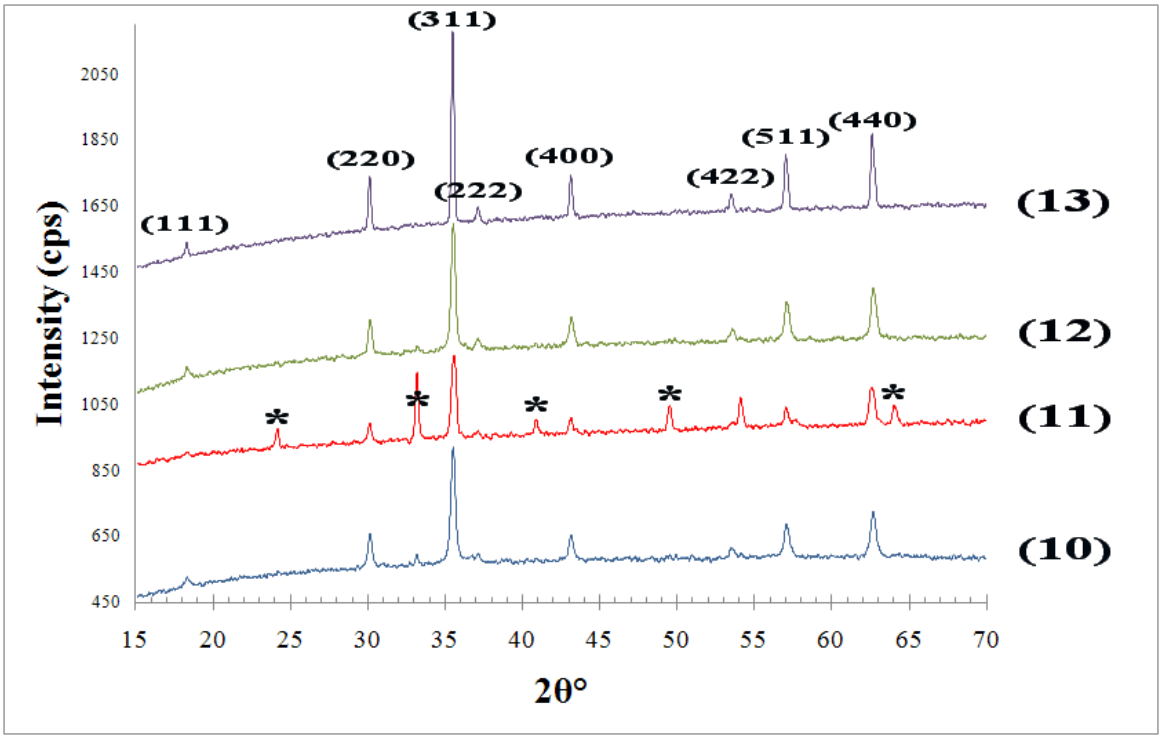

Figure 4.4 XRD patterns of samples (10-13)

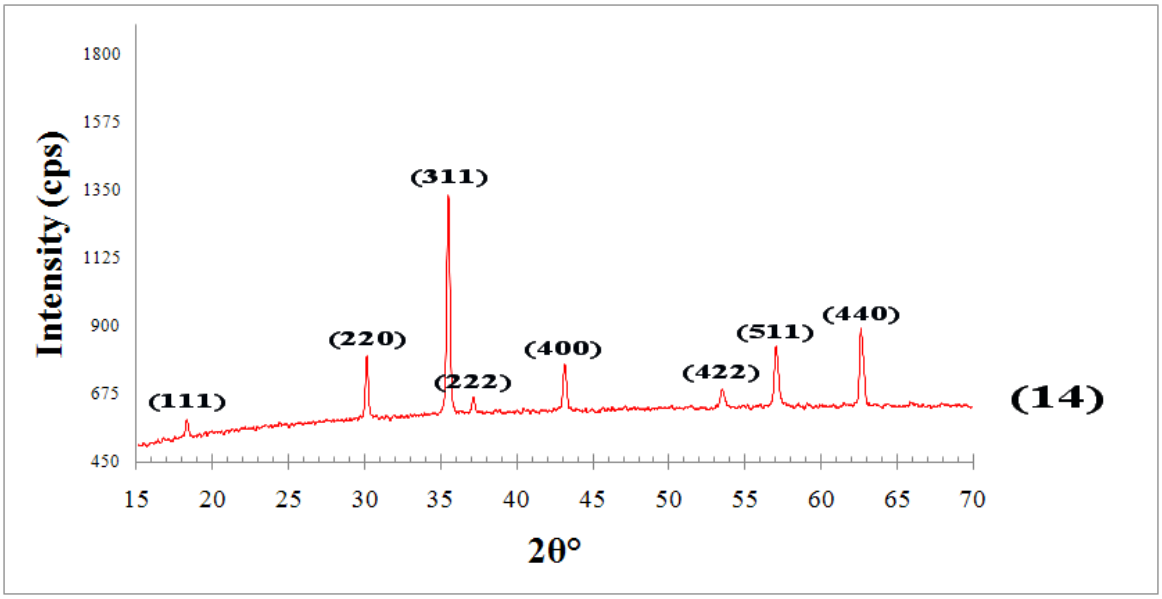

Figure 4.5 XRD pattern of sample (14)

4.3.2 DTA/TGA

DTA/TGA curves for sample 9 are shown in Figure 4.6. Over the temperature range 25-600 °C, the DTA curve exhibits only one single exothermic peak at 260 °C which signifies both the decomposition and the oxidation of the crosslinker, or its decomposition products. It is a fact that the crosslinker burns when heated releasing carbon dioxide.

DTA/TGA curves for sample 14 are shown in Figure 4.7. When heated over 150 °C, citric acid decomposes with the loss of water and producing some carbon dioxide. However, the DTA curve exhibits two exothermic peaks, one at 150 °C which refers to the loss of the water as the citric acid begins to decompose, and the other at 260 °C which refers to the oxidation of the remaining carbon content of the intermediate compounds of decomposition formed from citric acid, by oxygen in the air and forming more carbon dioxide, and releasing heat.

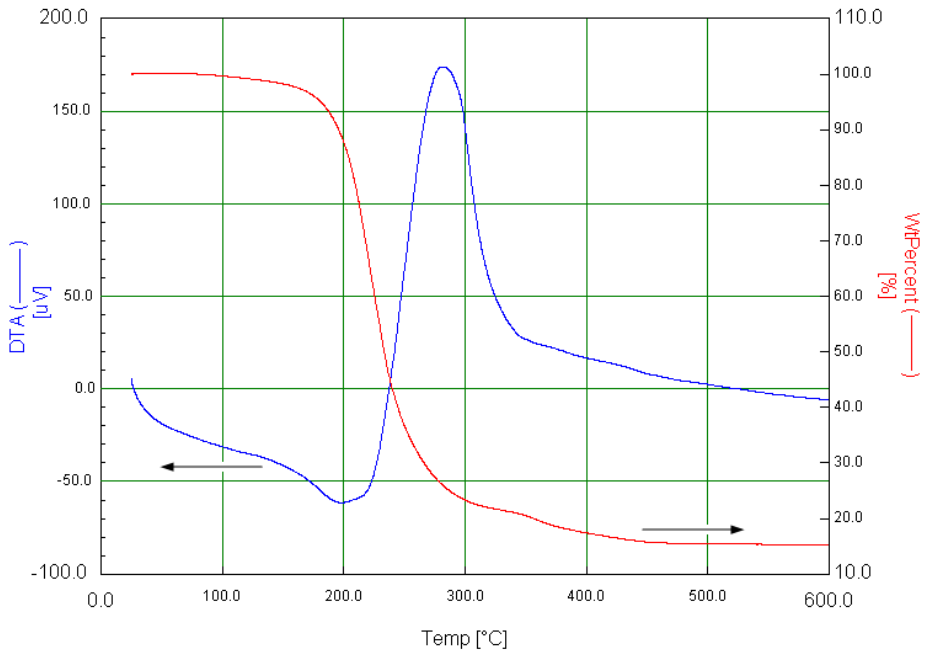

Figure 4.6 DTA/TGA curves of sample (9)

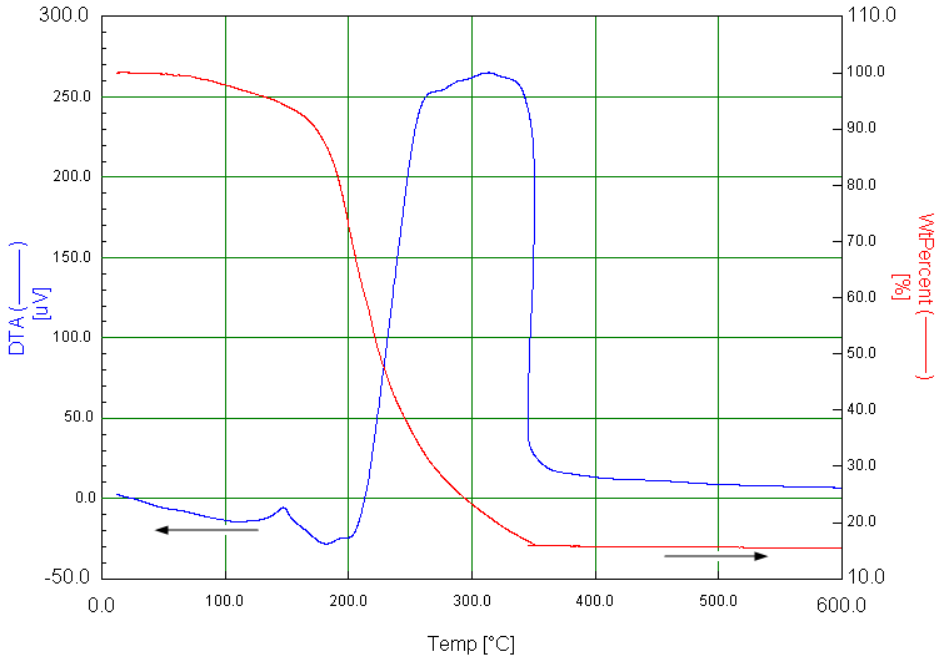

Figure 4.7 DTA/TGA curves of sample (14)

4.3.3 SEM/FE-SEM images

SEM images of samples synthesised with the crosslinker (2, 4, 6) and without the crosslinker (1, 3, 5) are shown in Figure 4.8. Samples prepared with the crosslinker exhibit a polydisperse size distribution with the particle size ranging from 90 nm to 200 nm, while samples synthesised without the crosslinker show a monodisperse size distribution with the particle size about 90 nm; furthermore, some particles were agglomerated and formed large clusters. No difference in either the structure or the particle size was observed when using the different catalysts in the corresponding procedures producing samples, 3 and 5, or 4 and 6 respectively.

SEM images of samples 7 to 9 are shown in Figure 4.9. The images indicate that sample 7 has a wide range of particle sizes (from 50 nm to 350 nm). Moreover, the particles are larger in size and have a wider size range when the temperature of the heat treatment is increased as shown for samples 8 and 9. An SEM image of sample 10 is shown in Figure 4.10. It shows a nano polydisperse distribution of particles with a range from 80 nm to 200 nm. An FE-SEM picture of sample 14 is shown in Figure 4.11. It

indicates the effect of increasing the percentage of citric acid which results in a wider range of particle sizes (from 20 nm to 250 nm).

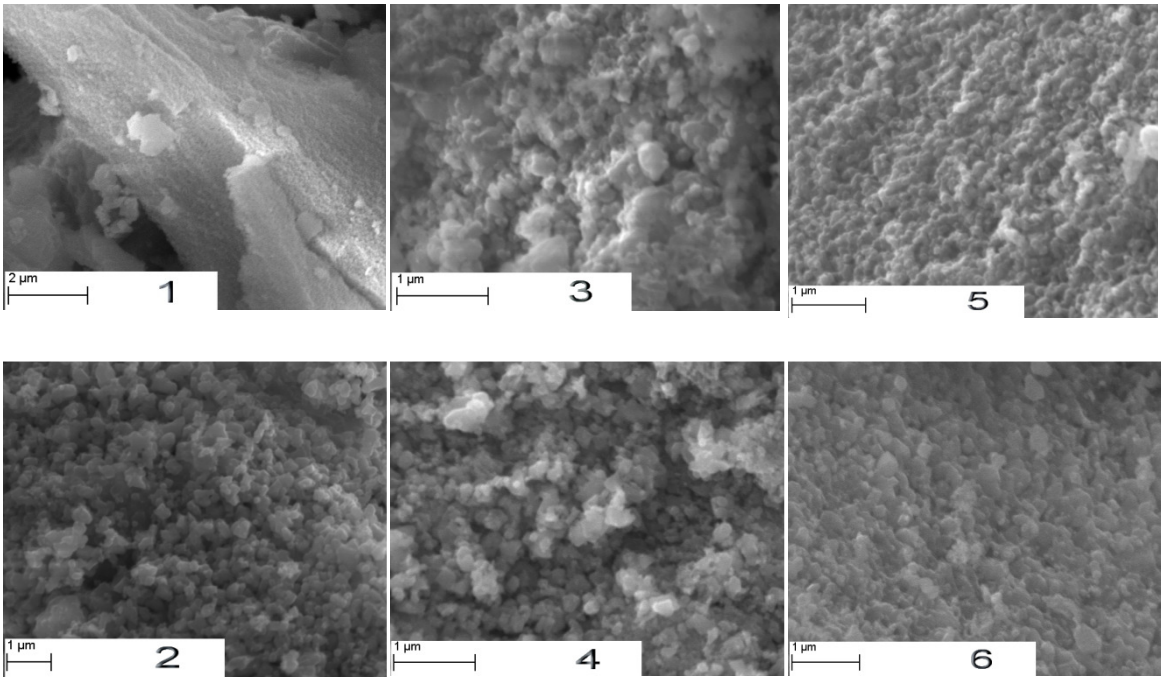

Figure 4.8 SEM images of samples (1-6)

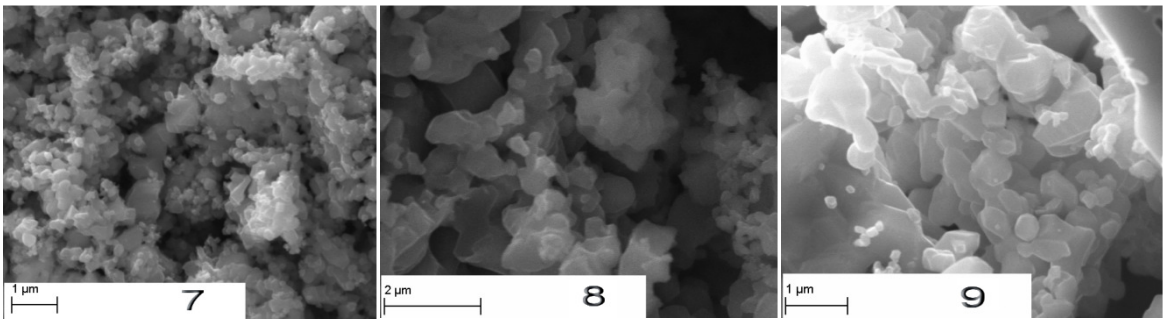

Figure 4.9 SEM images of samples (7-9)

4.4 Discussion

4.4.1 The effect of the crosslinker

A comparison of samples prepared with, and without, the crosslinker allows two main conclusions to be drawn. Firstly, when employing the same heat treatment conditions, the crosslinker causes a decrease in the amount of the impurities, but only by 20%. Increasing the ratio of the amount of crosslinker with respect to the inorganic

metal ions part beyond a certain point, for instance to 3:1, did not help in obtaining a purer cobalt ferrite product.

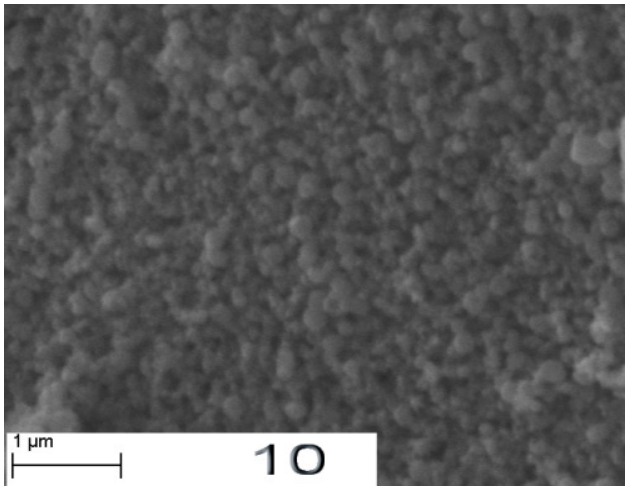

Figure 4.10 SEM image of sample (10)

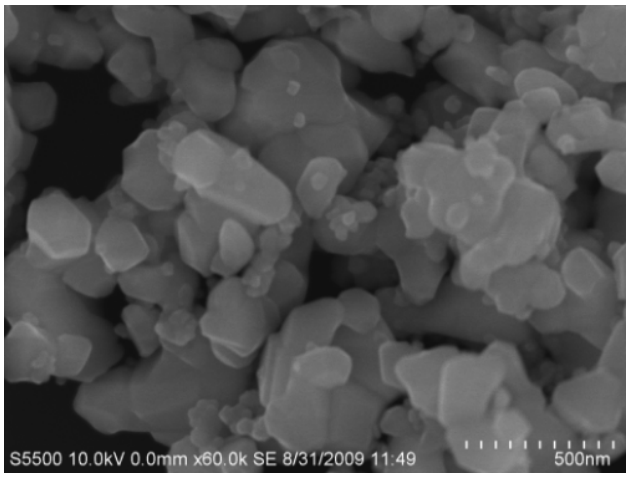

Figure 4.11 FE-SEM image of sample (14)

A calculation using the EVA software programme indicates that impurities were present at a level of 3% and these were identified above as a mixture of other oxides. These results show that along with the formation of cobalt ferrite, the crosslinker also favours the auto-condensation of iron and cobalt colloids to form Fe_2O_3 and CoO. The crosslinker allows the different metal ions, firstly to react with itself, and then subsequently during the heat treatment stage to approach other metal ions and eventually form an oxide bridge, As illustrated in Figure 4.12, the cobalt ferrite phase is produced as a result of reaction (b), whereas impurities, that is the other oxides, are the results of reactions (a) and (c). While (b) might be favourable, (a) and (c) can also

occur. The impurities probably occur because of the peculiar property of this crosslinker that allows all three different reactions to take place without there being a sufficiently selective mechanism, permitting only reaction (b). Therefore, using different ratios of crosslinker did not result in any improvement in the purity of the end product.

Even when employing heat treatment at higher temperatures (up to 1000 °C), a similar result was obtained. This indicates that the thermal energy was not sufficient to achieve a significant mobility for the cations within the oxides to change positions and so achieve the formation of cobalt ferrite.

Secondly, from a morphological point of view, it is observed that increasing the amount of the crosslinker increases the average particle size range from 110 nm to 300 nm. This change occurred when using the molar large ratios of 50% and 300%, expressing the amount of the crosslinker with regard to the amount of the metal ions respectively. In addition, it was found that increasing the heat treatment temperature results in an increase in the particle size also.

The reason for the choice of 300% is as follows: procedures involving molar ratios of 50% of DEGDA were carried out in order to crosslink a maximum of 2 metallic entities as shown in Figure 4.12. Procedures involving the 300% were investigated to ensure the full linking of the inorganic constituents (with every valency bond satisfied plus a slight surplus) with the purpose of exploring the effect of this crosslinker excess on the properties of the final materials. This results in a structure containing all possible links, which can be represented in the liquid phase as a hybrid polymer-like material, as shown in Figure 4.13.

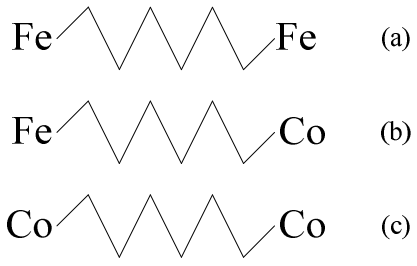

Figure 4.12 The crosslinker probable reactions, (a) and (c) are unfavourable, (b) is favourable

In both cases, when using either 50% or 300% of DEGDA, the subsequent heat treatment causes the decomposition and oxidation of the organic part, and in this way

the crosslinker acts as a catalyst of the inorganic condensation reaction. However, in the case when using 300% of DEGDA, the result is an even greater enlargement of both the particle size range and the sizes of the particles.

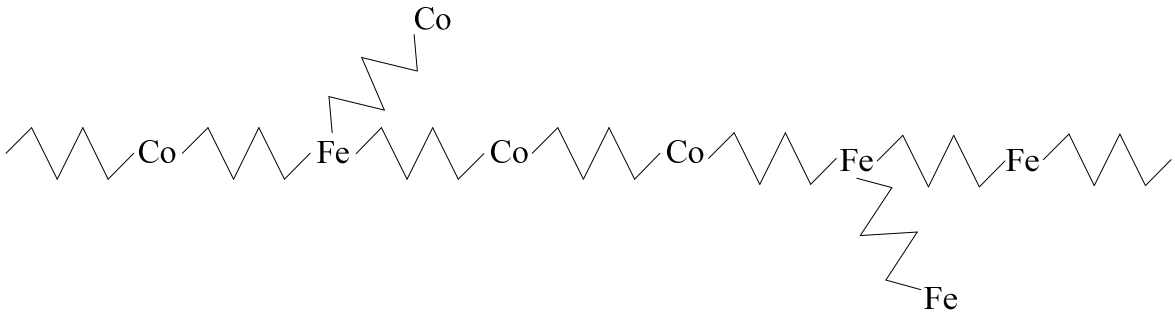

Figure 4.13 The hybrid structure of materials containing 300% crosslinker

On the other hand, samples without crosslinker did not have any cross-linking agent at work between the mineral ions. Very homogeneous sols were obtained by hydrolysis, but this homogeneity did not last for long. At the gelling stage phase separation took place. The solid particles in the gel agglomerated so much that sedimentation caused them to collect at the bottom of the beaker resulting in a mixture of oxides. The heat treatment was intended to form the ferrite lattice through an inter-diffusion process. However during this process, it was difficult for the cations to migrate between constituents to their thermodynamically ideal positions on A sites (tetrahedral) and B sites (octahedral) in the crystalline spinel lattice. The driving force for the inter-diffusion process was not sufficiently powerful. Sedimentation could cause the local stoichiometry to fail, and lead to higher levels of impurities, as demonstrated in Figure 4.2 in samples 3 and 5.

4.4.2 The effect of the chelating agent

Chelating agents are usually used in inorganic chemistry to prevent particle agglomeration by inhibiting condensation reactions in liquid phase synthesis [130]. In our study, citric acid was used to chelate both inorganic precursors to form either monodendate or bidendate metal complexes [131], as shown in Figure 4.14. In addition, it prevents both metal cations from undesired spontaneous condensation reactions.

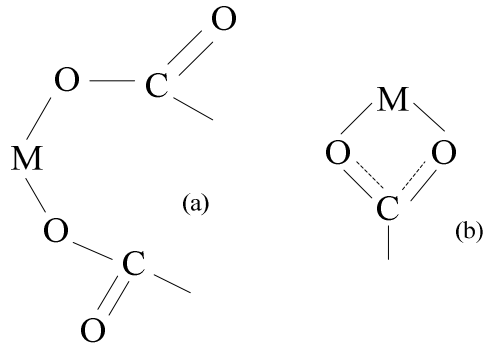

Figure 4.14 Metal complexes, (a) is monodendate, and (b) is bidendate

From a structural point of view, it has been clearly demonstrated that citric acid enables cobalt ferrite powders to be prepared under the same conditions as those when using the crosslinker. Indeed, comparisons of samples 2 with 10, and 4 with 12 show a decrease in the impurities' concentration from 3% to less than 1% respectively. Furthermore, the increase in the heat treatment temperature to 1000 °C, which was carried out when making sample 13, resulted in the single phase of cobalt ferrite being obtained, without impurities, whereas the same high temperature did not produce the same level of purity even when 300% of DEGDA was used when making sample 9. In fact, increasing the molar ratio of citric acid to 200% with respect to the metal ions seems to have been sufficient to ensure adequate chelation of the mineral ions forming both types of complex. It is suggested that one type of complex forms with the cobaltous ion and both types with the ferric ion as shown in Figure 4.15. If this is true, this, and other factors seem to combine to cause a more homogeneous mixture as explained below.

It would seem that the inter-diffusion process during the heat treatment was made more efficient due to the greater homogeneity, which had been achieved by that stage, and this enabled the development of the pure cobalt ferrite material in sample 14, when applying a heat treatment temperature of only 600 ºC. This can be explained by two factors: the first one is intimately associated with the molecular structure of the hybrid organic-inorganic complexes of both cobalt and iron ions, where, in contrast with the crosslinker, the chelating agent prevented any initial condensation or any cross-linking during the sol–gel synthesis. It causes the molecular structure of the sol to be composed of 2 hybrid complexes assigned by the initial stoichiometry as illustrated in Figure 4.15. Although the complexes have been formed, the two species of complex are

still free to diffuse throughout the solution. It is quite probable that the greater homogeneity is caused by an electrochemical effect, which would occur as follows: The initially strongly charged ferric ions would be only partially neutralised by the citric acid anions, and would continue to diffuse causing a high probability that they would become surrounded evenly by the initially less strongly charged cobaltous ions also only partially neutralised by the chelating agent. The process of diffusion would operate to ensure that the energy of the system would approach a minimum with no location having a higher or lower electrical charge, than any other location. Therefore, because of the initial stoichiometry, one ion of cobalt would inevitably enter an environment where it is close to two ions of iron. This does not happen when using the crosslinker, because once one of the reactions (a), (b) or (c), illustrated in Figure 4.12, has occurred, there is no mechanism for a rearrangement to take place to allow one ion of cobalt to be linked with two ions of iron. The second factor is that the oxidation of the organic part of the hybrid complex during the heat treatment caused a further chemical reaction at this molecular unit level with the formation of the cobalt ferrite structure, from a previously existing environment where the cobalt and iron ions were close to each other in the correct ratio. The critical difference between this and the crosslinker seems clearly to reside in the greater homogeneity at the molecular level which was not achieved to the same extent when using the crosslinker.

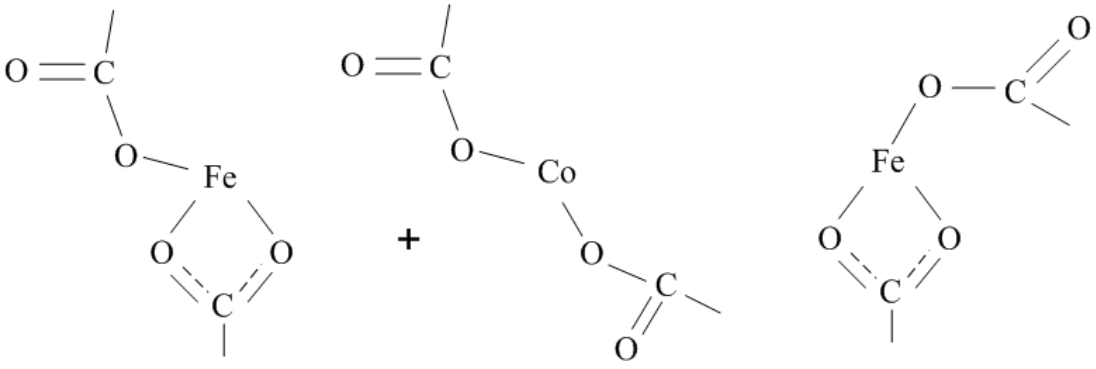

Figure 4.15 Organic-inorganic hybrids formed when using 200% chelating agent

In all cases during the heat treatment, nanoparticles tended to agglomerate and form larger particles and this resulted in polydisperse powders as illustrated, for instance in Figure 4.11. This particular image also seems to indicate that using larger quantities of the chelating agent while maintaining the same heat treatment temperature

tends to produce larger particles. This effect can be seen by comparing some of these particles with those in the powder illustrated in Figure 4.10 in which a smaller amount of citric acid was used. These particles in Figure 4.11 are larger than those in Figure 4.10. Larger quantities of the chelating agent are required because if this is not done a small quantity of impurities is formed, but it seems that when larger quantities are used it may be important to lower the heat treatment temperature because even at 600 ° C, there seems to be agglomeration forming larger particles. There is a window of opportunity for improvement because the DTA/TGA data indicates that citric acid decomposes at about 190°C. This suggests that a decrease in the temperature and the time of heat treatment would result in smaller particles, with a smaller size range, and there would still be the potential to achieve very low levels of impurities.

4.4.3 Calculating the crystal size of sample (14)

The crystal size of sample (14) was estimated using the Debye Scherrer equation [132] as follows:

$$\boldsymbol{D = \frac{0.9 \times \lambda}{\delta \times \cos(2\vartheta)}}$$

Where λ is the wavelength of the light used in the XRD equipment. It was 1.540598 Å (=0.1540598 nm). 2ϑ is the Bragg's angle, the angles of incidence and reflection producing the greatest intensity in the diffraction pattern. For cobalt ferrite, it is 35.348 degrees. δ is the width of the peak measured at half the maximum height of the peak (FWHM), which was measured using the XRD pattern of sample 14 at 2ϑ=35.438º. At that point, the height of the peak is 1390 and the background is 620. The intensity at which the FWHM is measured is, therefore [(1390-620)/2] +620 = 1005. This results in a value for δ of 0.216° (= 0.00377 radians). Cos (2ϑ) is Cos (35.348) =0.8147.

Substituting with respective values gives an average crystal size of 45 nm.

$$D = \frac{0.9 \times 0.1540598}{0.00377 \times 0.8147} = 45 \text{ nm as the crystal size}$$

An estimate of the sizes of these particles using the FE-SEM image in Figure 11 gave values in the range from 20 nm to 250 nm. This indicates some particles in sample 14 are composed of a number of crystals i.e. they are polycrystalline, and some particles consist of individual crystals. The reason behind this is attributed to the high heat

treatment temperature and the long dwelling time which facilitated the process of forming the larger particles at the expense of the smaller ones. The analysis of the XRD pattern of sample 14 by the EVA software programme provided with the instrument shows that the powder is composed of a single spinel phase of cobalt ferrite with lattice parameter (a) equal to 8.3919 Å.

4.5 Summary

Cobalt ferrite powders have been synthesised employing the sol–gel technique. A particular focus was given to the investigation of the fundamental role of the crosslinker and chelating agent on the structure and morphology of the materials being synthesised. The results clearly indicate that citric acid enables cobalt ferrite to be obtained with a higher purity than could be obtained using the crosslinker. This difference has been correlated with the different molecular unit structures formed when using each of the two organic molecules. The crosslinker allows the formation of three different structural units which produces a mixture of the oxides (cobalt oxide with iron oxide, iron oxide on its own, and cobalt oxide on its own). On the other hand, the chelating agent permits the formation of individual molecular units that are free to diffuse, so that the initial stoichiometry can be maintained. In addition, the crosslinker and chelating agent were found to have a crucial effect on the particle size and on the range of different sizes of particles, under the same conditions. These results can be considered as part of a preliminary study of the development of methods to prepare cobalt ferrite nano materials, and it is intended that they can be implemented in specific magnetic applications.

Chapter 5

The structural and magnetic analyses of nanoparticles

5 The structural and magnetic analyses of the nanoparticles

5.1 Introduction

In the previous chapter, it was suspected that the cobalt ferrite nanoparticles which had been synthesised had agglomerated and formed larger particles as a result of the heat treatment operation. This is because these nanoparticles were found to be in the size range between 20 and 250 nm. While some of these synthesised nanoparticles may be small enough to have only one magnetic domain, it is probable that others have many magnetic domains, because they are so large. Therefore, there is a need to investigate whether the thermal energy released in the heat treatment operation could be reduced because it might be responsible for the undesired growth of particle size during this operation.

In the phase of the study reported in this chapter, the sol–gel technique was followed in the preparation of cobalt ferrite amorphous powder following the same procedure which was selected as the best approach as described in the previous chapter.

It was assumed that there must be a correlation between the heat treatment operational parameters (the temperature and the time) and the structural properties (the crystallinity and the freedom from unwanted oxides) of the material being synthesised. Similarly, it was understood that some heat treatment is necessary to completely decompose the organic and nitrate contents present in the amorphous powder and finally

to form the spinel structure without these kinds of impurities also. It was therefore important when attempting to change these operational parameters of the heat treatment that this would not result in a material with poorer properties.

Having ensured that the heat treatment parameters could be changed without producing a material with poorer properties, it was then possible to produce batches of powders using milder conditions in the heat treatment operation. The particle size distributions of these new batches of nanoparticles were estimated and since the results showed promise, their magnetic properties were also determined. The significance of these results is discussed in detail.

5.2 Experimental procedure

5.2.1 Material development

The sol–gel synthesis was based on the formation of a stable and homogenous solution made by dissolving a mixture of Cobalt (II) nitrate hexahydrate ($Co(NO_3)_2.6H_2O$, ≥99%, Fluka) and Iron (III) nitrate nonahydrate ($Fe(NO_3)_3.9H_2O$, ≥98%, Sigma-Aldrich) in de-ionised water, which is a hydrolysis reaction. The solution was transformed into a sol and then a gel by evaporation of the water, and during this time condensation reactions took place. Details of the whole preparation process are sketched in Figure 5.1.

The precursors were used as received without any further purification. In order to maintain the homogeneity in both the sol and the gel during the condensation and other reactions, avoiding any precipitation or sedimentation of the products of these reactions, citric acid (CA, Sigma-Aldrich) was employed as a chelating agent. Both precursors were initially separately dispersed in de-ionised water for half an hour by stirring. Following this dispersion, the chelating agent was added and the mixture was left reacting under vigorous stirring for 2 hours. Both solutions were then mixed together and left stirring for 24 hours and after this the condensation reactions of both metal nitrates were allowed to take place. The quantity of each metal precursor was calculated so that the ratio of the two metals in the final material would be Co:Fe = 1:2 and the quantity of citric acid was estimated assuming that each ferric ion would require

two molecules of citric acid and each cobaltous ion would require two molecules of the chelating agent as well, so that the metal ions would be adequately chelated.

5.2.2 Methodology

It is understood that most of the oxidation reactions which occur during the heat treatment operation take place above a temperature of 200 °C. This follows as a result of the DTA/TGA curves for the amorphous powder which are shown in Figure 5.2. Therefore, in the initial investigation to determine whether the temperature used in the heat treatment operation could be reduced, the temperature range of 200-600 °C was selected for the initial trials and the 10 h dwelling time was maintained for each trial. The period of 10 h was selected because originally it had been found in the previous study that it had made it possible for the spinel structure to be formed.

The methodology of this initial study consisted in a series of trials. In each trial the temperature of the heat treatment was different. The selected temperature was decreased for each member of the series from an initial value of 600 °C for the first trial in intervals of about 50 °C to a temperature of 200°C, being the lowest temperature of interest, while the dwelling time was maintained at 10 hours. It was then planned that a second series of trials would be carried out in which this minimum temperature for the heat treatment would be maintained, while the dwelling time would be progressively decreased from an initial value of 10 hours in intervals of 2 hours, down to a final value of 2 hours.

Afterwards, the material produced in each trial was analysed by XRD, with the aim of identifying and then quantifying the impurities in the products. It was hoped that this work would identify a temperature for the heat treatment, below which there would be problems with impurities, and above which the risk of impurities developing would be insignificant. This temperature would be the minimum temperature at which the heat treatment could be operated in a process to produce pure cobalt ferrite with its spinel structure.

However, as the work progressed it became clear that with a temperature of only 200°C, the heat treatment could still result in producing the cobalt ferrite with the spinel structure with no other oxides. At this point, the investigation became focussed on the dwelling time of the heat treatment, and this was then studied. It could be safely

assumed that investigations studying different dwelling times (10, 8, 6, 4 and 2 hours) at temperatures which are much higher than the minimum temperature, e.g. 500 or 600 °C, would result in products with the spinel structure and without impurities. As the research interest is to determine the critical conditions, it was thought there would be no point in including these extra conditions in this study as they are not of great importance. These other trials would have had much less significance in this study, being examples which might have produced the same quality of product, but the conditions required to do so would be ruled out as being of no economic benefit, because similar results can be obtained at much less cost. If they had been included, there would have been about 40 samples instead of the 12 already mentioned. It is better to focus the interest on studying the morphology and magnetic properties in the much smaller number of samples of nanoparticles whose significance lies in the fact that they are much more likely to be produced on a larger scale. The list of samples investigated in this study and their conditions of preparation are indicated in Table 5-1.

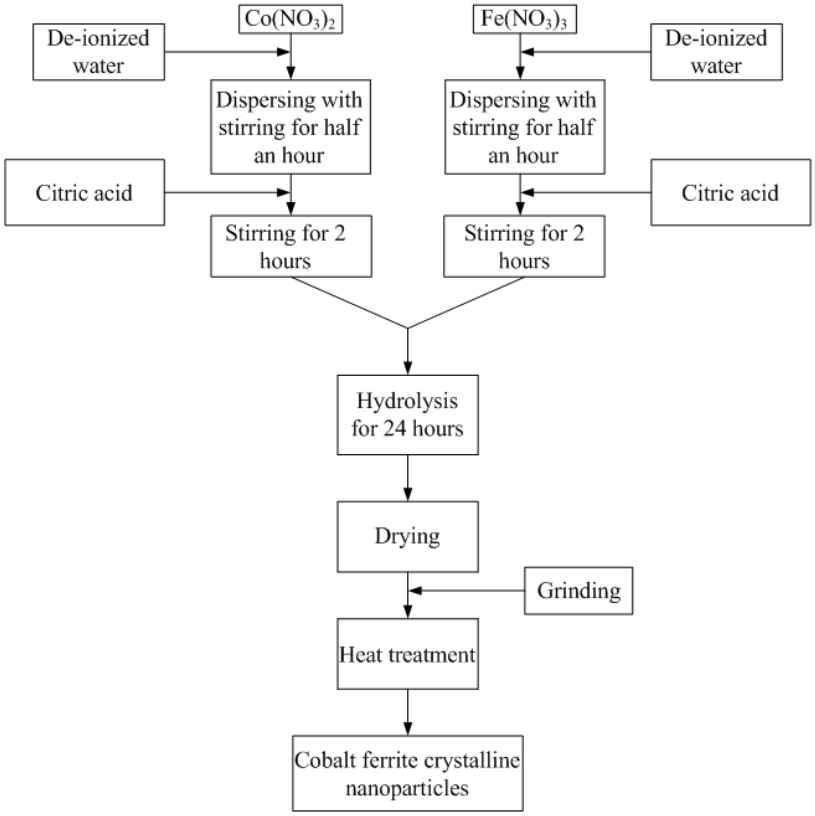

Figure 5.1 Materials preparation

5.3 Results and discussion

5.3.1 Structural and thermal analyses

The XRD patterns of the products prepared with the heat treatment operational parameters defined in Table 5-1are presented in Figure 5.3. One can observe that all the peaks related to cobalt ferrite spinel structure are identifiable in all the materials with no additional peaks and all patterns match with the JCPDS-ICDD file number of 22-1086.

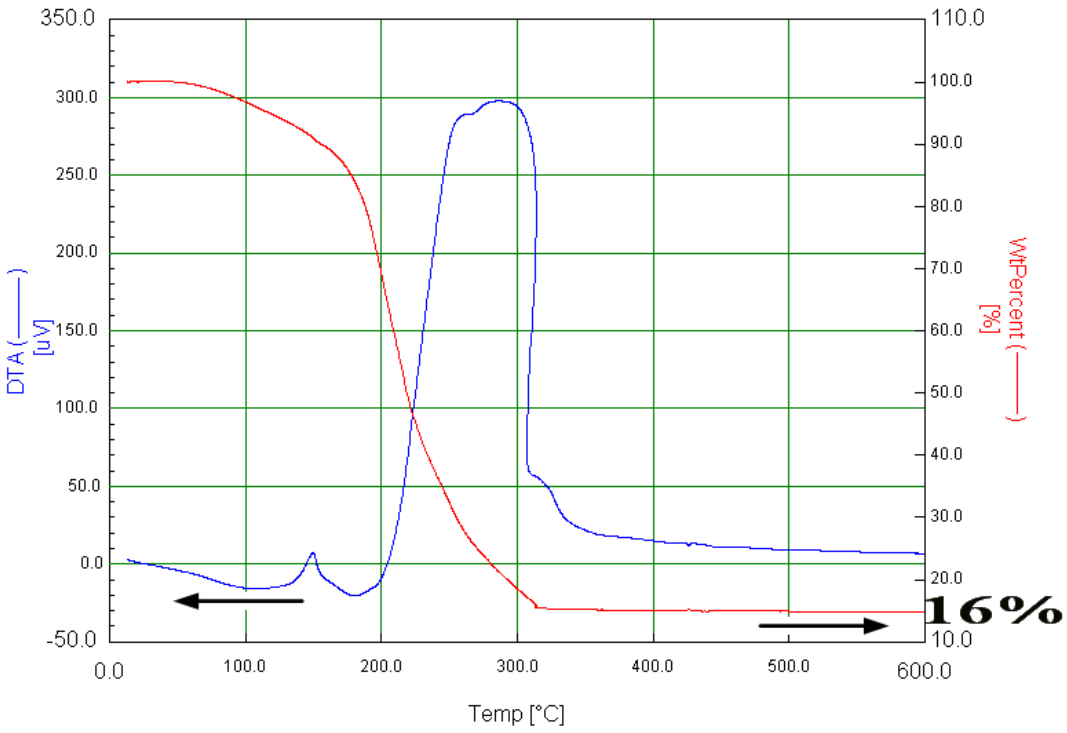

Figure 5.2 DTA/TGA curves of amorphous powder

Although each sample in the series was prepared at a different heat treatment temperature, in the range from 600 °C down to the minimum temperature of interest, i.e. 200 °C, in each case the only phase observable in the XRD patterns is that of the cobalt ferrite spinel phase as indicated by the XRD patterns of samples A, B, C, D, E, F, G, and H. At that stage, it was thought that there would be no point in operating the equipment with a dwell time of 10 h if reducing the time could also result in reducing the particle sizes. Therefore, in a further series of trials the 10 hour dwell time was reduced to 8, 6, 4, and then finally to 2 hours while the temperature was maintained at 200 °C. Again in each case the only phase observable in the XRD patterns is that of the

spinel structure as indicated by the XRD patterns of samples I, J, K, and L shown in Figure 5.3.

Table 5-1 The heat treatment conditions of prepared samples

Sample	Heat Treatment Temperature in degree Celsius	Dwelling Time (hours)
A	600	10
B	500	10
C	450	10
D	400	10
E	350	10
F	300	10
G	250	10
H	200	10
I	200	8
J	200	6
K	200	4
L	200	2

These results indicate the success of the particular form and arrangement of the sol–gel technique, described in chapter 4 in developing a material with the cobalt ferrite spinel structure. It can be assumed that with this particular choice of starting materials and procedures, the cobalt ferrite structure would have been obtained with a heat treatment temperature anywhere within the range between 200 and 600 °C. However, as XRD patterns can only be used to identify crystalline structures present in a material they do not give any information about the purity of the materials, if these materials also contain substances which are not crystalline, such as organic constituents. It was therefore decided to perform thermal analyses such as DTA/TGA to identify the purity of the prepared materials taking into account non-crystalline substances. These other techniques would identify the minimum temperature and time required to complete the decomposition of the nitrates and the decomposition or oxidation of organic moieties, initially present in the precursors and in the chelating agent or having been produced in reactions during the sol–gel processing.

To pursue this approach further, the dwelling times and temperatures of the heat treatment operation, which were designated above as A and L were selected for comparison, because they represent the two extremes of the parameters, being the

strongest 600 °C, for 10 h and the mildest 200 °C, for 2 h respectively. The heat treatment operations were then carried out, but in the DTA/TGA equipment using the same starting material, the amorphous powder produced by the sol–gel process, and using the equipment's programmable ramp rates and set temperatures to repeat, as closely as possible, the operation of the horizontal tube furnace, normally used for the heat treatment operation. According to the work reported in the previous chapter, the heat treatment conditions designated as A were carried out already, in both the horizontal tube furnace, and in the DTA/TGA equipment (sample 14 and Figure 4.7). The analyses suggest that the product, identified as cobalt ferrite with a spinel structure, at 350°C, became free of any organic or unstable inorganic impurities, because the solid became stable with no further oxidation or decomposition reactions to form gases about and above 350°C. These results can therefore be used as a reference for comparison with the heat treatment parameters designated as L.

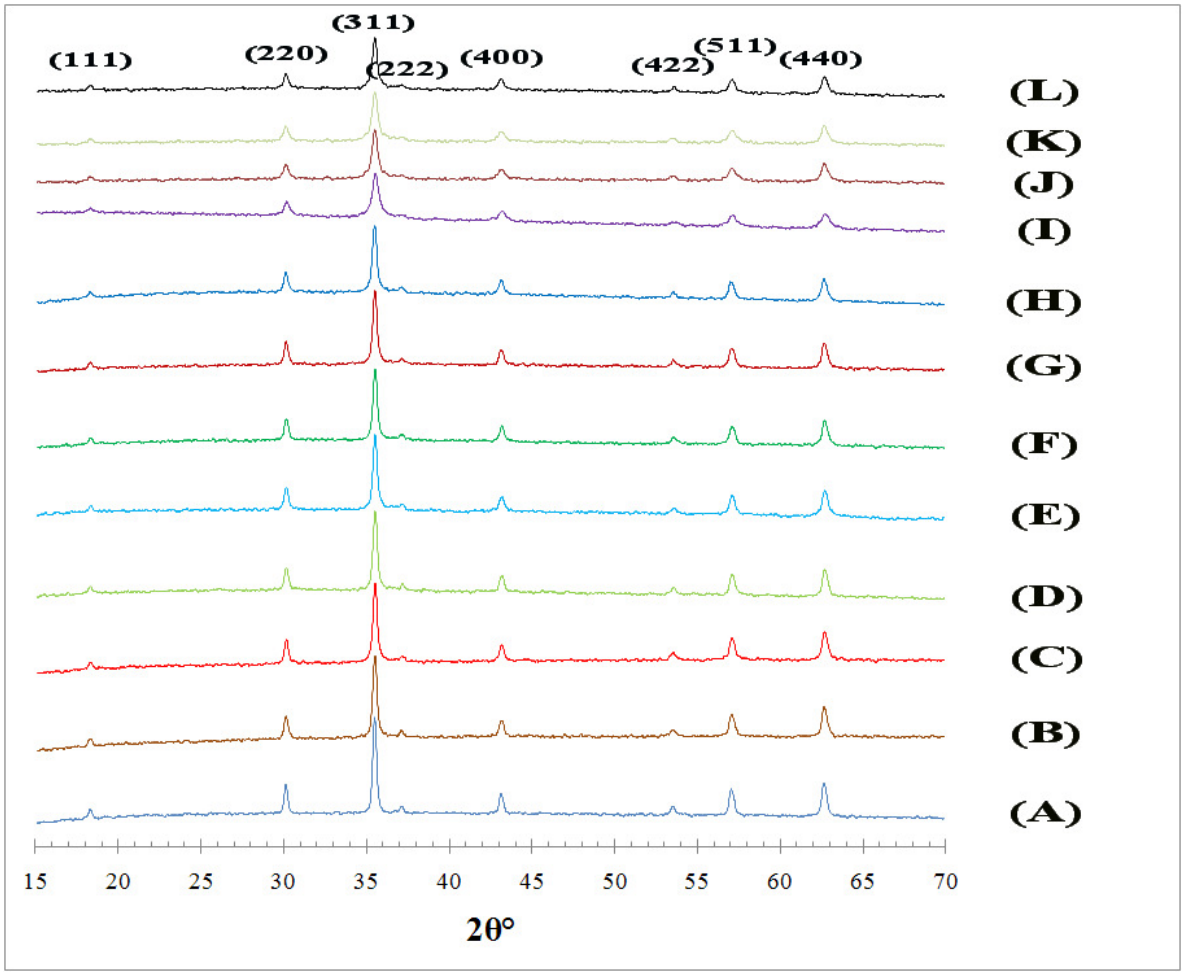

Figure 5.3 XRD patterns of samples (A-L)

The thermal analysis following the heat treatment conditions designated by A is shown in Figure 5.2. In the results one can observe that within the range of temperatures between room temperature and 600 °C, the DTA curve exhibits two exothermic peaks or bands centred at 150 °C and 300 °C. The band centred at 300 °C is actually spread out over a range of temperatures from 205 °C up to 345 °C. This band seems to result from the superimposition of several overlapping bands. In fact, it is well known that the oxidation of various, similar organic compounds take place in this domain of temperatures. In this case, it is very likely that the width of the band results from both the decomposition of the nitrate ions, which were originally linked to both the Co and the Fe ions and the oxidation and decomposition of the citric acid, which have become linked to both the Co and the Fe ions. Furthermore, the TGA curve shows that the initial weight of material reduces to 16% of its original value during the treatment. The additional components contribute 84% to the total weight of the amorphous powder.

The results of the DTA/TGA following the heat treatment conditions designated by L are shown in Figure 5.4. It has already been shown using different equipment that the heat treatment conditions of 200°C for 2 hours produces cobalt ferrite with the correct spinel structure with no other oxides. However, one can observe in the TGA curve that the initial weight of the starting material reduces to only 29% of its original value. This is 13% higher than the final value when compared with the corresponding result for the heat treatment procedure designated by A. This must be attributed to the incomplete oxidation and decomposition of the organic and nitrate components. This result indicated the need to investigate the effects of the different parameters in the heat treatment operation more thoroughly and to identify the optimum set points which would produce the cobalt ferrite free of all additional components.

To identify the optimum heat treatment conditions, there were initially two alternative strategies which could be adopted: either (1) gradually to increase the dwell time while maintaining the heat treatment temperature at 200 °C; or (2) gradually to increase the heat treatment temperature up towards 600 °C, keeping the dwell time constant at 2 hours. However, it was considered most likely that increasing the heat treatment temperature would generally have a greater effect on the particle size, than an increase in the dwell time, and a growth in particle size is most undesirable in this study.

Therefore, increasing the dwell time at a lower temperature was considered to be a better strategy than increasing the temperature with a short dwell time.

This investigation started, therefore with 200 °C as the heat treatment temperature, and the dwell time was gradually increased in a series of trials using the DTA/TGA equipment. However, even when the dwell time had been extended to 10 hours, the TGA curve showed that the initial weight of the starting material was reduced only to 24% of the original value. This indicates that there was insufficient thermal energy to oxidise or decompose the organic and nitrate components completely.

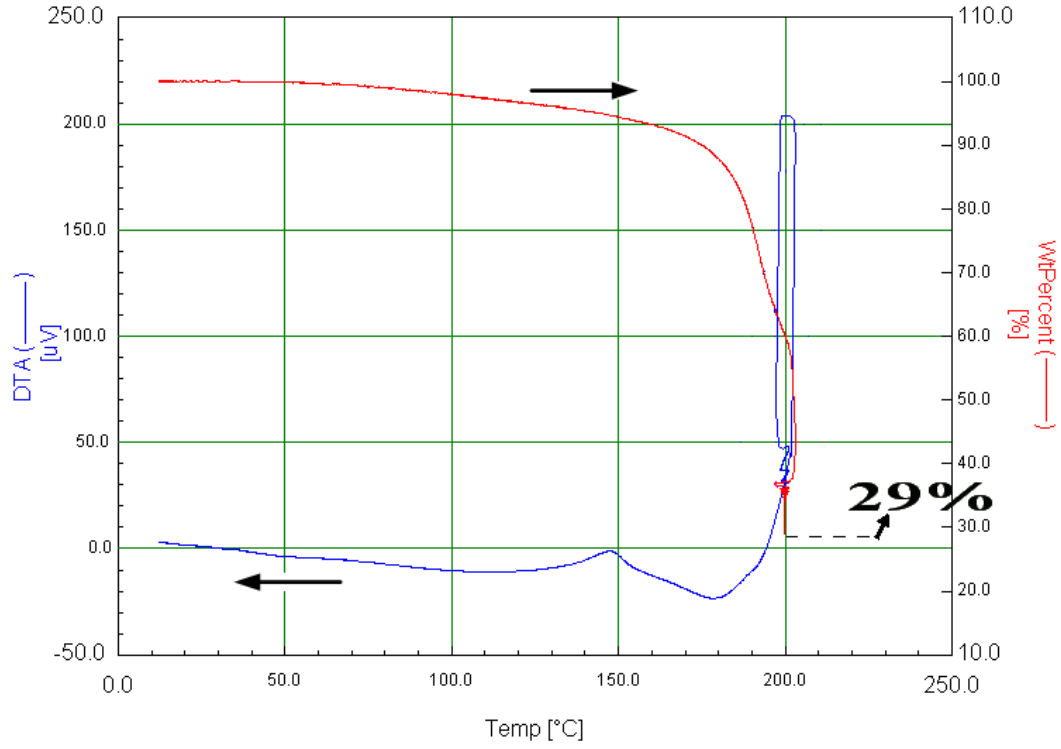

Figure 5.4 DTA/TGA curves of sample (L)

A temperature of 250 °C was then selected and the same approach was repeated by gradually increasing the dwell time. Eventually, it was found that with the parameters of 250 °C and 10 hours as the heat treatment temperature and time respectively, the desired result was achieved. The final point on the TGA curve at 250°C was 16%.These parameters had already been selected in earlier trials, and had been designated as G. They represent the lowest thermal conditions for the heat treatment which will ensure the complete elimination of all impurities. The heat

treatment operation with these settings would provide the smallest possible opportunity for the particle size to increase because the temperature would be kept to the minimum. In other words, the heat treatment conditions designated by G can be considered to be sufficient to oxidise the organic compounds in the samples, to eliminate all impurities and at the same time to provide the smallest opportunity for any undesired growth in particle size to take place. The DTA/TGA curves for these heat treatment settings designated by G are shown in Figure 5.5. The final percentage point weight of the TGA curve is found to be equal to the equivalent final percentage point weight of the TGA curve following the heat treatment parameters designated by A (16% of its initial weight). This demonstrates the complete elimination of all impurities and the attainment of cobalt ferrite as a single phase.

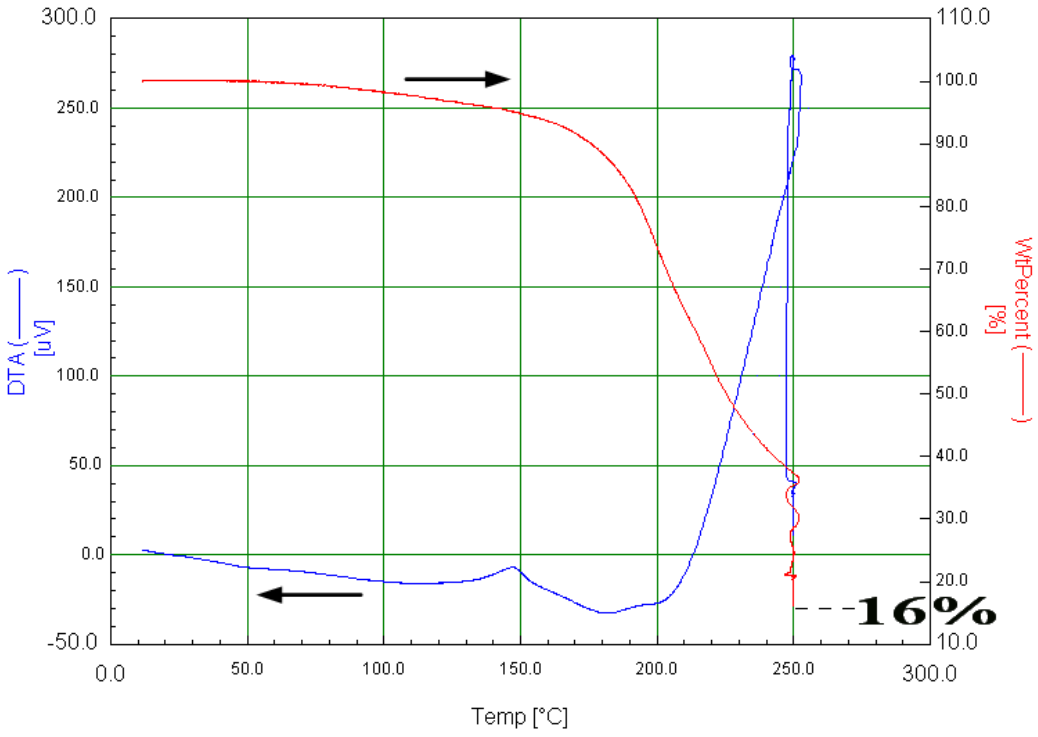

Figure 5.5 DTA/TGA curves of sample (G)

5.3.2 FTIR analysis

FTIR spectroscopic analyses were carried out on samples of the same amorphous powder, the product of the sol–gel processing described above, after they had been heat treated in the horizontal tube furnace. The parameters used in the heat

treatment operation were different for each sample, and these parameters were the same as those designated as A, G, H and L in Figure 5.3.

. The results are shown in Figure 5.6. One can observe that the spectra of samples A and G are identical demonstrating the presence of the same chemical bonds and molecular structure in both samples. These spectra are clearly different from the spectra of samples H and L, which are identical on their own, demonstrating the presence of organic residues beside the cobalt ferrite in both samples.

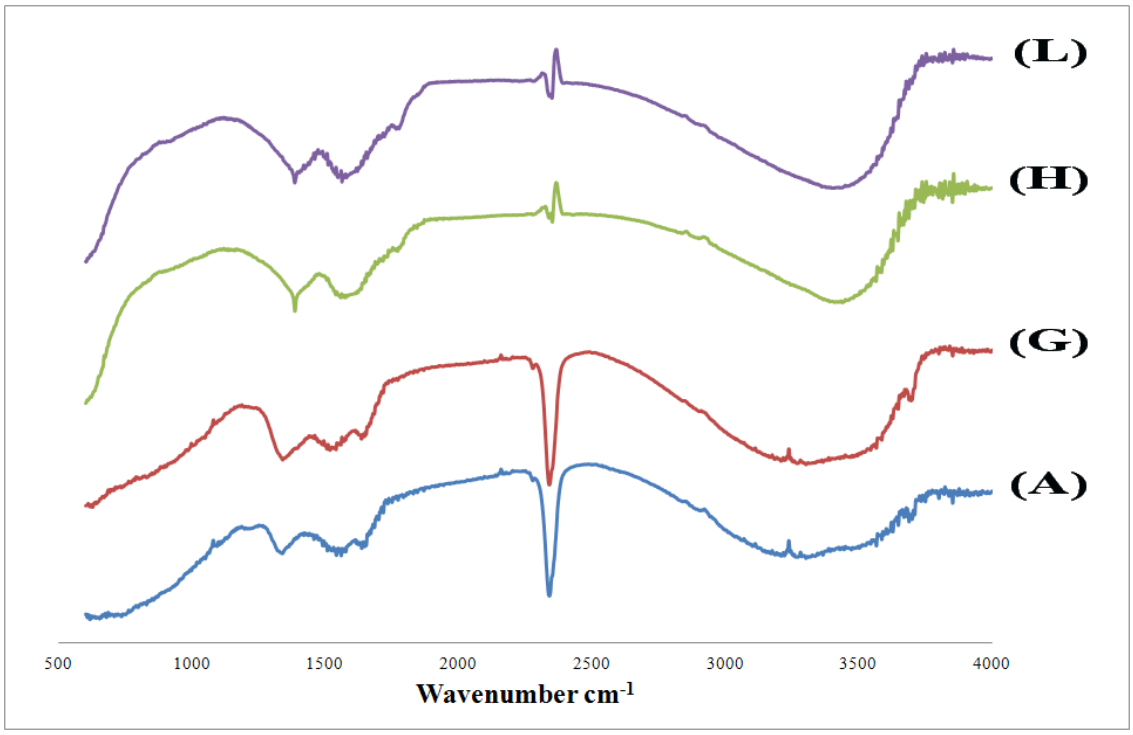

Figure 5.6 FTIR spectra of samples (A, G, H, L)

5.3.3 Morphology and particle size

As stated above in this chapter, the particle size of ferrite powders is crucially dependent on the temperature during the heat treatment [71, 77, 78]. The observed increase in the size at higher temperatures could be a result of the formation of crystalline clusters, clusters of crystals which have become cemented together. However, normally when particles come into contact with each other and under favourable energetic conditions, some of them grow, while others decrease in size and disappear altogether, and so the result is usually a smaller number of larger particles [59].

An FE-SEM image of particles made during the heat treatment carried out using the parameters indicated by G is shown in Figure 5.7. This image has been used to estimate the particle size distribution. The sample is composed of nanoparticles in the size range between 7 and 28 nm. The particles are smaller than those in the corresponding FE-SEM image, after the heat treatment parameters indicated by A were followed (Figure 4.11). It is evident that the increase in particle size visible in Figure 4.11 resulted because the heat treatment temperature was allowed to reach a much higher value, 600°C, in comparison with the temperature indicated by G, 250°C. A histogram of the particle size distribution of sample G is shown in Figure 5.8. As can be seen, the sizes of about 70% of the particles (The percentage refers to the total number of particles) are smaller than 15 nm. The asymmetric shape of the histogram may indicate that some agglomeration had taken place, with the formation of particles with larger sizes, e.g. around 25 nm.

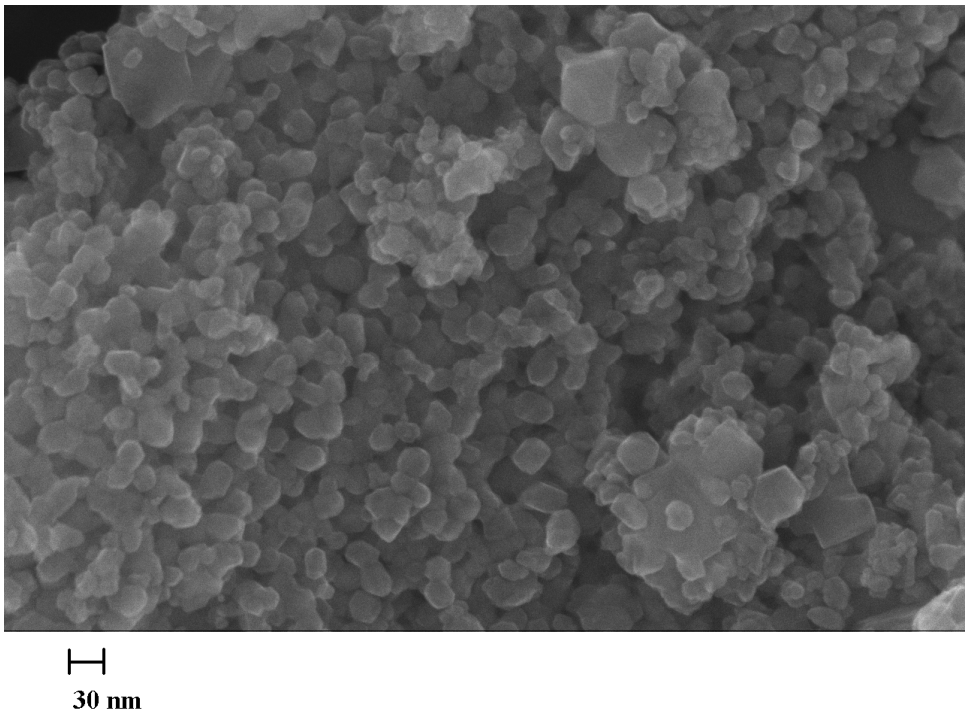

Figure 5.7 FE-SEM image of sample (G)

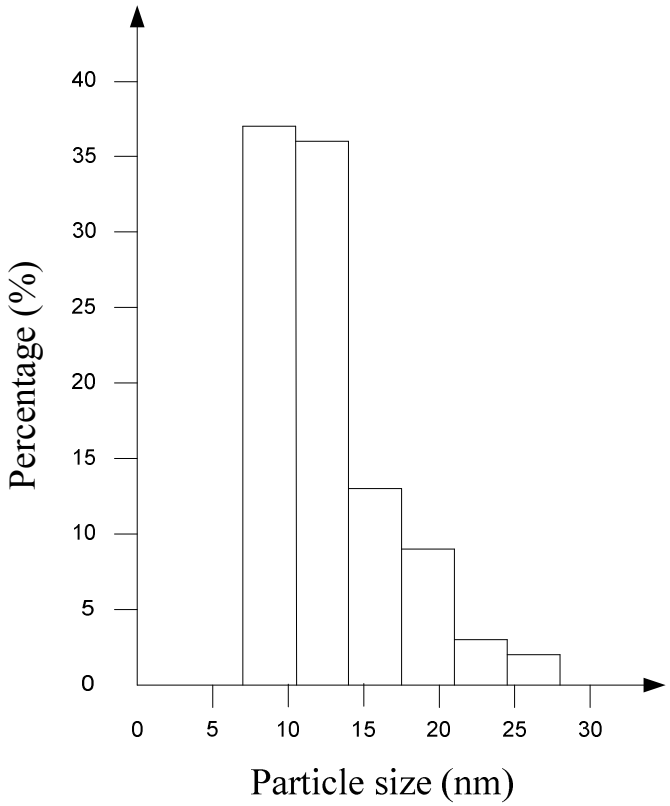

Figure 5.8 The particle size histogram of sample (G)

5.3.4 Magnetic properties

The magnetic properties of the nanoparticles in sample G were investigated in order to determine their magnetic state and to predict their behaviour in various circumstances. The hysteresis loop at room temperature is shown in Figure 5.9. The saturation magnetisation, the remnant magnetisation and the coercivity are found to be as follows 62emu/g, 22.5emu/g and 1250Oersteds, respectively (The magnetisation indicated in the figure refers to "mass magnetisation"). These results are in good agreement with one reference [74] but in obvious disagreement with another reference [65]. In this last reference the saturation magnetisation of particles with a size of 25 nm was estimated to be only 19emu/g. However, it should be noted that in this case no heat treatment was carried out at the end of the synthesis process. This omission could have had the effect that the particles might have been only partially crystalline and, in turn, this factor may have contributed to a reduction of the effective size of the particles. Particle size has an important role in decreasing the saturation magnetisation and therefore the omission of the heat treatment casts some doubt on the very low value for

the saturation magnetisation quoted in this reference. The low result for saturation magnetisation might be as well due to the presence of organic materials in the sample. If organics were present in large quantities, the magnetic properties would be poor when compared with pure cobalt ferrite, and therefore the magnetic saturation would be smaller. Furthermore, another reference can be quoted which gives support to the above conclusions is as follows: measurements on particles with a size of about 36 nm provide an estimate for a saturation magnetisation of 64emu/g [27].

Assuming that the above experimental results are correct, it is now necessary to investigate their significance. Firstly, drawing attention to the value of the saturation magnetisation, 62emu/g, this must be compared with the accepted bulk value of the saturation magnetisation of 80 emu/g [87, 133]. Is there any significance in the difference between these two results?

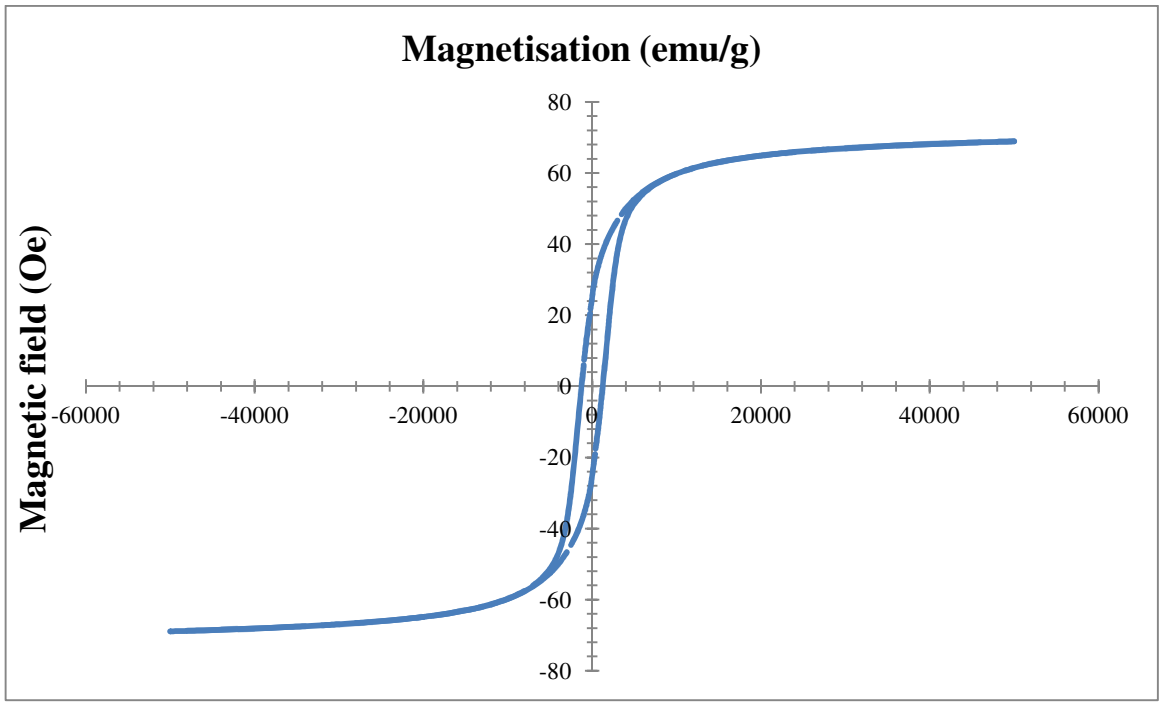

Figure 5.9 Hysteresis loop of sample (G) at 300 K

The saturation magnetisation, Ms, of powders is generally smaller than the bulk value and is found to be even smaller when the average particle size of powder is very small [72, 78, 79]. The reason for this may be as follows. If the particle size exceeds a critical diameter, there will usually be more than one magnetic domain in the particle. This allows the particle to have a complete magnetic circuit within itself, with the

magnetic field flowing along one side and back along the other side. However in single-domain nanoparticles, where the particle size does not exceed this critical diameter, there can be no internal magnetic circuitry. Because of this, in these small particles the spins of electrons near the particle surface are disordered compared with those near the centre of the particle. Therefore the electrons near the surfaces of these particles do not contribute to the magnetic properties of the material. The smaller the particle, the greater will be the proportion of its atoms which are close to the surface. Therefore in very small particles these surface effects are magnified, and in this case this surface effect contributes to lower the saturation magnetisation, Ms. The phenomenon may also be referred to as the influence of core-shell morphology and the finite-size effect [80, 81, 93, 95, 96].

Evidence points to the fact that the particles in samples A, B, C, D, E and F were larger than those in sample G. This is because during the preparation of each member of the series, different temperature set points were selected in the heat treatment operation and this resulted in different levels of thermal energy. Since the greater the temperature, the greater is the opportunity for particle growth, it is concluded that sample G, with particles in the size range between 7 and 28 nm had the smallest particles and that the sizes of the particles gradually increased in the series from sample F to sample A, which had the largest sizes, being in the range between 20 and 250 nm. It also follows that if the saturation magnetisation had been measured for each member of the series, the results would have indicated a gradual increase in this property following this series from sample G to sample A, with increasing particle size, approaching the bulk value of 80emu/g.

At this point the magnetic property which is being studied changes from the saturation magnetisation to the Coercivity, Hc. The result for sample G has already been given. It is 1250Oersteds, which is equivalent to 99.5kA/m.

In order to understand the significance of this result, it is useful to compare it with the bulk value, and the following approach has been used in an attempt to estimate this. Data is available showing the relationship between flux density and applied magnetic force for a sample of cobalt ferrite measuring 1 cm in diameter and 10 cm long. This is shown in Figure 5.10.

The numerical values behind this data are available and have been modified to remove the experimental fuzziness and then transformed into the same form as shown in Figure 5.9, showing the relationship between mass magnetisation and applied magnetic field. This is presented in Figure 5.11.

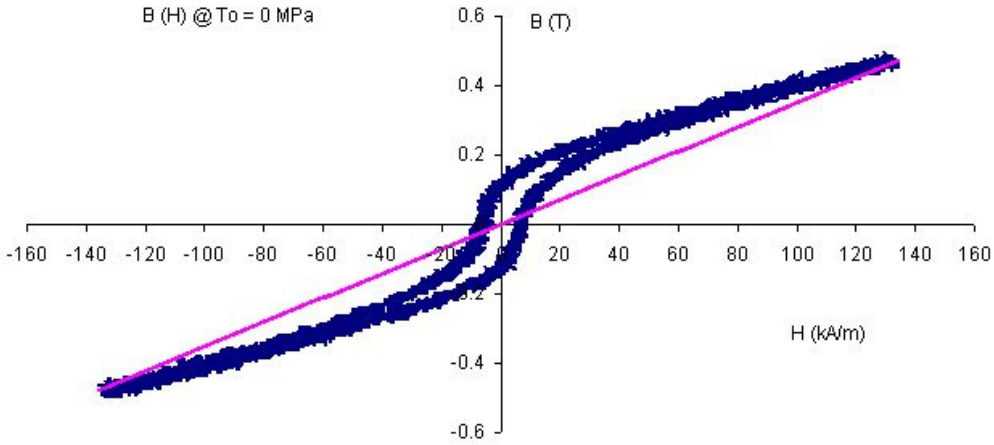

Figure 5.10 The relationship between flux density and applied magnetic force for a rod of cobalt ferrite [8]

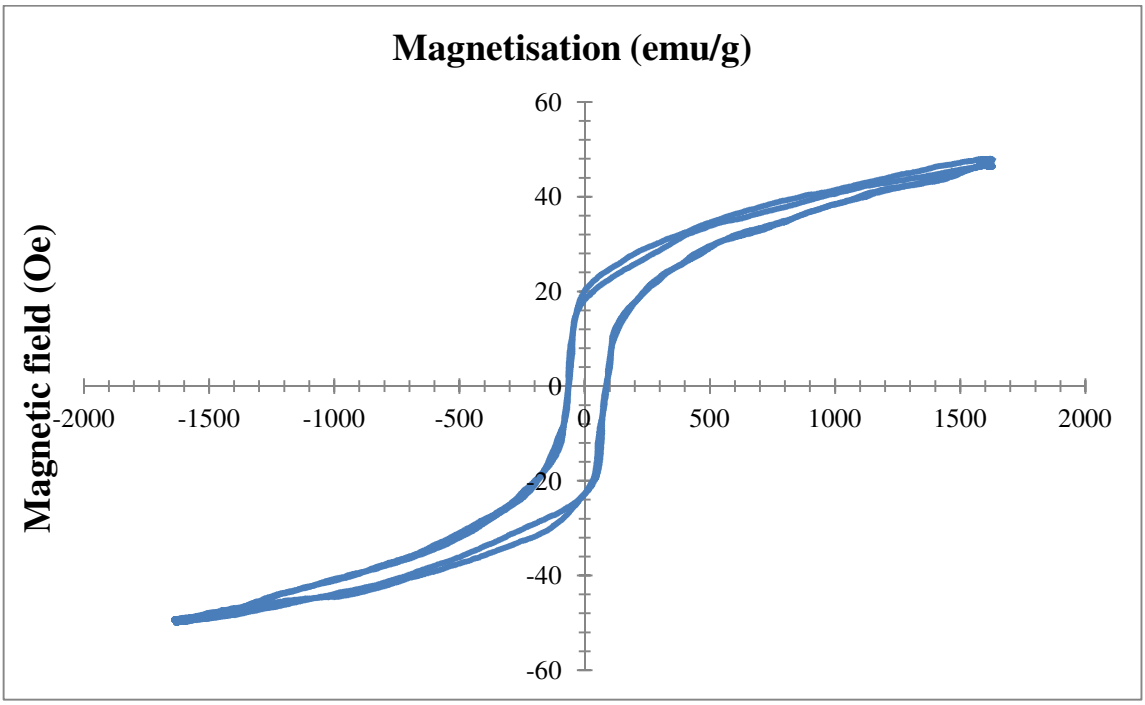

Figure 5.11 The relationship between mass magnetisation and applied magnetic field for a rod of cobalt ferrite

This data indicates that after the sample had been magnetised to a value of 48.2emu/g, it was necessary to apply a negative magnetic field of 74.7Oersteds to

reduce the magnetisation to zero again. This does not provide an estimate of the coercivity of the material directly, because this property can only be measured after the sample has been magnetised to the saturation magnetisation value, which is given in the literature as 80emu/g. However it is generally true that curves indicating the relationship between mass magnetisation and applied field strength are nearly parallel with each other except in regions a long way from the origin. In this case one can predict that the curve indicating the relationship between mass magnetisation and applied magnetic field strength at saturation would have the same shape as that shown above, except that where the magnetisation reaches a value of 80emu/g, or -80emu/g, the experimental lines would be parallel to the x axis, indicating that saturation magnetisation had been achieved. If the curves are parallel closer to the origin, one can estimate that the coercivity of the material as about 130Oersteds.

There are therefore two values for the coercivity of cobalt ferrite. One for the nanoparticles in sample G with a value of 1250Oersteds, and one for a rod measuring 1 cm in diameter and 10 cm long, with a rough estimate of the value of 130Oersteds. Is it possible that this property can change so much for very small particles?

The answer to that question is yes it can. In fact for all materials the coercivity increases with decreasing particle size until a maximum value is reached at a critical diameter corresponding to the transition stage from the multi to the single domain state. In both of these states the material is still ferrimagnetic. However, with further reduction in particle size, the coercivity decreases to zero, and at another critical diameter there is a second transition stage from the ferrimagnetic state to the superparamagnetic state [28, 59, 82, 83]. The coercivity of cobalt ferrite nanoparticles was found by some investigators to attain a maximum value at 29 nm [72]. Therefore, according to this reference, this size should be considered to be the critical diameter at which particles switch from the single into the multi domain state. It was estimated to be around 70 nm elsewhere [134].

Again it would have been very interesting if the magnetic properties had been measured for all the members of the series from sample A to sample G. In that case it might have been possible to find a maximum value for the coercivity in the data, and this would have established whether all the particles in sample G have only a single

magnetic domain or not. It would also have been useful in determining the critical diameter, where the change from the single to the multi domain occurs.

There are other ways of estimating this critical diameter. One way involves using a technique to make the domain walls in larger particles visible. The sizes of the domains in samples which are not magnetised can then be estimated, and this size should be the same as the critical diameter. Domains exist because of the large amount of energy that is required to establish a uniform magnetic field over a region in a sample. Although some energy is required to build a domain wall, the energy involved with the domain wall is much smaller than the energy required to establish a uniform magnetic field for large particles. However when the particles are very small the energy required to build the domain wall becomes relatively greater than the energy required to establish the uniform magnetic field. Therefore the minimum energy solution is to form particles where there is only one magnetic domain.

This explains why the coercivity of very small particles is so high in comparison with the bulk value. It reflects the amount of energy that is saved in the material when there is no magnetisation, and the material is free to form magnetic domains. This completes the review of magnetic properties carried out at room temperature.

It is now necessary to investigate the magnetic properties at low temperature. Figure 5.12 shows the hysteresis loop at 10 °K. The saturation magnetisation, the remnant magnetisation and the coercivity are 67.3emu/g, 52.5emu/g and 10,000Oersteds, respectively. The coercivity is therefore much greater at the low temperature. This result is in approximate agreement with the results of an investigation [82], in which the magnetic properties of particles with 15 nm as the average size were studied using a maximum applied magnetic field of 12kOe. The coercivity was estimated from measurements of the hysteresis loops recorded both at room temperature and at 77 °K. The value at 77 °K was higher than that at room temperature.

The remnant magnetisation, Mr, is defined as the magnetisation left in a sample after removing the applied magnetic field. Similarly, the coercivity, Hc, is defined as the applied magnetic field necessary to bring the magnetisation of a sample to zero. As a comparison between the two loops, Figure 5.9 and Figure 5.12, recorded at 300°K and at 10°K, reveals, some magnetic properties (Mr, Hc) are found to have higher values at

the lower temperature. This could be understood to be a result of energy barriers in nanoparticles becoming more apparent at lower temperatures. It is suggested that these barriers always exist, but they become more obvious at low temperatures, and they are barriers which retard magnetic moments from aligning towards the applied magnetic field. In this case, more time is required for the magnetic moments to relax resulting in higher values of Mr and Hc. Their existence may also become more noticeable because a stronger applied magnetic field is required to align the magnetic moments in nanoparticles.

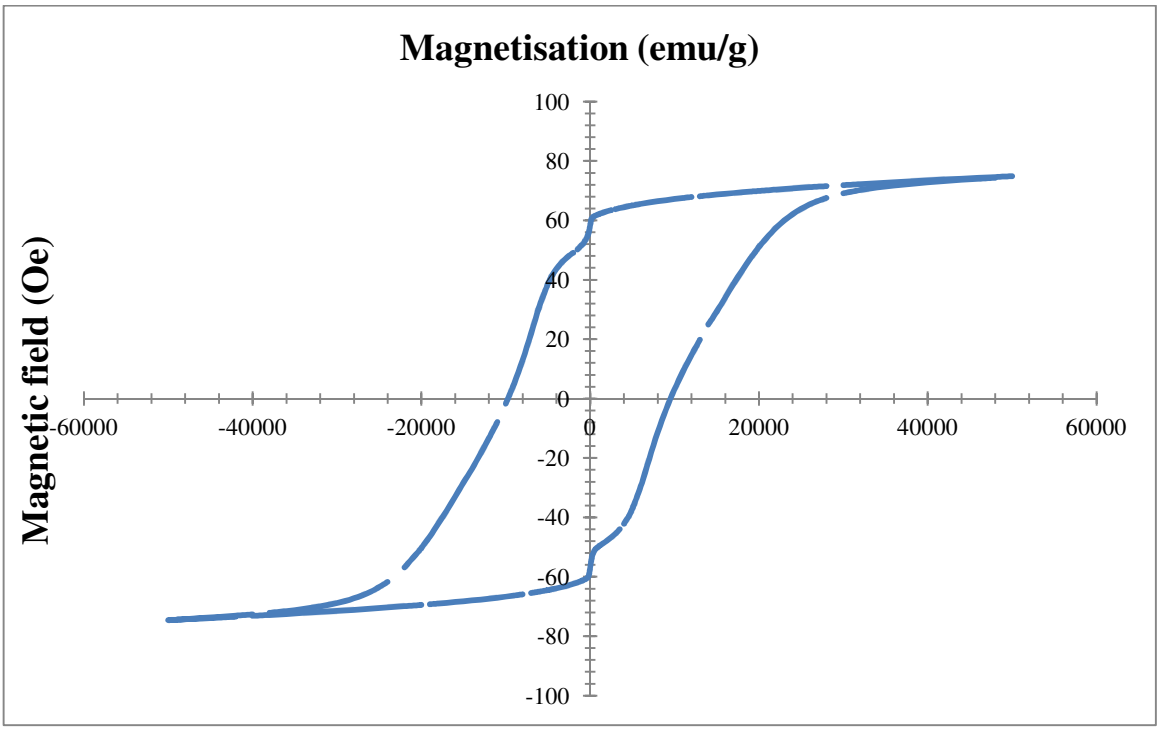

Figure 5.12 Hysteresis loop of sample (G) at 10 K

The corollary to the above explanation is that when heating up, the magnetic characteristics (Mr, and Hc) decrease in value due to energy barriers being overcome by thermal activation energy. Continuing along the same trend, the nanoparticles at a certain temperature enter into the superparamagnetic state where all magnetic moments fluctuate arbitrarily along the easy axes of magnetisation, and the same magnetic properties Mr and Hc, have zero values.

Cobalt ferrite single-domain nanoparticles can exist either in the ferrimagnetic or the superparamagnetic state. At room temperature, the superparamagnetic threshold estimated using the Néel theory, is reported to be about 10 nm [135]. In

superparamagnetic particles, magnetisation can flip randomly in direction under the influence of thermal agitation. The temperature of the transition from superparamagnetism to ferrimagnetism is called the blocking temperature, TB. It is the temperature at which both Hc and Mr decrease to zero [62]. It can also be regarded as the temperature at which the magnetic anisotropy energy barrier of a nano magnet is overcome by thermal activation, being equal to the average level of thermal energy in the material. This results in the fluctuation (the random flip in direction) of its magnetisation.

In the previous paragraph an estimate was reported for the transition temperature between the superparamagnetic and the ferrimagnetic state, if the particle size is about 10nm. It was room temperature. This is of particular significance in view of the particle size distribution of sample G. The particle sizes in the sample range from 7 nm to 28 nm, with about one third of the number of the nanoparticles consisting of particles below 10 nm. While it is important to avoid trying to force the interpretation of the words “about 10 nm” into providing exact information, this estimate raises the possibility that perhaps a third of the nanoparticles of sample G consists of particles that are in the superparamagnetic state. If this were true, the measurements given above of coercivity and remnant magnetisation at room temperature would refer only to the 67% of the nanoparticles of sample G which consisted of larger particles in the ferrimagnetic state. To investigate this more thoroughly another set of properties was measured.

In most of the work on these aspects of magnetism at present, investigators are concerned to measure the properties of particles that are much smaller than 10 nm, and therefore the temperature of the transition from the ferrimagnetic to the superparamagnetic state occurs at temperatures which are well below room temperature. Investigators have found that the properties of these materials are different depending on certain features which were or were not present when the samples were cooled down as they passed through the transition from the superparamagnetic to the ferrimagnetic state. In particular they depend on whether there was a magnetic field during this cooling period. The two conditions are referred to as “field cooled”, that is, there was an applied magnetic field at the time of the cooling of the sample, or “zero field cooled”, that is, there was no applied magnetic field at the time that the sample was cooled

through the transition temperature and changed from the superparamagnetic state to the ferromagnetic state.

The temperature dependence of magnetisation under zero-field cooled (ZFC) conditions for sample G is shown as a curve in Figure 5.13. The Figure shows that magnetisation increases with temperature. For each measurement the magnetisation was determined at the same applied magnetic field strength of 500Oersteds. This magnetic field must have been switched off while the sample was cooled through the transition temperature and then switched on again once a low temperature had been achieved. In other investigations, while the sample is in the ferrimagnetic state, the magnetisation increases with temperature, then it reaches a maximum value at the transition temperature between the ferrimagnetic state and the superparamagnetic state, and then it decreases as the temperature continues to rise. The curve in Figure 5.13 therefore seems to indicate that the majority of particles in sample G are still in the ferrimagnetic state at 300°K or room temperature. However it should be noted that the investigations mentioned above were carried out using samples of magnetic particles which had a very small range of sizes, whereas sample G contains particles with a larger range of sizes. Now it is probable that the maximum value of the magnetisation would be more difficult to identify in a sample composed of particles with a large range of sizes, because the change from one state to the other would be more gradual. Nevertheless the evidence from Figure 5.13 seems to be decisive, because there is no indication of an interruption away from the upward trend in the values of magnetisation as the temperature increased.

Due to the noticeable difference between values for the coercivity measured at 10 °K and 300 °K, it is still possible that the majority of particles in sample G are close to the transition point of entry into the superparamagnetic state. This is considered a possibility because of the suggestion that the coercivity might be the result of energy barriers which must be overcome by an increase in temperature, in a similar way to that of reactions requiring activation energy. This possibility is strengthened if the words above “about10 nm” are applied to indicate that the smaller particles in sample G have already passed into the superparamagnetic state, because the transition temperature or blocking temperature for particles with a size of 10 nm is estimated to be 300 °K.

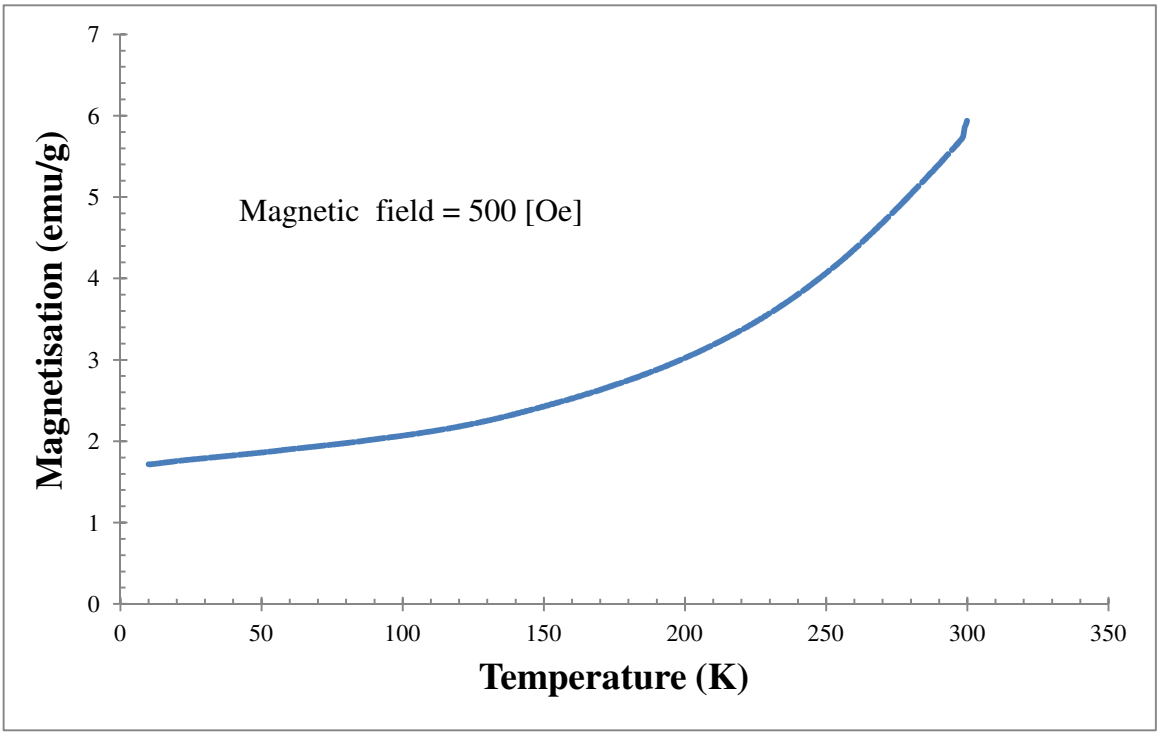

Figure 5.13 Temperature dependence of magnetisation in ZFC of sample (G)

Ferrimagnetic behaviour is generally observed in one of the following two alternative sets of circumstances. Firstly, for a sample of nanoparticles with a monodisperse distribution of particle size, ferrimagnetic behaviour is detected at relatively low temperatures as it is essential to cross the blocking temperature by cooling down to transfer from the superparamagnetic to the ferrimagnetic state. Secondly, for a sample of nanoparticles that has a range of particle sizes, i.e. a polydisperse distribution, some nanoparticles with a relatively larger size have a higher blocking temperature than those particles with a smaller size. It is also possible that the blocking temperature for the larger particles could be higher than room temperature. It is believed that the latter set of circumstances is more applicable to this study as sample G contains nanoparticles in the size range of 7-28 nm. The hysteresis loop formed by measuring the properties of sample G at room temperature is significantly narrower than the corresponding hysteresis loop of properties measured at 10 °K.

The magnetic properties of the nanoparticles in sample G were investigated in order to determine their magnetic state. Using data from other sources, if the particles are larger than 29 nm, (or possibly 70 nm) they have more than one magnetic domain. If they are smaller than 29nm but larger than 10 nm, they are ferrimagnetic, but have only one magnetic domain. If they are smaller than 10 nm, they are not ferrimagnetic at room

temperature but are superparamagnetic. The particles in sample G had a size range between 7 and 28 nm., and this suggests that there were no particles with more than one magnetic domain, and while most of the particles were ferrimagnetic and had only one domain, a minority had superparamagnetic characteristics.

The magnetic properties that were measured confirm that ferrimagnetic characteristics are present when measurements are carried out at room temperature. However it is not possible to be more definite about the magnetic state of the particles than this. It would have been valuable to have been able to measure the coercivities of samples A to F at room temperature. This should have indicated that there is a maximum coercivity for one of the members of the series from sample A to sample G, and in turn this would have provided a new indication of the particle size at the transition between the single domain state and the multi-domain state. It would in turn have indicated that no particles in sample G had more than one domain.

It might also have been valuable to have extended the data on the magnetisation of sample G under an applied magnetic field of 500Oersteds. Measurements have been made in the temperature range between 10°K and 300°K, but this did not extend to temperatures between 300 °K and 525 °K. (Above 525°K irreversible changes would occur in the sample) It would have been valuable to establish whether the graph of magnetisation against temperature has a maximum value at some point in the extended temperature range. If this maximum could be found experimentally, it would confirm that there is a transition at room temperature for particles with a size of 10 nm between the ferrimagnetic state and the superparamagnetic state. This would also confirm that a minority of the particles in sample G have superparamagnetic characteristics.

5.4 Summary

Variations of the parameters of the heat treatment operation, the final stage in the preparation of cobalt ferrite nanoparticles were investigated. The spinel structure was formed in all the products, but in some cases other phases were also present. The impurities in the products were identified. The lowest temperature and shortest dwell time required to prepare cobalt ferrite nanoparticles with a single phase were determined, using techniques involving DTA/TGA equipment and FTIR spectra. The heat treatment parameters of 250 °C and 10 h, which were the set points chosen for the

production of sample G, were selected because they ensured the complete elimination of impurities in the product, while also providing the smallest opportunity for the particles to grow to larger sizes. An FE-SEM image of sample G demonstrated that it was composed of nanoparticles in the size range between 7 and 28 nm. Relevant magnetic properties demonstrated the ferrimagnetic behaviour at room temperature of sample G with a saturation mass magnetisation of 62emu/g. With heat treatment parameters as low as 250 °C and 10 h, the method of preparation described in this thesis is a significant improvement over the methods reported by other investigators in the state of the art literature.

Chapter 6

The modelling and optimisation of the heat treatment operation

6 The modelling and optimisation of the heat treatment operation

6.1 Introduction

The main challenge, at this point, for the person who prepares a powder, is to choose the heat treatment parameters that will facilitate the attainment of cobalt ferrite powder with the required specifications. It is usually a time consuming trial and error procedure even when there are inputs chosen with skill by that person. Eventually, the chosen inputs result in the production of a sample of powder close to the required specifications. Interestingly, there are often alternative ideal heat treatment parameters that can be adopted, once they have been determined. However, there are now various methods for obtaining the desired output variables, to accurately predict the heat treatment ideal parameters without consuming large amounts of materials, time, labour effort and money. These methods use models' development. Recently, DoE has been employed for many applications in different areas [136, 137].

This chapter contains a report of treatments carried out on the amorphous powder which had been prepared employing the sol–gel technique, using the same procedures as those given in the previous chapters. During the heat treatment operation, nanoparticles tend, not only to agglomerate, but also to grow and form undesirable large particles and this is due to the thermal energy made available because of the high temperatures. Furthermore, employing high temperatures and prolonged dwelling times

results in high electrical operating costs. Therefore, it is usually favourable to lower the heat treatment temperature and shorten the dwell time to reduce the cost but not to the limit where the conditions become insufficient to cause the oxidation of the organic contents in the amorphous powder.

Response surface methodology (RSM) was used to establish the mathematical relationships between the two heat treatment input parameters (the temperature and the dwell time) and the two responses (the purity of the powder and the electrical operating cost of the operation). The resulting mathematical models were experimentally validated. The optimisation capabilities in Design-Expert 7.0 were used to improve the heat treatment operation. Optimal heat treatment conditions were determined. Employing the optimum set of conditions, an experiment was carried out on a sample of the amorphous powder, and a structural characterisation of the sample was performed subsequently.

6.2 Methodology

6.2.1 Response surface methodology

Engineers often wish to determine the values of the process input parameters at which the responses reach their optimum. The optimum could be either a minimum or a maximum of a particular function in terms of the process input parameters.

Response surface methodology (RSM) is one of the optimisation techniques currently in widespread use which analyses the quantitative data collected from the experiment and describes the performance of the different processes, predicts the responses of interest affected by the input variables of the experiment and finds their optimum values [138]. In other words, RSM is a set of mathematical and statistical techniques that are useful for modelling and predicting the response of interest affected by a number of input variables with the aim of optimising this response [139]. RSM also specifies the relationships among one or more measured responses and the essential controllable input factors [140].

When all independent variables are measurable, controllable and continuous in the experiments, with negligible error, the response surface can be expressed by Eq. 1.

$$y = f(x_1, x_2, \ldots x_k) \quad (1)$$

Where: k is the number of independent variables.

To optimise the response "y", it is necessary to find an appropriate approximation for the true functional relationship between the independent variables and the response surface. Usually a second order polynomial is used in RSM as shown in Eq. 2.

$$y = b_o + \sum b_i \chi_i + \sum b_{ii} \chi_{ii}^2 + \sum b_{ij} \chi_i \chi_j + \varepsilon \quad (2)$$

Where: b_0, b_i, b_{ii} and b_{ij} are the coefficients for the independent variables. They are constants that are multiplied by the factors in a mathematical model. They are often referred to as "b-coefficients" in DoE. Moreover, ε is the error term.

6.2.2 Experimental design

The design is based on a two-factor, face-central composite design, with full replication [139]. In order to find the range of each process input parameter, trial runs are usually performed by changing one of the process parameters at a time. The same procedure was followed in this study. The process input variables are the temperature and the dwell time. Increasing the heat treatment temperature, up to 600 °C, results in the complete oxidation of the organic content as indicated in the previous chapter. However, one can observe that most of the oxidation reactions occur in the temperature range between 200 and 300 °C as shown in Figure 6.1. Further trials showed that by adopting different dwell times, between 2 and 10 hours, it became possible to narrow the range of temperatures of interest down to between 225 and 275 °C. Table 6-1 shows the process variables, with their coded and actual values. Statistical software in Design-Expert 7.0 was used to code the variables and to establish the design matrix shown in Table 6-2. RSM was applied to the experimental data using the same software; a polynomial, Eq. 2, was fitted to the experimental data to obtain the regression equations for all responses. The statistical significance of the terms in each regression equation was examined using the sequential F-test, the "lack-of-fit" test and other adequacy measures. Finally the same software was used to obtain the best fit.

The run order specified in Table 6.2 was carried out, and the results are shown in the column headed by "Purity [%]". This heading could be more accurately called the "Level of Impurity", because it gives an indication of the concentration of impurities in the sample after the heat treatment. The values were obtained from the experimental data as follows. The weight of each sample of the amorphous powder was recorded

before each trial run. Then after the heat treatment, the weight was recorded again. The final weight divided by the initial weight expressed as a percentage is the value given in Table 6-2 under the Purity column. The level of impurity is given approximately by subtracting 16% from this value (as explained in chapter 5, section 5.3.1).

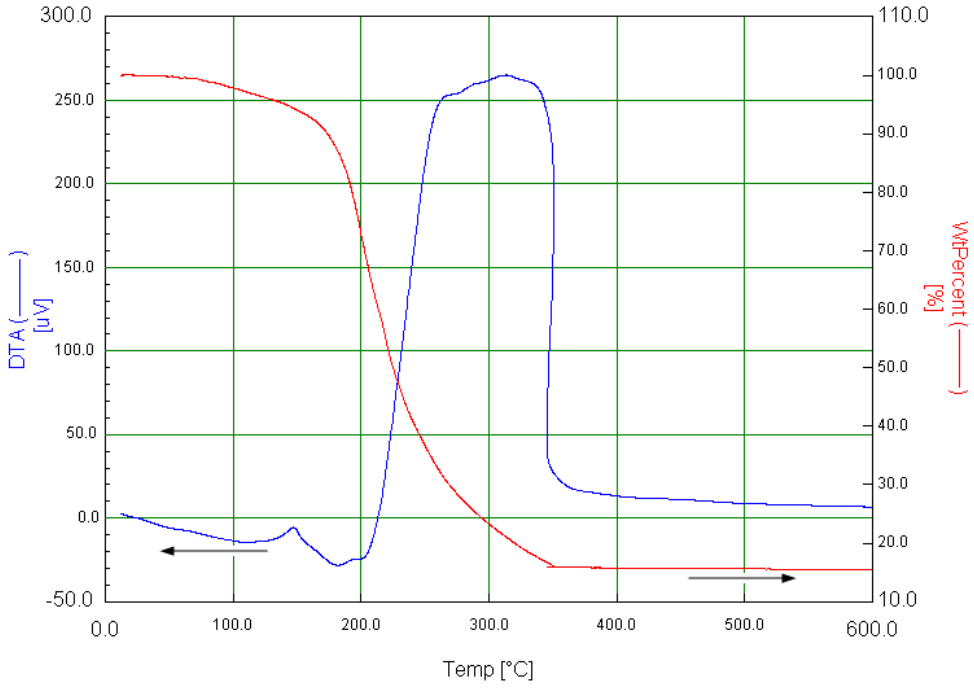

Figure 6.1 DTA/TGA curves of amorphous powder

Table 6-1 Independent variables and experimental design levels used

Variable	Notation	Unit	Limits		
			-1	0	1
Time	A	[h]	2	6	10
Temperature	B	[°C]	225	250	275

6.2.3 Desirability approach

There are many statistical techniques for solving multiple response problems such as overlaying the contours plot for each response, constrained optimisation and desirability approach. The desirability method is recommended due to its simplicity and availability in the software. It provides flexibility in weighting and giving importance for each response individually. The method of solving such multiple response

optimisation problems employing this technique consists in using a technique for combining multiple responses into a dimensionless measurement of performance known as the overall desirability function. The desirability approach consists in transforming each estimated response, Y_i, into a unitless utilities function bounded by $0 < d_i < 1$, where a higher d_i value indicates that the response value Y_i is more desirable. If $d_i = 0$, this means that there is a completely undesired response and, vice versa, when $d_i = 1$, the response is totally desired, in the sense that there is no undesirable aspects involved in it [141].

In the current study the individual desirability for each response d_i is calculated using Eqs. 3 to 6, where T_i is the target value of i^{th} response. The shape of the desirability function can be changed for each goal by the weight field 'wt_i'. Weights are used to give more emphasis to the upper/lower bounds or to emphasise the target value. Weights could be ranged between 0.1 and 10; a weight greater than one gives more emphasis to the goal, while weights less than one give less emphasis. When the weight value is equal to one, this will cause the d_i functions to vary from zero to one in a linear mode. In the desirability objective function (D), each response can be assigned an importance factor (r), relative to the other responses. Importance varies from the least important, a value of 1(+), to the most important, a value of 5(+++++). If varying degrees of importance are assigned to different responses, the overall objective function is shown in equation 7 below. Where n is the number of responses to be considered [142].

For a goal of a maximum, the desirability will be defined by:

$$d_i = \begin{cases} 0 & , \quad Y_i \le Low_i \\ \left(\dfrac{Y_i - Low_i}{High_i - Low_i} \right)^{wt_i} & , \quad Low_i \langle Y_i \langle High_i \\ 1 & , \quad Y_i \ge High_i \end{cases} \tag{3}$$

For a goal of a minimum, the desirability will be defined by:

$$d_i = \begin{cases} 1 & , \quad Y_i \le Low_i \\ \left(\dfrac{High_i - Y_i}{High_i - Low_i} \right)^{wt_i} & , \quad Low_i \langle Y_i \langle High_i \\ 0 & , \quad Y_i \ge High_i \end{cases} \tag{4}$$

For a goal as a target, the desirability will be defined by:

$$d_i = \begin{cases} \left(\dfrac{Y_i - Low_i}{T_i - Low_i} \right)^{wt_{1i}} & , \quad Low_i \langle Y_i \langle T_i \\ \left(\dfrac{Y_i - High_i}{T_i - High_i} \right)^{wt_{2i}} & , \quad T_i \langle Y_i \langle High_i \\ 0 & , \quad Otherwise \end{cases} \tag{5}$$

For a goal within a range, the desirability will be defined by:

$$d_i = \begin{cases} 1 & , \quad Low_i \langle Y_i \langle High_i \\ 0 & , \quad Otherwise \end{cases} \tag{6}$$

$$D = \left(\prod_{i=1}^{n} d_i^{r_i} \right)^{\frac{1}{\sum r_i}} \tag{7}$$

6.2.4 Optimisation

The optimisation part in Design-Expert 7.0 searches for a combination of factor levels that simultaneously satisfies the requirements placed (i.e. optimisation criteria) on each one of the responses and process factors (i.e. multiple response optimisation). Numerical and graphical optimisation methods were used in this work by selecting the desired goals for each factor and response. As mentioned above the numerical optimisation process involves combining the goals into an overall desirability function (D). The numerical optimisation feature in the Design-Expert package finds one point or more in the factors domain that would maximise this objective function. In a graphical optimisation with multiple responses, the software defines regions where requirements simultaneously meet the proposed criteria. Also, superimposing or overlaying critical

response contours can be defined on a contour plot. Then, a visual search for the best compromise becomes possible. In the case of dealing with many responses, it is recommended to run numerical optimisation first; otherwise it could be impossible to find a feasible region. The graphical optimisation displays the area of feasible response values in the factor space [142]. Figure 6.2 shows the flow chart of optimisation steps in Design-Expert 7.0 [136].

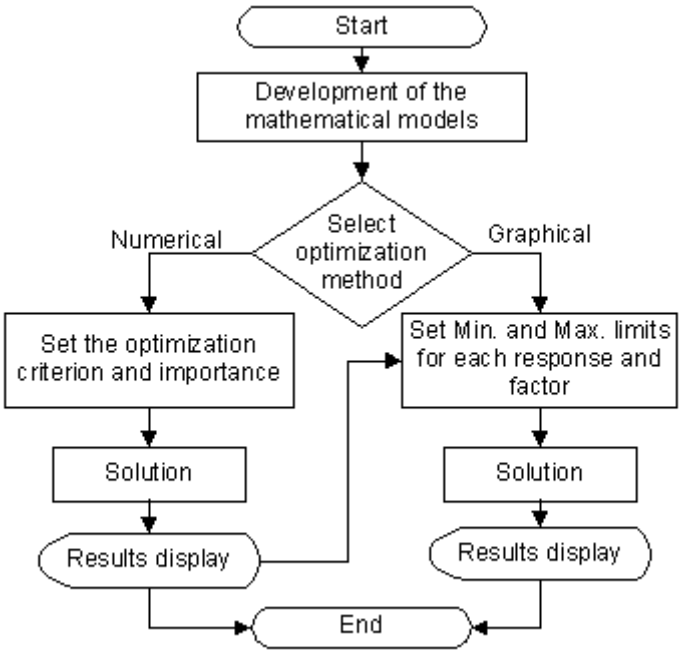

Figure 6.2 Optimisation Steps [136]

6.3 Experimental work

6.3.1 Material development

Heat treatment experiments were carried out on samples of the amorphous powder prepared employing the sol–gel technique. The method is based on the formation of a stable and homogenous sol obtained by the hydrolysis and condensation reactions of a blend of Cobalt (II) nitrate hexahydrate, ($Co(NO_3)_2.6H_2O$, ≥99%, Fluka) and Iron (III) nitrate nonahydrate, ($Fe(NO_3)_3.9H_2O$, ≥98%, Sigma-Aldrich) as shown in Figure 6.3. The precursors were used without any further purification with a molecular ratio, Co to Fe, equal to 1:2. The quantity of citric acid was stoichiometrically double the sum of the metal ions.

Table 6-2 Design matrix

No	Run order	Parameters		Responses	
		A	B	Purity [%]	Operating cost [€]
1	12	2	225	27.426	0.11232
2	9	10	225	20.763	0.5616
3	10	2	275	16.17	0.13728
4	1	10	275	16.055	0.6864
5	3	2	250	21.61	0.1248
6	6	10	250	16.087	0.624
7	11	6	225	23.849	0.33696
8	4	6	275	16.034	0.41184
9	2	6	250	16.45	0.3744
10	8	6	250	16.525	0.3744
11	7	6	250	16.667	0.3744
12	13	6	250	16.732	0.3744
13	5	6	250	16.523	0.3744

6.3.2 Electrical operating cost estimation

The electrical operating cost was calculated using the following equation:

Electrical operating cost [€] = $(0.12/1000)*A*V*(T-T_r/T_{max}-T_r)*t$

This was simplified slightly to:

Electrical operating cost [€] = $(0.12/1000)*A*V*(T/T_{max})*t$

$$= 0.0002496*(T*t) \quad (8)$$

Where: The cost of 1 kWh of electricity is taken as €0.12 , A is the average current used by the furnace when set to reach the maximum temperature over the duration of the total time spent in operating the equipment, it is 13 amps, V is the Nominal voltage of the furnace [240 V], T is the Heat treatment temperature [°C], T_{max} is the Maximum temperature of the equipment [1500 °C], T_r is the room temperature [°C] and t is the Heat treatment dwell time [h].

6.4 Results and discussion

6.4.1 The development of mathematical models

The "fit summary" tab in Design-Expert 7.0 suggests the highest order polynomial where the additional terms are significant and the model is not aliased. Selecting the step-wise regression method eliminates the insignificant model terms automatically. The sequential F-test for significance of both the regression model and the individual model terms along with the lack-of-fit test were carried out using Design-Expert 7.0. The Analysis of Variance (ANOVA) for the reduced quadratic models summarises the analyses of both responses and shows the significant model terms. Table 6-3 and Table 6-4 show the ANOVA results for the purity and electrical operating cost respectively. The same tables show also the other adequacy measures R^2, Adjusted R^2 and predicted R^2. All the adequacy measures are in reasonable agreement. They indicate significant relationships. The adequate precision ratios in all cases are greater than 4 which indicate that the models are adequate. The analysis of variance results for the purity and electrical operating cost models show the main effect of the two heat treatment parameters and their quadratic effects, along with the interaction effect of these two parameters. They are all shown to be significant model terms. Nevertheless, the temperature is the factor most associated with the purity of the final product and the dwell time is the factor most associated with the electrical operating cost. According to these software results, the models that have been developed are statistically accurate and can be used for further analysis. The final models in terms of coded and actual factors are shown below in Eqs.9 to12.

$$\underline{\text{Purity}} = 16.87 - 2.05 * A - 3.96 * B + 1.64 * AB + 1.25 * A^2 + 2.34 * B^2 \quad (9)$$

$$\underline{\text{Electrical operating cost}} = 0.37 + 0.25 * A + 0.037 * B + 0.025 * AB \quad (10)$$

$$\underline{\text{Purity}} = 321.43661 - 5.54395 * \text{Time} - 2.13265 * \text{Temp.} + 0.016370 * \text{Time} * \text{Temp.} + 0.078242 * \text{Time}^2 + 3.75181\text{E-}003 * \text{Temp.}^2 \quad (11)$$

$$\underline{\text{Electrical operating cost}} = 6.15841\text{E-}017 - 9.34976\text{E-}017 * \text{Time} + 4.91540\text{E-}019 * \text{Temp.} + 2.49600\text{E-}004 * \text{Time} * \text{Temp.} \quad (12)$$

It was noticed the anomaly between run 8 and run 4, where the purity is seen to become poorer when the dwell time is increased for 6 to 10 hours. This is experimental error. However, the last 5 runs are done to establish the experimental accuracy.

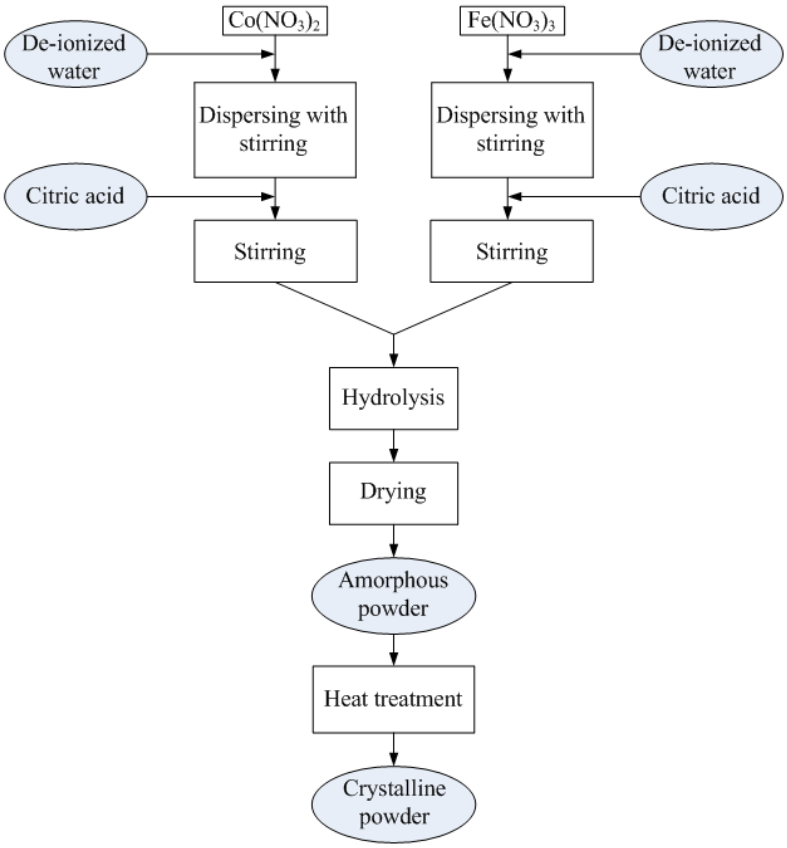

Figure 6.3 Material preparations

6.4.2 Confirmation experiments

In order to validate the developed models, three confirmation experiments were carried out with heat treatment conditions chosen randomly. From the experimental responses, the average of three measured results for each set of heat treatment conditions was calculated. Table 6-5 summarises the sets of conditions for the three experiments, the averages of actual experimental values, the predicted values and the percentages of error. The validation results demonstrated that the models developed are quite accurate as the percentages of the errors between the predictions and the experimental results were small.

Table 6-3 ANOVA for the purity model

Source	SS	DOF	MS	F value	Prob > F	
Model	160.2317	5	32.0463	48.31	< 0.0001	significant
A-Time	25.2191	1	25.2191	38.02	0.0005	
B-Temp.	94.2401	1	94.2401	142.08	< 0.0001	
AB	10.7191	1	10.7191	16.16	0.0051	
A^2	4.3285	1	4.3285	6.53	0.0379	
B^2	15.1862	1	15.1862	22.89	0.0020	
Residual	4.6431	7	0.6633			
Lack of Fit	4.5893	3	1.5298	113.64	0.0003	significant
Pure Error	0.0538	4	0.0135			
Cor Total	164.8748	12				
$R^2 = 0.9718$				$Adj\text{-}R^2 = 0.9517$		
$Pre\text{-}R^2 = 0.7786$				Adeq Precision = 23.252		

6.4.3 The effect of heat treatment parameters on the responses

During the heat treatment operation, the powder weight decreases and at a certain point it starts to have a constant value as shown in Figure 6.4. However, the "purity" in this chapter refers to the remaining material in a sample expressed as a percentage of the initial weight of the sample, before the heat treatment. This percentage must approach towards a minimum because there is a lower limit to the weight of the sample and no experimental results can go beyond this. The minimum value of the "purity" is the sample weight expressed as a percentage of the initial weight, when the sample is composed entirely of cobalt ferrite free of any organic or inorganic components.

In Figure 6.4 it can be seen that the purity is more responsive to the temperature, line B than to the dwell time, line A. In other words, increasing the heat treatment temperature results in a larger enhancement in the purity than when increasing the dwell time although the effect at higher temperatures is very small. This is of course due to the initial choice of the range of the parameters. Both effects can be attributed to the greater amount of thermal energy received by the samples either at the higher temperatures or for the longer period, and it is the thermal energy which facilitates the oxidation reactions of the organic components present in the amorphous powder.

Table 6-4 ANOVA for the electrical operating cost model

Source	SS	DOF	MS	F value	Prob > F	
Model	0.3847	3	0.1282	63660000	< 0.0001	significant
A-Time	0.3738	1	0.3738	63660000	< 0.0001	
B-Temp.	0.0084	1	0.0084	63660000	< 0.0001	
AB	0.0025	1	0.0025	63660000	< 0.0001	
Residual	0.0000	9	0.0000			
Lack of Fit	0.0000	5	0.0000			
Pure Error	0.0000	4	0.0000			
Cor Total	0.3847	12				
$R^2 = 0.9999$				$Adj\text{-}R^2 = 0.9999$		
$Pre\text{-}R^2 = 0.9999$						

Table 6-5 Validation test results

Exp. No.	Temp., °C	Time, h		Purity, %
1	240	5	Actual	19.492
			Predicted	19.585
			Error %	-0.477
2	260	2	Actual	17.373
			Predicted	18.307
			Error %	-5.376
3	250	9	Actual	16.25
			Predicted	16.034
			Error %	1.329

Figure 6.5 shows the relationship between the "purity" on the one hand, and the heat treatment input parameters (temperautre and dwell time) on the other. It is apparent from the results that both of the operational input parameters have significant effects on the purity of the resulting powder. If the heat treatment temperature is set to a certain value, following the solid lines in the Figure, the value shown in the Figure as "purity" decreases. This indicates that the impurity level decreases, and the real purity increases, as the dwell time is extended. If the heat treatment dwell time is set to a certain value, an invisible vertical line from one of the solid lines to the other must be followed. At high temperatures the value shown in the Figure as "purity" is lower, which indicates

that the impurity level is smaller, and the real purity is found to improve as the temperature is increased.

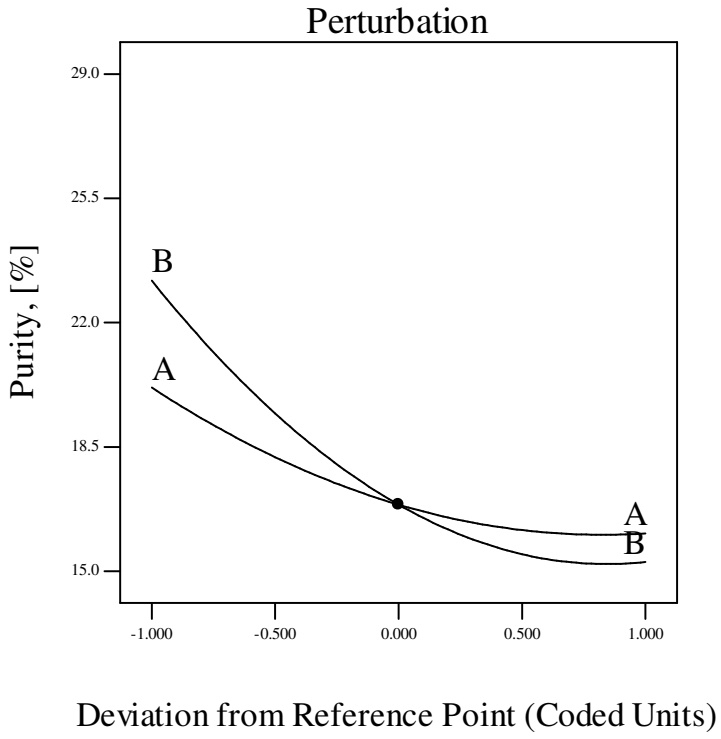

Figure 6.4 Perturbation plot shows the purity [%] as a function of A: dwelling time, and B: temperature

Referring to Figure 6.5 again, the interactive relationship between the purity and the heat treatment input parameters can be seen. It is evident that at higher temperatures, the effect of the dwell time on the purity tends to be relatively insignificant. Figure 6.6 shows the contours plot which illustrates the combined effect of temperature and dwell time on the purity.

It is shown in equation 8 that both of the process input parameters have a significant effect on the electrical operating cost of the heat treatment operation. Figure 6.7 shows the electrical operating cost in € as a function of the dwell time and temperature. As Table 6-2 and Figure 6.7 show, the electrical operating cost is found to increase to a greater extent when extending the dwell time, line A, in comparison with the increase which occurs when raising the temperature, line B, during the heat treatment operation. In other words, extending the heat treatment dwell time at a certain temperature results in relatively higher electrical costs than when increasing the heat

treatment temperature during a short dwell time. Figure 6.8 shows the contours plot which illustrates the combined effect of temperature and dwell time on the electrical operating cost.

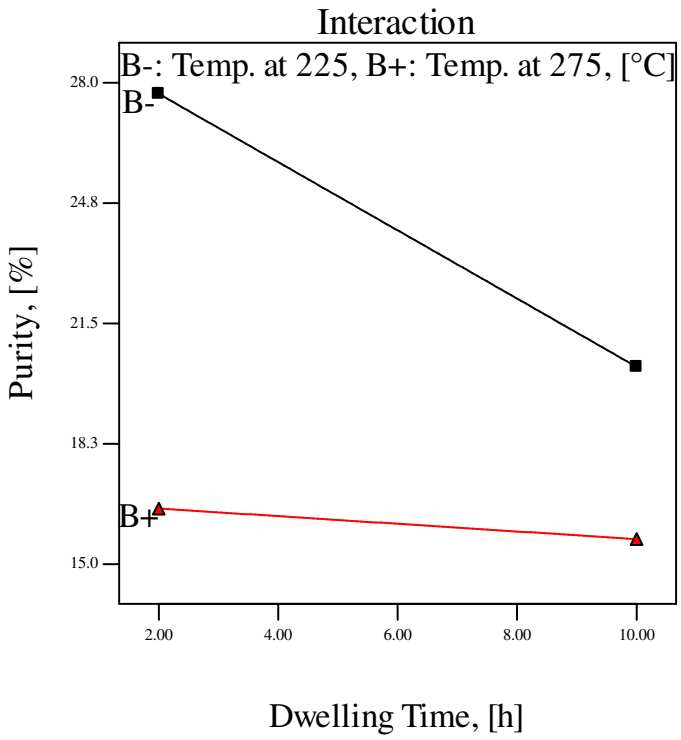

Figure 6.5 Interaction relationship between the purity and the heat treatment input parameters

During the heat treatment operation, decomposition and oxidation reactions of the organic component generally occur. In addition, the crystalline spinel structure of cobalt ferrite is also formed by means of an inter-diffusional migration. Therefore, it is also necessary to select a dwell time for the heat treatment which is sufficient to allow the inter-diffusional migration to take place and so to ensure the formation of the spinel structure as a single phase without any other oxides remaining. On the other hand, heat treatment at high temperatures for long periods results in growth in the sizes of the particles [58, 143].

As these results indicate, the formation of the spinel structure as a single phase without impurities can occur under a number of different sets of conditions. However, to reduce the electrical operating cost of the heat treatment operation and to avoid as much as possible the growth in the sizes of the particles because larger particles are

undesirable, there is a further need to carry out a further optimisation procedure in the heat treatment conditions.

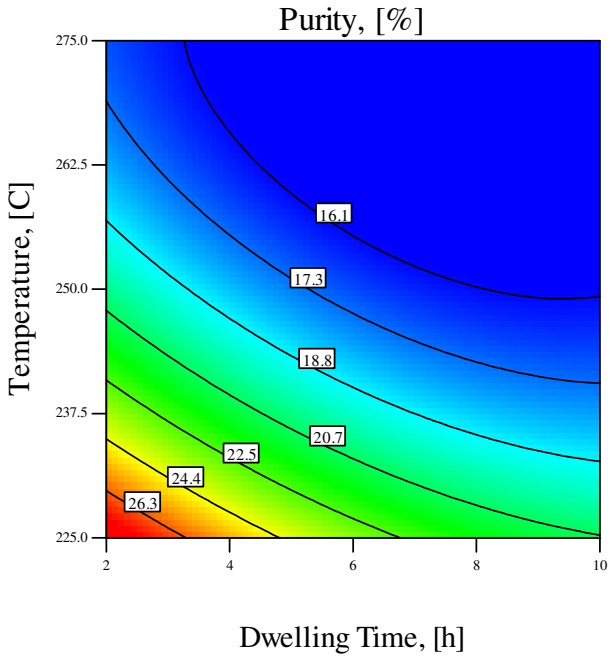

Figure 6.6 Contours plot shows the effect of temperature and dwelling time on the purity

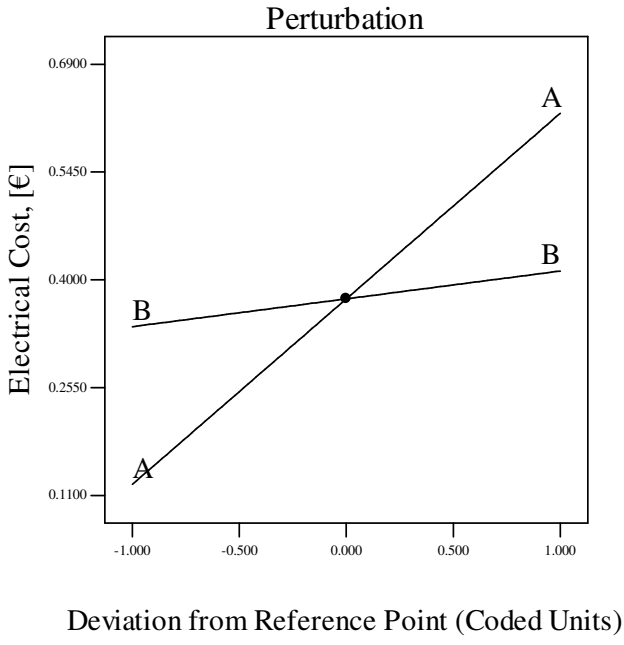

Figure 6.7 Perturbation plot shows the electrical operating cost [€] as a function of A: dwelling time, and B: temperature

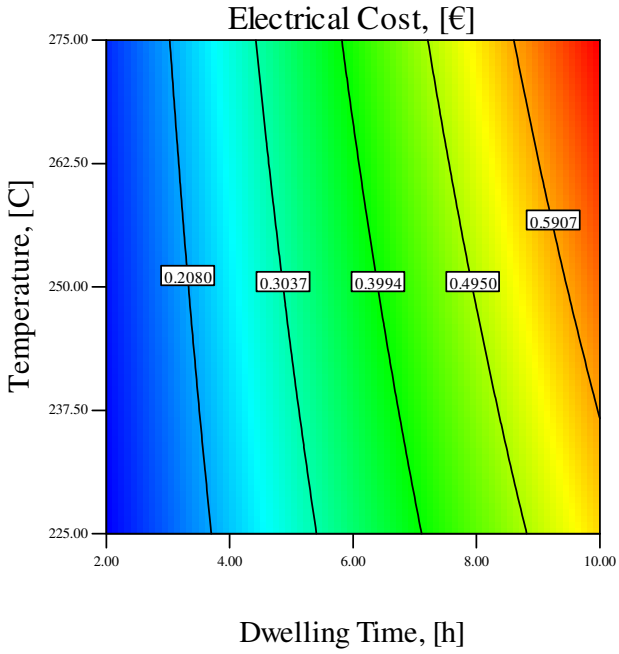

Figure 6.8 Contours plot shows the effect of temperature and dwelling time on the electrical operating cost

6.4.4 Optimisation

The possibility of combining the requirements for the purity, for the spinel crystalline structure, for the minimum growth in particle size and for the minimum the electrical operating cost must be considered since it has been shown that the purity can be achieved under a number of different sets of conditions. Achieving some of these requirements may have a negative effect on other requirements. For instance, raising the temperature is needed to oxidise the chelating agent completely and to achieve the purity, but it also, inevitably, accelerates the growth rate of particle size, particularly with prolonged dwell times. Also, time is important in order to form the spinel structure, but it also results in more electrical consumption and consequently in an increase in the electrical operating cost. On balance, and based on the above discussion, it is vital to carry out a further optimisation technique to discover the heat treatment condition at which all requirements would be satisfied, or satisfied as much as possible.

In practice, using the software, once the mathematical models have been developed and checked for adequacy, the optimisation criteria can be set to determine the optimum heat treatment conditions. In this part of the investigation two criteria were

selected for implementation to achieve high purity taking into consideration the formation of the spinel structure and the avoidance of any unnecessary growth in particle size in addition to the reduction in electrical consumption. Table 6-6 summarises the optimisation criteria used at this point in the study.

Table 6-6 Optimisation criteria used in this study

Parameter or Response	Limits		Importance	First criterion	Second criterion
	Lower	Upper			
Time	2	10	3	is in range	is in range
Temp.	225	275	3	minimise	is in range
Purity	16.034	27.426	5	minimise	minimise
Electricity operating cost	0.11232	0.6864	3	is in range	minimise

The first criterion was selected to achieve the minimum "purity" (that is the minimum level of impurities, which is the highest real purity) employing the minimum temperature needed for the chemical reactions, with no limitation on either the dwell time or the electrical operating cost. In the second criterion, the goal was to achieve the minimum "purity" at the minimum electrical operating cost with no limitation on either the temperature or dwell time of the heat treatment. Table 6-7 and Table 6-8 present the optimal solutions based on the two optimisation criteria as determined by Design-Expert V7.

Table 6-7 Optimal solution as obtained by Design-Expert based on the first criterion

Number	Time, h	Temp., °C	Purity, %	Electricity operating cost, €	Desirability
1	9.28	249.97	16.034	0.579	0.771

Table 6-8 Optimal solution as obtained by Design-Expert based on the second criterion

Number	Time, h	Temp., °C	Purity, %	Electricity operating cost, €	Desirability
1	3.43	275	16.034	0.235	0.913

In this exercise in optimisation, the criteria were selected so that, whatever else might have been involved in each criterion, the aim must always be that the minimum "purity" must be achieved. Table 6-7 shows the optimal heat treatment conditions according to the first criterion. These conditions give the lowest temperature necessary to fully oxidise the organic contents. However, due to the prolonged dwell time, the

electrical operating cost is considered to be high, at about 0.58 €, for an operation on a small batch of powder. On the other hand, if the electrical operating cost is to be reduced much further with the same level of purity, the temperature has to be increased to its highest value within the range, as the results in Table 6-8 show. In this case, the electrical operating cost has a value of about 0.24 € per batch. Thus, by adopting the second criterion, the required purity can still be achieved, with a 60% reduction in the electrical operating cost when compared with the costs associated with the first criterion.

Under certain circumstances, a visual approach to this type of optimisation problem may be useful. It is achieved by using a diagram called an overlay plot. This type of plot is immensely practical, and can be used to reach an immediate technical assessment, to explore the results of choosing values for process parameters that would achieve certain responses. Figure 6.9 and Figure 6.10 show the overlay plots based on the optimal solutions stated in Table 6-7 and Table 6-8. The green region on the plot refers to the area which is close to the solution or close to meeting the proposed criteria.

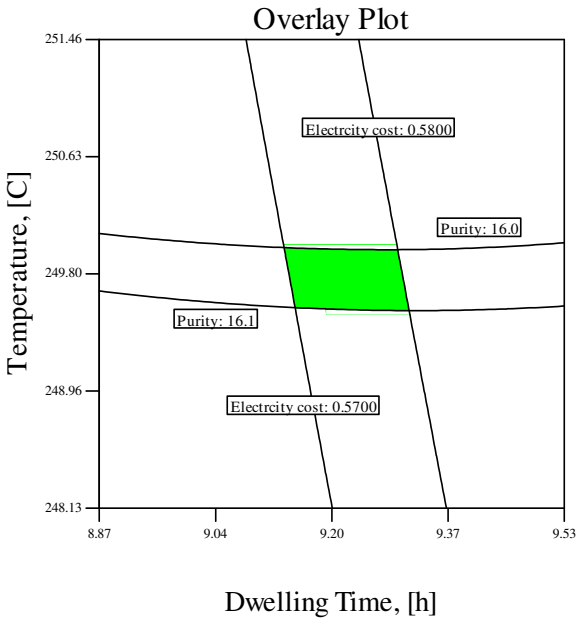

Figure 6.9 Overlay plot shows the region of optimal heat treatment condition based on the first criterion

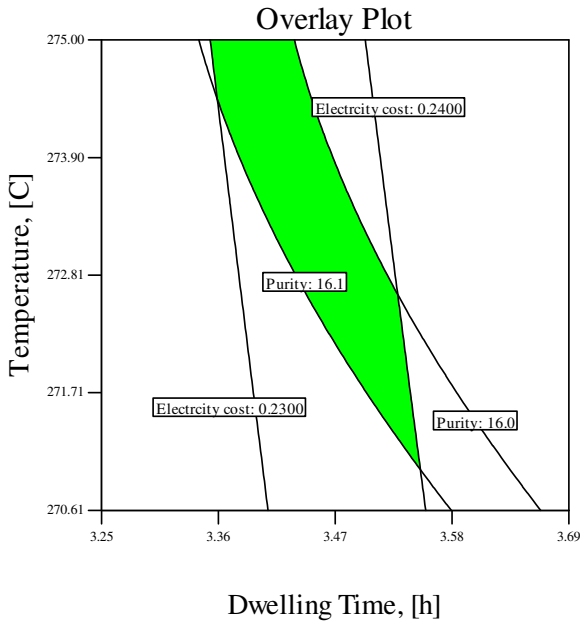

Figure 6.10 Overlay plot shows the region of optimal heat treatment condition based on the second criterion

6.4.5 The structural characterisation of the optimised sample

A new experimental trial was then carried out on a sample of the same amorphous powder, adopting the optimum heat treatment parameters shown in Table 6-8. Afterwards, the purity of the cobalt ferrite nanoparticles produced in this trial was estimated and it was found to match the predicted value. This indicates that the elimination of the organic contents and other impurities was achieved by oxidation and/or decomposition. To investigate the structure, an XRD pattern was obtained, and to illustrate the particle size distribution, an FE-SEM image was taken.

The XRD pattern of cobalt ferrite nanoparticles is shown in Figure 6.11. All the peaks related to the $CoFe_2O_4$ phase are visible providing evidence for the formation of the spinel structure. No additional peaks are visible. This indicates that the only crystalline phase present is the cobalt ferrite spinel structure. The XRD pattern matches the JCPDS-ICDD file number 22-1086.

The particle size distribution is illustrated in Figure 6.12. The particles exhibit a polydisperse distribution with the particle sizes ranging from 5 to 25 nm. The nanoparticles appear to be almost spherical. No agglomerations are visible. As a result,

a significant lowering in the sizes of the particles can be seen when compared with the results reported in previous chapters in this study.

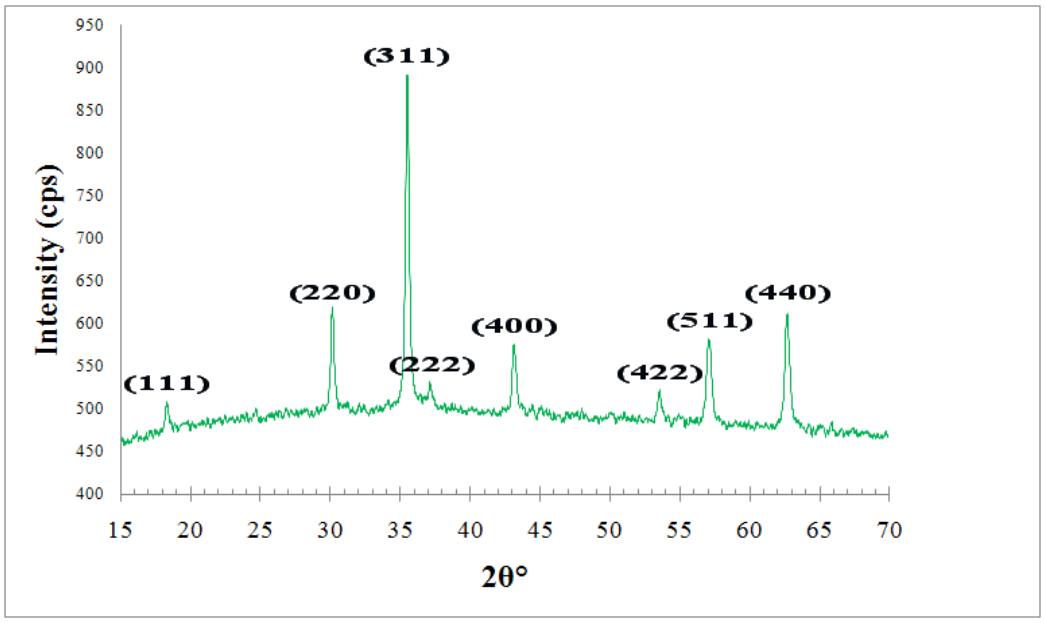

Figure 6.11 XRD pattern of cobalt ferrite nanoparticles obtained employing the optimal solution

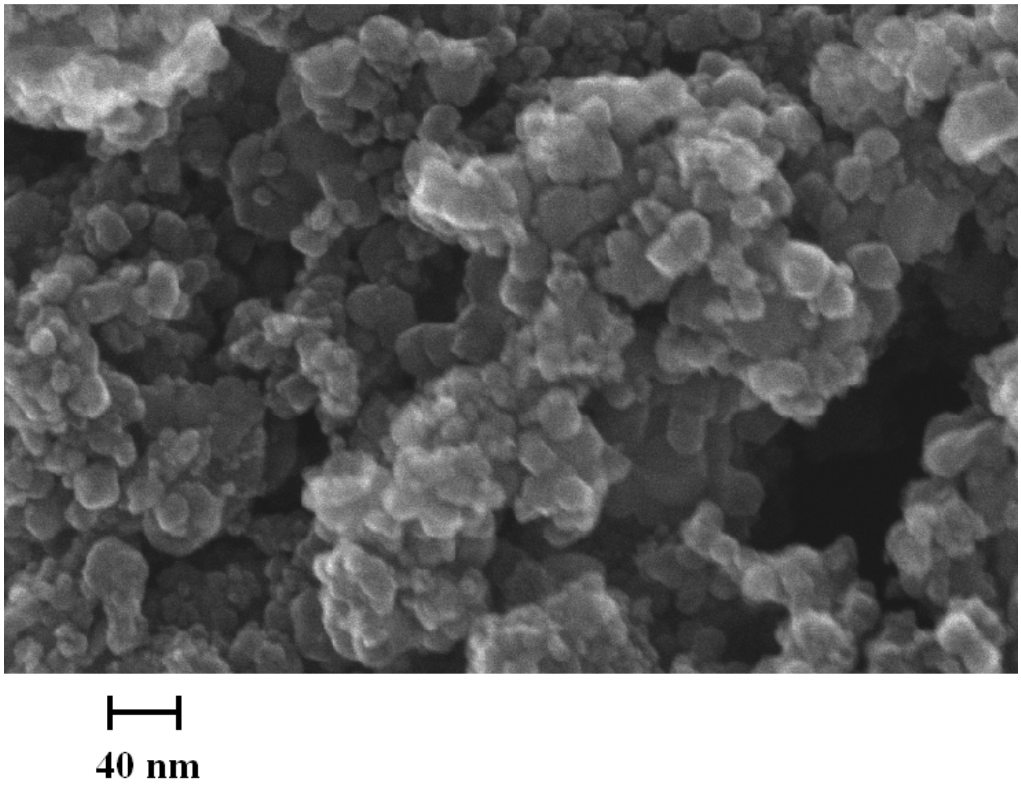

Figure 6.12 FE-SEM image of cobalt ferrite nanoparticles obtained employing the optimal solution

6.5 Summary

The sol–gel technique was adopted again to prepare fresh samples of cobalt ferrite, $CoFe_2O_4$, nanoparticles using cobalt and iron nitrates as precursors and citric acid as the chelating agent. The heat treatment operation was repeated experimentally following a planned arrangement of different parameter settings. The results of this series of trials enabled the heat treatment operation to be modelled using mathematical equations. The operation was then optimised by means of RSM in order to obtain the cobalt ferrite structure without any residual impurities. The temperature was found to be a parameter with the greatest influence with respect to both the purity and the electrical cost, and its interaction with the dwell time was investigated. An experimental trial was then conducted, for verification purposes, using parameters selected at random and the trial results matched the predictions given by the design software. It was discovered that a number of different sets of conditions, determined by the software programme, can be adopted to make the cobalt ferrite nanoparticles free of impurities. It was then possible to use the software programme to achieve three distinct aims simultaneously. These were to obtain the cobalt ferrite structure without any residual impurities, to avoid any unnecessary growth in the sizes of the particles and to reduce the electrical operating cost of the operation. The set of conditions that was finally selected, was the set in which the temperature was 275 °C and the dwell time was 3.4 h. Data was also made available in the form of charts which can be used for an immediate search about the optimal heat treatment settings and provide a good visual understanding of the optimisation. An experimental trial was then conducted using these parameters and it resulted in the formation of the spinel structure with no impurities. This was deduced firstly because the "purity" variable was found to match the predicted value of 16.034% referred to in Table 6-8 which indicates that all impurities had been removed. Secondly evidence that the spinel structure was that of cobalt ferrite and that there were no other phases present, was made available using XRD equipment. The particle size distribution was measured by SEM and was found to be in the range between 5 and 25 nm. The electrical operating cost was calculated to be €0.24 for the heat treatment operation on a small batch of powder and the parameters were selected to minimise this cost. The required purity can be obtained by employing either of the two solutions shown in Table 6-7 and Table 6-8. However, when the optimal solution indicated in Table 6-8 is

adopted, the heat treatment electrical operating cost would be reduced by approximately 60% in comparison with the costs associated when adopting the optimal solution shown in Table 6-7.

Chapter 7

The sintering behaviour of the nanoparticles

7 The sintering behaviour of the nanoparticles

7.1 Introduction

Cobalt ferrite powder was prepared using a standard solid-state reaction route by Rafferty et al. [6]. This original powder was initially sieved to produce a quantity of particles whose diameters were all smaller than 150 μm. The average particle size of the sieved powder was measured and it was found to be 14.17 μm. This sieved powder was then uniaxially pressed into disc samples and the discs were sintered under conditions with a single, continuous, ramp rate, bringing the temperature from room temperature to the sintering temperature and then with a single dwell time at the sintering temperature. The green density of the discs was measured, and expressing the result as a relative density with respect to the theoretical density of cobalt ferrite, it was found to be about 56%. A series of experimental trials was carried out by varying the sintering temperature in the range between 1200 and 1500 °C. After each trial the density of the discs was measured, and the maximum value of the density was found to be 87.51%, occurring in a disc which had been sintered at 1450 °C with a dwell time of 3 h. Further quantities of the sieved cobalt ferrite powder, with an average particle size of 14.17 μm, were then placed in an attrition mill, to produce smaller particles. The resulting powder, with 5.34 μm as the average particle size, had a specific surface area of 0.7381 m^2/g measured using the BET method. Using a dilatometer, it could be seen that the rate of

shrinkage was faster than that of the powder with 14.17 μm as the average particle size. In this case the total linear shrinkage was approximately 15%. The attrition mill was used again to prepare another small sample of the cobalt ferrite powder. This time the action of the mill was continued for much longer, and so the particle size of the powder was reduced more. When it was completed the particle size distribution was measured and the average particle size was found to be 2.37 μm. It was now possible to perform a comparative experiment. Three disc samples were made, each from a powder with a different particle size distribution, giving average particle sizes of 14.17, 5.34 and 2.37 μm. They were each sintered at 1450 °C for 3 h. Afterwards, the densities of the discs were measured. This was done using the "geometrical approach" in which the thickness and diameters of each disc was measured to provide an estimate of the volume and then by weighing each disc an estimate of the density could be made. The density of the disc made from the 5.34 μm powder was found to be greater than that made from the 14.17 μm powder by 4%. No further increase in density was observed when the particle size was further reduced to 2.37 μm.

After the comparative experiment described above the final densities of the discs were also measured by a different technique using Pycnometry. Because this technique uses helium gas which is able to penetrate into some of the pores in the discs, it provides a different value for the density. The reason why all these samples have densities which are less than the theoretical density of cobalt ferrite is because they contain pores which may be filled with air, but may also contain the residues left behind by organic binders and other chemicals, which have not been completely decomposed or oxidised. When pores exist in a sample, the density is less than the theoretical value and the relative density is less than 100%. Some of the pores are open, in which case they are close to the surface of the sample, or they are connected by passageways to the outside surface of the sample. Other pores are closed because they exist below the surface of the sample and there are no passageways connecting them to the outside surface. The materials inside them have become trapped inside the sample. If all the pores in a sample are open pores, the helium pycnometer density measurement gives the same value as the true density of the material. This occurs in a sample of powder before it is pressed into a shape such as a disc. However, during the sintering operation, some of the interconnecting passageways become blocked and so closed pores are created. When this happens the Pycnometry results give values for the relative density which are less

than 100%. The pycnometer therefore provides a measurement for the closed porosity on its own. The method of measuring the density using the geometrical approach gives a value which provides information on all pores, whether open or closed. Therefore an estimate for the amount of open pores can be made by subtracting one density value from the other.

With this alternative method for measuring density it was possible to provide estimates for the open porosity and the closed porosity for the disc made from cobalt ferrite with an average particle size of 14.17 μm. These are 2.94% and 9.95% respectively. The last result provides a reason why the sintering operation carried out on discs made using this powder was unable to achieve densities close to the theoretical value. Once the pores have changed from open to closed, it is not possible to reverse the change and so the gases or other materials trapped in the pores are trapped permanently. It is thought that a phenomenon must have occurred resulting in rapid grain growth, which surrounded the pores, causing them to become closed and leading to pore entrapment. It is also possible that the temperature inside the discs was lower than the temperature on the disc surface during sintering. This is because of the poor thermal conductivity of the material, and the fact that most of the heat is transferred to the surfaces of the disc by conduction and convection. Therefore the sintering activity would occur earlier at the surfaces of the disc than it would towards the centre of the disc. During the sintering most of the pores are eliminated, and therefore passageways connecting the pores deep inside the sample with the surface would become blocked near the surfaces, causing the pores deeper inside the disc to become closed. It is therefore important to control the sintering conditions so that the interconnecting passageways in the material do not become blocked changing the pores which are a long way from the surface from being open to closed, until most of the sintering has been completed throughout the whole of the sample.

The situation was different when working with the powders with smaller particle sizes. For instance, the open porosity of the 2.37 μm sample was found to be 5.27% while the closed porosity was 3.32%. Because the majority of pores in this last sample were still open during, and after, the sintering, it is possible to conclude that the low density result after sintering could not be due to the fact that the open, interconnected

pores had already been eliminated. In fact, in this case, decreasing the particle size does not confer any advantage in causing an increase in density.

After pressing the powder to form discs, and before the sintering operation, it was possible to cut these discs with a knife in such a way that a sample could be made which could fit into the dilatometer. In this way information about the shrinkage of the material could be generated. The differential of the shrinkage data can be calculated to indicate the rate of shrinkage, and when these curves for each of the powders are plotted from dilatometer data, it can be seen that the densification rate peak for the powders occurs at different temperatures. It is 1260 °C for the 2.37 μm powder. It increases to 1310 °C for the 5.34 μm powder. This is the temperature when the gases in the open pores are being expelled at the greatest rate, allowing the solid to contract under the influence of surface tension. However, when the sintering was carried out at higher temperatures e.g. 1450 °C which was the temperature set during the dwell time in these experimental trials, the temperature is already too high and there is a danger that some of the pores may become blocked at a stage which is too early in the operation. Therefore the higher temperature is not optimal in terms of achieving a maximum value of density. The critical densification stage was in effect being bypassed.

Therefore a two-step sintering profile was devised for the 5.34 μm powder based on data from the differential shrinkage curve. It consisted in an initial ramp to a temperature of 1310 °C, then a dwell time of 3 h at this temperature, then a second ramp rate of 20 °C/min to 1450 °C, followed by a second dwell of 30 min hold at 1450 °C. This was followed by cooling at 5 °C/min to room temperature. During the final stage of sintering, it was hoped that all of the porosity would be eliminated. However this could only occur if all pores were connected to fast, short diffusion paths which would be located presumably along grain boundaries. For this to happen, the contents of any pores would have to follow the passageways along grain boundaries. If exaggerated grain growth occurs, grain boundaries can quickly disappear, and then pores become trapped inside large grains. If this happens the pores would be very difficult to remove because the paths would be long and slow.

In order to test this sintering profile, discs were pressed using the 5.34 μm powder and sintered following the optimised profile. A final relative density of about 95% was achieved. This value was a significant improvement in comparison with the

value of 91.62% recorded for the equivalent sintered discs employing the one-step sintering profile. It was considered that this improvement was sufficient to justify the two-step profile approach to sintering and the explanation about open pores becoming closed because the temperature was raised to a high value at a stage in the operation which was too early.

As a result of this success the same sintering profile was selected for sintering rods of cobalt ferrite. These rods measured 1 cm diameter by 10 cm long. They were therefore very much larger than the discs which had been used previously. They were required for testing the magnetic properties of cobalt ferrite, but being so much larger it was recognised that all the problems involved in the sintering activity would be magnified. For instance the low thermal conductivity would cause a much larger difference in temperature between different parts of the sample, the connecting pathways from deep inside the sample to the surface would be much longer, it would be more difficult to remove the organic agents used as binders, and finally being much larger there would be a tendency for cracking to occur. Also because of the size of the rod, it was considered impractical to attempt to use an attrition mill to generate the powder with an average particle size of 2.37 μm. The rods were cold isostatically pressed using the 5.34 μ m powder at a pressure of 185 MPa. After sintering the density was measured using the geometrical approach, and the result was a relative density of 91.16%. In view of the extra difficulties in the sintering of so large a sample, this result was considered as very satisfactory. One explanation for the fact that the relative density was not as high as that obtained when working with discs was the less efficient removal of the PVA binder from the larger sample, leading to trapped pores. Of concern was the high percentage of closed pores 8.13%. This was attributed to trapped binder, exaggerated grain growth, or a combination of the two.

The aim of the experimental work reported in this chapter was to study the behaviour of cobalt ferrite nanoparticles during sintering in order to eliminate the open porosity and produce samples with a density closer to the theoretical density value. Cobalt ferrite nanoparticles were prepared employing the sol–gel technique. The structure and morphology of these nanoparticles had been already investigated. The density of the nanoparticles was measured using a pycnometer. These nanoparticles were uniaxially pressed into disc samples and sintered under conditions involving a

single, continuous ramp rate and a single dwell time. It was proposed that a correlation would be investigated between the sintering temperature and the densities of the resulting sintered disc samples. The density of disc samples was measured employing the geometrical method, a method using Archimedes Principle and a helium Pycnometer. The difference between the various methods can be used to quantify the percentages of open and closed pores inside the sintered compacts.

7.2 Experimental procedure

7.2.1 Nanoparticles preparation

Cobalt ferrite nanoparticles were uniaxially pressed into disc samples. These nanoparticles had been prepared beforehand employing the sol–gel technique. This is based on the formation of a stable and homogenous sol obtained through the hydrolysis and condensation reactions. The reactions take place between water, citric acid and a mixture of Cobalt (II) nitrate hexahydrate, (Co(NO3)2.6H2O, ≥99%, Fluka) and Iron (III) nitrate nonahydrate, (Fe(NO3)3.9H2O, ≥98%, Sigma-Aldrich) as shown in Figure 7.1. The precursors were used without any further refinement with a molecular ratio of Co to Fe equal to 1:2.The amount of citric acid was stoichiometrically double with respect to the sum of the two metal ions.

The sol was then dried, placed in alumina crucibles (Almath Ltd., UK) and exposed to a heat treatment operation in a horizontal tube furnace (Carbolite, Sheffield, UK) at 275 °C for 3.4 h in flowing dry air to form the crystalline $CoFe_2O_4$ nanoparticles. Using a mixer and hotplate, a solution containing 3wt% of PVA and 3wt% of glycerine was formed by dissolving them in distilled water. The cobalt ferrite nanoparticles were then blended into this solution and mixed thoroughly. The mixture was placed on evaporating dishes, dried at 105 °C and ground using a mortar and pestle.

7.2.2 Disc samples forming and sintering

Disc samples were formed by uniaxially pressing 3.0 g of nanoparticles in a 20 mm diameter steel die. A load of 20 kg/cm^2, approximately equal to 20 bar, was applied for a duration of 20 s. These disc samples, which were then loaded on to alumina tiles, were sintered under conditions involving a single, continuous, ramp rate and a single dwell time. The binder burnout was carried out first, with a heating up ramp rate of 0.2

°C/min to 550 °C. The temperature was then maintained at 550°C for 1 h, and then the furnace was cooled to room temperature, initially at a rate of 5 °C/min. A dwell time for the sintering of 3 h was employed. The heating up rate was 10 °C/min while the initial cooling down rate was controlled at 5 °C/min.

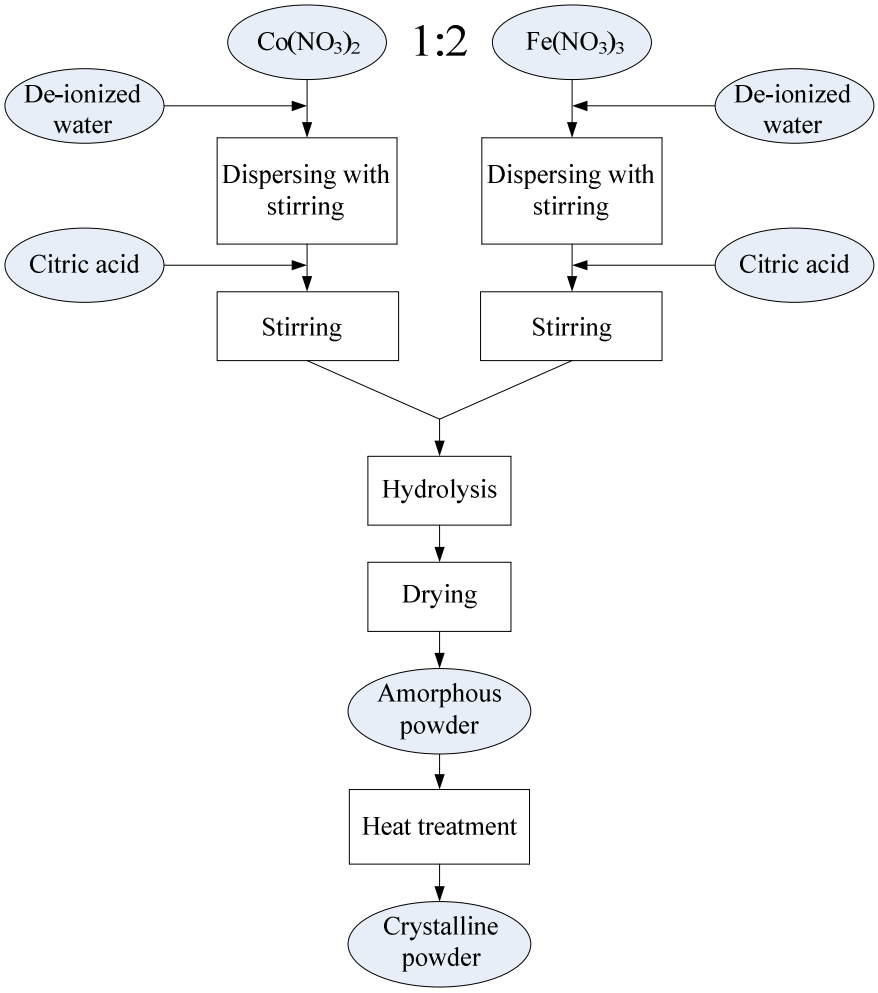

Figure 7.1 Nanoparticles preparation

7.2.3 Density measurements

The density of each sintered disc sample was estimated by the geometric method. The discs being cylindrical, the density was calculated on the basis of length and mass measurements, using vernier calipers (with an accuracy of 0.01 mm) and a precision balance (with an accuracy of 0.0001 g), respectively. An average thickness was determined from four measurements. Values for the diameter were calculated, being also the average of four measurements. A method using Archimedes' Principle was also employed to measure the density of the disc samples and a helium Pycnometer

was used to provide information on the closed pores. Using all these methods, it was possible to determine the percentages of open and closed porosity.

7.3 Results and discussion

7.3.1 Morphology of nanoparticles

The preparation of cobalt ferrite nanoparticles employing the sol–gel technique has been described in the previous chapters. The XRD pattern of the nanoparticles prepared for this study is shown in Figure 7.2. All the peaks relating to the cobalt ferrite structure are visible. No additional peaks can be seen providing evidence for the formation of pure cobalt ferrite without any impurities. This pattern matches the JCPDS-ICDD file number 22-1086.

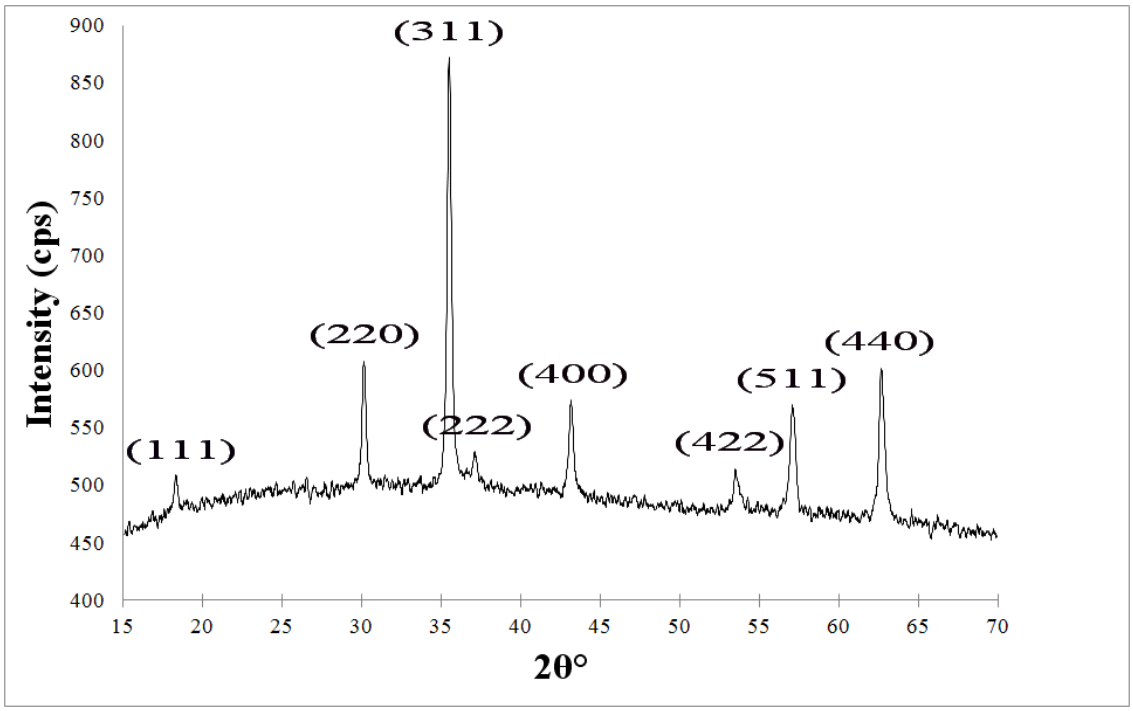

Figure 7.2 XRD pattern of obtained nanoparticles

The particle sizes are illustrated in Figure 7.3. These nanoparticles have a size range between 5 and 25 nm (demonstrating the nano nature of resultant powder).

7.3.2 Sintering of nanoparticles

A density of 5.24 g/cm^3 was measured by Rafferty et al. for cobalt ferrite powder using a helium gas Pycnometer [6] and this has been used as the basis for

calculating the relative densities of samples in the present investigation. The cobalt ferrite nanoparticles prepared for this study were uniaxially pressed and sintered under conditions involving a single continuous ramp rate and a single dwell time. The green density of the pressed discs was calculated to be 38.97±1.88%. A series of sintering trials was conducted on these discs. The sintering temperature was varied for each member of the series from 1200 to 1500 °C with intervals of 50 °C. Details of the different sintering conditions with the final densities of the samples are presented in Table 7-1. For each set of conditions, three disc samples were sintered. This resulted in three measurements being made for each of the three ways of estimating the density for each set of conditions. Each density value presented in this table for the disc samples is the arithmetic mean of three measurements and the standard deviations are also given.

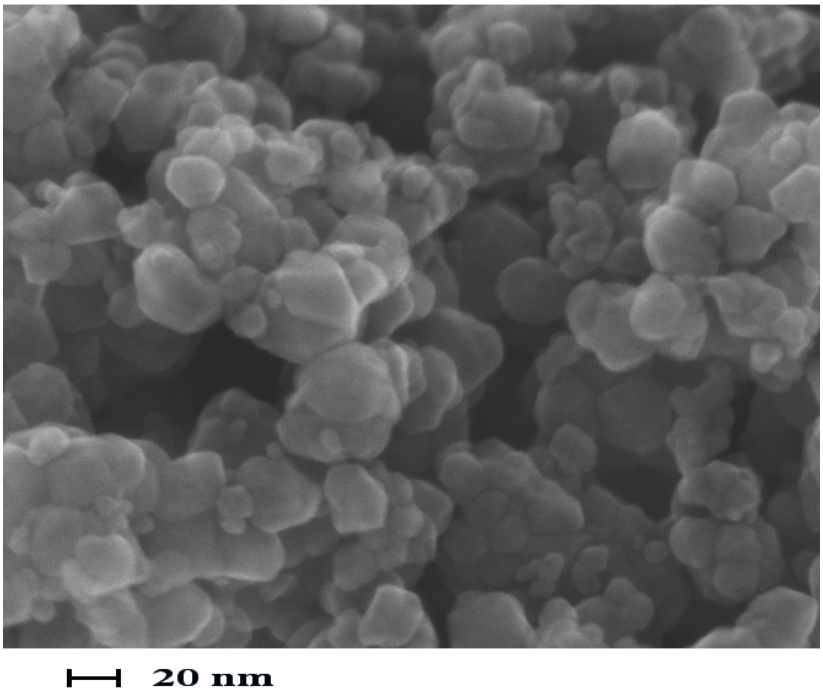

Figure 7.3 Particle size and its distribution

The density is found generally to be higher when the sintering temperature is higher until a maximum value is reached. After this, with further increases in the sintering temperature, the density becomes smaller, as shown in Figure 7.4. A maximum value for the density using the Archimedes method of 96.16±0.20% was reached at 1350 °C. The Pycnometry data yielded a value of 96.62±0.48% at the same sintering temperature. Employing sintering dwell times which were shorter, or longer, than the 3 hours, at 1350 °C, did not result in any increase in the final density of the disc samples,

as shown in Figure 7.5. A small number of disc samples were prepared using different applied pressures during the pressing. These different pressures were 15 and 25 kg/cm^3, one being higher, and one being lower, than the pressure normally used in this study. However no increase in the final density was observed after making these changes in the applied pressure used when pressing, as shown in Figure 7.6. The percentages of the open and closed porosities of the prepared disc samples are shown in Table 7-2. The data suggest that there were a small percentage of closed pores remaining in the disc samples after sintering. The amount of closed porosity seems to have decreased at first as the sintering temperature increased. It then reached a minimum value at 1350 °C, and then it started to increase again as the sintering temperature was raised to higher values. In contrast with this, the percentage of open porosity was found to be very small, especially when sintering at 1350 °C. This provides evidence that the sintering operation was successful in reducing some of the open porosity in these disc samples.

Table 7-1 The sintered discs with their respective conditions and densities

Sample	Temperature [°C]	Geometrical Density [%]	Archimedes Density [%]	Pycnometer Density [%]
1	1200	94.36±0.17	94.90±0.10	95.43±0.28
2	1250	94.91±0.18	95.25±0.15	95.59±0.37
3	1300	95.24±0.21	95.67±0.20	96.10±0.50
4	1350	95.71±0.25	96.16±0.20	96.62±0.48
5	1400	94.27±0.52	95.13±0.17	96.00±0.96
6	1450	94.01±0.22	95.00±0.15	95.99±1.12
7	1500	93.19±0.50	93.97±0.23	94.75±1.52

The stages of sintering are often placed into four different categories according to the microstructural changes that are taking place. The stages are (1) from contacting particles to neck growth, (2) pore coalescence and finally (3) pore shrinkage and (4) grain growth. During each stage the microstructural features change progressively in terms of neck size, pore size and grain size. During the sintering process, both neck growth and pore shrinkage reduce the distance between particles, and therefore theoretically both should increase the sample's density and shrinkage.

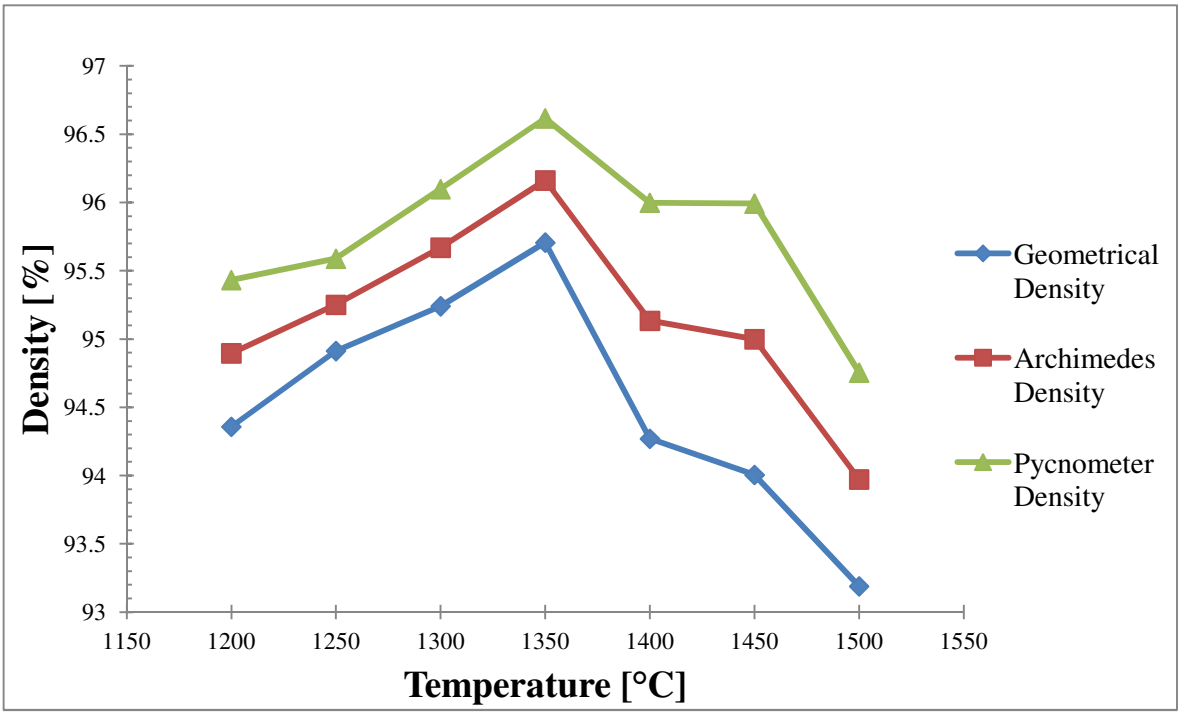

Figure 7.4 Densities as function of temperature

Agglomeration often occurs where nanoparticles exist. Agglomeration can be defined as a feature which occurs when small particles come together to form a group in such a way that the surfaces of the particles are held together by a bonding which makes the structure permanent, or semi-permanent. During the initial stage of sintering, the groups of small particles demarcated by grain boundaries coalesce to form larger aggregates with pore boundaries as shown in Figure 7.7. This results in a non uniform microstructure and may lead to non uniform densification during sintering. Hence, the concept of the fastest diffusion route during sintering becomes complicated as intra agglomerate pores may densify by grain boundary diffusion while the larger pores may require higher energies for densification. The mechanism seems to be strongly controlled by surface diffusion at low temperatures leading to neck growth and grain rotation. At higher temperatures, rapid grain boundary diffusion by overheating along inter particle boundaries may be a governing sintering mechanism [128].

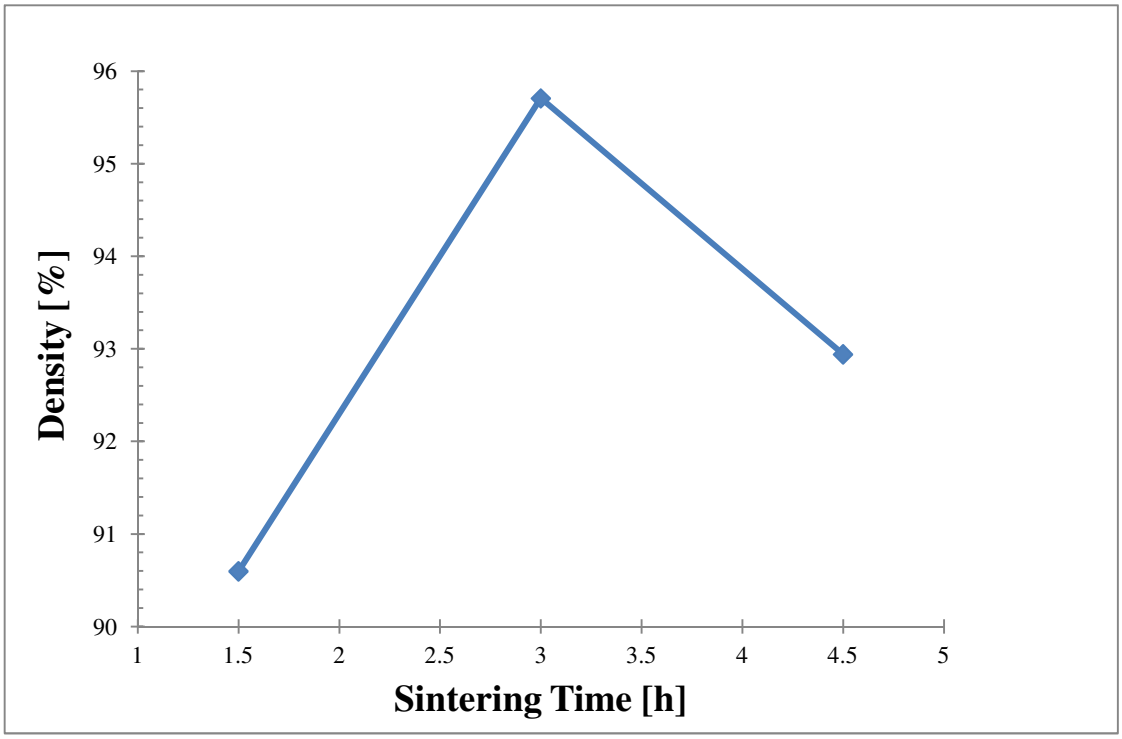

Figure 7.5 Density at 1350 °C as a function of sintering time

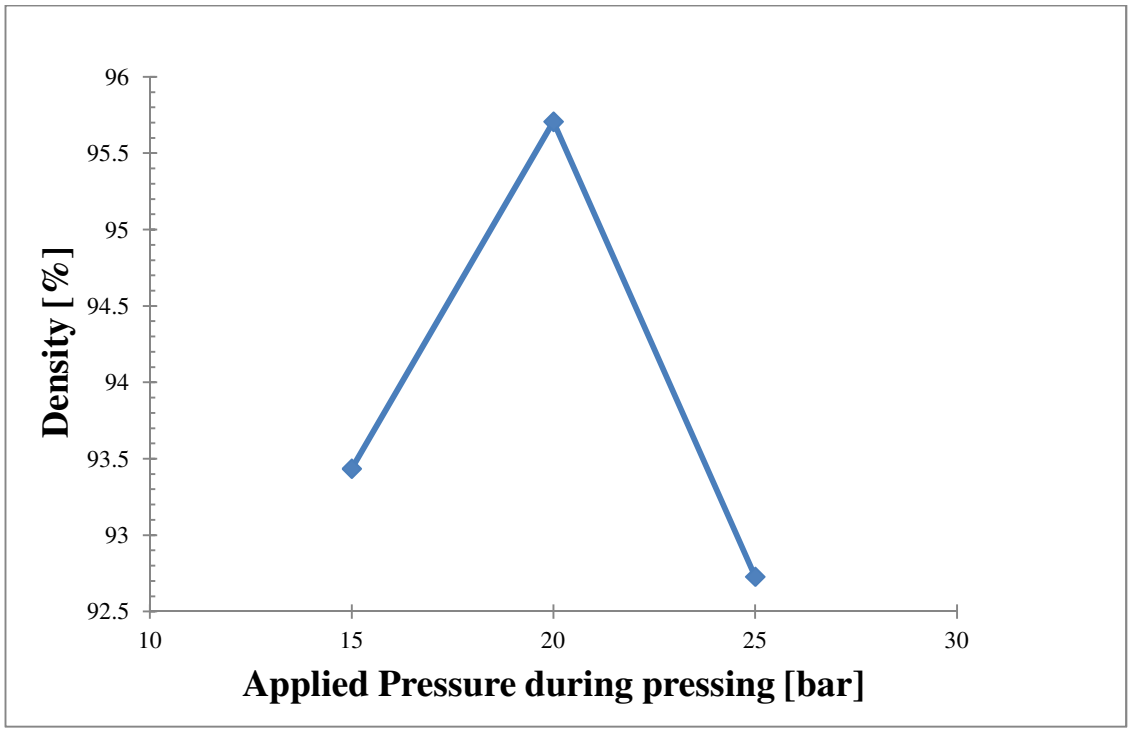

Figure 7.6 Density at 1350 °C as a function of the applied pressure during pressing

The mass transport mechanism in the initial stage of densification of nano-crystalline In_2O_3 was proposed to be grain boundary diffusion. In order for this mechanism to be active, grain boundaries must have been formed by necking during

heating [144]. It cannot be true therefore that grain boundary diffusion is the first transport mechanism. It is common for many ceramic systems to go through regimes where surface diffusion is the most important transport mechanism in the initial stages. This leads to the formation of grain boundaries, and then grain boundary diffusion becomes the most important transport mechanism as the temperature rises. Both of these mechanisms cause densification and the second one also causes grain growth [145].

Table 7-2 Open and closed porosity

Sample	Temperature [°C]	Open Porosity [%]	Closed Porosity [%]
1	1200	1.07	4.57
2	1250	0.68	4.41
3	1300	0.86	3.90
4	1350	0.91	3.38
5	1400	1.73	4.00
6	1450	1.99	4.01
7	1500	1.56	5.25

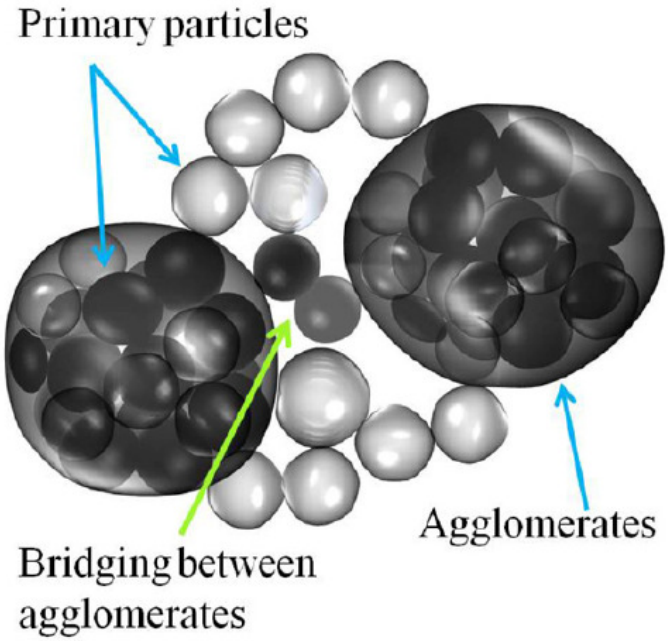

Figure 7.7 Schematic of WC microstructure during the initial stage of sintering [128]

As it has been observed, the density of disc samples increased as the temperature increased from 1200 to 1350 °C. It reached a maximum value at 1350°C while it decreased as the temperature was increased further towards 1500 °C. These changes could be due to the following factors. A significant amount of grain growth accompanied by pore entrapment is believed to happen at higher sintering temperatures. On the other hand, grain boundary diffusion is thought to be relatively small at lower sintering temperatures. Therefore this mechanism did not contribute to the densification activity to the same extent at lower temperatures. This caused the densification rate to be smaller at lower temperatures and as a consequence the discs remained more porous.

The results obtained when the dwell time was shortened to less than the 3 hours are relatively easy to explain. Clearly a shorter dwell time was not long enough for the sintering to be completed, and, as a result, the porosity was not eliminated. This can be concluded because, when the dwell time was extended to 3 hours, more of the porosity was eliminated during the sintering, evidence for which is provided by the higher values of the final density of the discs which were sintered for 3 hours. However, the results obtained when the dwell time was extended beyond the 3 hours are not so easy to explain. The longer dwell times also had a negative effect on the sintering. It might have caused a de-sintering process to take place. As pores can become smaller during the different stages of sintering, they can also become larger (e.g. link together) when, for instance, the neck and grain boundary between any two grains disappear. This phenomenon is described as de-sintering. It is generally, but not exclusively, associated with grain growth. This results in the pores to increase in size and become trapped.

The following remarks have been made in an attempt to seek explanations for the results of the experiments on varying the pressure applied when pressing. It is probably true that adopting a lower applied pressure during pressing would have resulted in unusually weak discs. The pressure was required to bring the nanoparticles sufficiently close to each other so that the organic binders on their surfaces could act as glues, holding the particles together, and preserving the shape of the disc. However it is also probably true that most of the deformation of the pressure compact, occurring in response to the applied pressure, caused the particles to move relative to one another, and this would have reduced the pore volume in the pressure compact. Also because the particles were not totally spherical in shape there would have been a tendency for the

stresses produced by the hydraulic equipment to be magnified at certain points, and on occasions this would have resulted developing in fractures in the particles. This would happen more regularly if the particles had sharp points or jagged edges. Because of this feature, there would have also been a reduction in the volume of the compact and the porosity would have been also reduced. On a smaller scale there would have also been a deformation of the organic binder layers existing as a coating on each of the surfaces of the nanoparticles. Therefore the decrease in the pore volume in the pressure compact which would have occurred as a result of increasing the magnitude of the applied pressure might be significant. For the same reasons, if the pressure applied when the discs were being made, was unusually low, the effect on the porosity would also be significant. Therefore, it is true that the porosity in the compact would be greater if the applied pressure was smaller.

The above explanation, for the existence of variations in porosity in the pressure compacts before sintering, would be generally accepted by other investigators. However, the following results of experimental trials reported in this investigation would not have been anticipated. This is that this variation in the magnitude of the porosity, originating in the different pressures used to form the discs, has discernible results in the variations of density in samples, even after the sintering operation.

This is all the more remarkable in view of the result of the experimental trial in which a higher value of applied pressure was used for the pressing of the discs. This also resulted in a reduction of the density of the samples in measurements carried out after the sintering operation. It is difficult to find a satisfactory explanation, particularly for this second effect, namely, an above average density before sintering resulted in a below average density after the treatment. It is true that the increased pressure in the die would have created more cracks in the compact in its green state, but these cracks would occur in individual particles of the microstructure as described above. This would have produced less porosity and a greater packing density of the particles. Both of these features would be expected to facilitate the subsequent sintering operation, even though it also resulted in slightly more particles in the compact. One would therefore have expected that the sintering operation would result in improved properties.

In this context it should be noted that a test was carried out using a helium gas pycnometer, type AccuPyc 1330 V1.02, to determine the true density of a sample of the

nanoparticles. The value obtained was 4.93±0.0118 g/cm^3 which is very different from the value of 5.24 g/cm^3 reported by Rafferty et al. [6]. However, a sample of the same powder was sent outside the University laboratory for the same test to be carried out, using a different helium gas pycnometer (type AccuPycII 1340 V1.05), and a value of 4.95±0.0029 g/cm^3 was obtained. The agreement between the two pycnometers is impressive, although the value quoted by Rafferty et al. is recognised as the true value by many other workers (SEE APPENDIX E).

The reason for this disparity could be related to the nature of this particular sample of cobalt ferrite nanoparticles. This is because these particles are known to have been magnetically active, and there is evidence that the majority of them were small enough to have had only one magnetic domain. Under normal conditions, that is, at room temperature and at atmospheric pressure, there would have been a tendency for these particles to arrange themselves in such a way as to minimise the magnetostatic energy of the sample. This could be done, for instance, by allowing the particles to form large rings or hoops, with the particles joined to one another end to end around an empty space inside the ring. If temporary structures such as this formed frequently enough throughout the sample, it is possible that the result would be that the nanoparticles would tend to occupy a larger volume than if they were not magnetic. This might explain why some techniques designed to measure density might provide values which are too low. However, when the instrument measuring the density is the helium gas pycnometer, it is expected that the gas would be able to penetrate through such loose structures to the empty space inside, and would therefore provide a value for the density which would agree with the known density of the individual particles. If these ideas provide a true explanation for the disparity in the density results, it is not known why the pycnometer should not be able to penetrate to the centres of these structures. However when measuring the density of powder samples with larger particles, each particle would have many magnetic domains and consequently there would be no reason for the ring or hoop like structures to form. It follows in turn that the density measuring equipment would provide the more normal, higher, value.

A similar phenomenon was observed after the pressing stage. The calculated value of 38.97±1.88% as the green density, reported in this study for compacts made using magnetic nanoparticles, indicates that a similar effect may have occurred causing

a decrease in the density. This value is much smaller than the average value of 56% reported for compacts made from micro-sized cobalt ferrite powder. Perhaps the two effects are related, and perhaps the disparity in density observed before the powders were pressed, is preserved even after the pressing stage.

Rafferty et al. reported a smaller value of density when preparing rods which were cold isostatically pressed at 185 MPa. A value of 91.16% was reported. Rafferty et al. related the reason of this result to the less efficient removal of binder leading to trapped pores. However, it is also possible that the critical densification stage was in effect being bypassed. The data, which were used to design the two-step sintering profile, was taken from differential shrinkage curves in a test using a compact disc which had been made at a pressure of 20 kg/cm^2. However, this pressure is far smaller than the pressure used when preparing the rods, which was 185 MPa. Furthermore, it seems that powders pressed under different pressures, behave differently during sintering, and the experimental work reported in this chapter suggests strongly that this is true. If so, a disc sample compressed at 20 kg/cm^2 cannot be expected to predict the behaviour of a rod compressed at 185MPa. It follows that the differential shrinking curve cannot reliably indicate the temperature where there is a peak in the densification rate in the rod sample. Therefore, the temperature selected in the two-step sintering profile as the temperature for the first dwell time might not be the correct value. It follows that a critical densification stage during the sintering of the rod might have occurred at a temperature which was different from the first dwell time of the two-step sintering programme. Therefore perhaps the sintering programme did not give sufficient time for the densification to occur at the correct temperature and this could explain the poor result of the sintering operation on that occasion.

7.4 Summary

The sintering behaviour of cobalt ferrite nanoparticles was investigated. Cobalt ferrite nanoparticles were successfully prepared employing the sol–gel technique. These nanoparticles were without any impurities. The particle size was found to be in the range between 5 and 25 nm. Disc samples were prepared employing a uniaxial press using a pressure of 20 kg/cm^2. Sintering trails were then conducted. A maximum density of 96.16±0.20% was reached at 1350 °C. This value was obtained by an instrument based on Archimedes principle. Helium gas Pycnometry data yielded a value

of 96.62±0.48%, for the same conditions. The density did not increase to a higher value, although a number of changes were made to the period of the dwell time. Similarly no higher values of the density were obtained when the pressure used to form the disc samples was varied. The maximum density, obtained in this study, was found to be a higher value when compared with the results found in the literature when employing a one-step sintering temperature profile.

Chapter 8

Conclusions & Future work

8 Conclusions & Future work

8.1 Conclusions

It is proposed in this study that cobalt ferrite powder with particles that are small enough to have only one magnetic domain could be used to improve the magnetostrictive coefficient of cobalt ferrite. This is because these particles have the potential to resolve the problem that, in multi-domain particles, the easy axes of magnetisation are normally arranged in all directions. The particles could also have the potential to resolve the problem of reducing the porosity which remains after sintering to even lower levels.

- Cobalt ferrite powders were synthesised and characterised employing the sol–gel technique.
- A particular focus was given in the investigation to the fundamental roles of the crosslinker and the chelating agent in creating the final structure and morphology of the powders that were produced.
- The effects of the heat treatment operational parameters on the final properties of the cobalt ferrite nanoparticles were investigated.
- The minimum temperature required to prepare cobalt ferrite nanoparticles as a single phase was determined to be 250 °C, and the dwell time required at this temperature was determined to be 10 hours.

- The magnetic properties of samples of the powder were measured and demonstrated that the particles followed ferrimagnetic behaviour at room temperature, with a saturation mass magnetisation of 62emu/g.
- The heat treatment operation was simulated, and optimised, by means of RSM, in order to obtain the cobalt ferrite structure without any residual impurities, to avoid any unnecessary growth in the sizes of the particles, and to minimise the electrical operating cost of the operation.
- The optimum conditions of a heat treatment temperature of 275 °C and a dwell time of 3.4 hours resulted in the formation of the cobalt ferrite spinel structure with no impurities.
- The electrical operating cost of the heat treatment could be reduced by approximately 60% when the optimal set of parameters is employed.
- The sintering behaviour of the cobalt ferrite nanoparticles was investigated.
- A maximum density of 95.71±0.25% was reached at 1350 °C. Pycnometry data yielded a value of 96.62±0.48% for the same conditions.
- This first value for the density is an improvement over the value of 91.62% reported by other investigators, for cobalt ferrite powder with an average particle size of 5.34 μm using conditions involving a single continuous ramp rate and a single dwell time.

The following summarises these conclusions. Cobalt ferrite (single-domain) nanoparticles were successfully prepared. They were structurally and magnetically characterised. The operation of the heat treatment was simulated and optimised in order to reduce the cost of the operation. The density of a sintered disc made from these nanoparticles indicates that a noticeable improvement was achieved. This improvement is considered to contribute in the enhancement of the magnetostrictive coefficient.

8.2 Future work

Magnetostriction is influenced by magnetic and structural factors. The results of this study suggest that there are grounds for claiming that the structural factor can be improved as it is related to the final sintered density. A density for sintered compacts of around 96% was achieved employing a single continuous ramp rate and a single dwell time. With an increase in density similar to this, the magnetic properties of samples of cobalt ferrite could be improved with an increase in the magnetostriction. The magnetic

factor is related to the fact that the easy axes of magnetisation are arranged in different directions in each magnetic domain. The preparation of single-domain particles, which was carried out in this study, is a step towards a solution to this problem also.

The next step in this approach would be the development of a method to control the alignment of these particles during the pressing and sintering operations, that is to cause the alignment of the easy axes of magnetisation of these particles, so that they are parallel to each other and then, maintaining this alignment, to press these particles into a compact and sinter that compact at an elevated temperature employing the methodology presented in this study. Introducing the sintered compact afterwards into an adequate magnetic field, which must be perpendicular to the aligned easy axes of magnetisation, would deviate the magnetic moments of all the grains from the easy to the hard direction of magnetisation, causing the magnetostriction to reach its maximum value.

References

References

[1] Choadhury, H. A., 2008, "A Finite Element Approach for the Implementation of Magnetostrictive Material Terfenol-D in Automotive CNG Fuel Injection Actuation," PhD Thesis, Dublin City University, .

[2] Ekreem, N. B., 2009, "An Investigation of Electromagnetic Rig-Generated Strong Magnetic Fields," PhD Thesis, Dublin City University, .

[3] Talavera, J., Carnicero, A., Lopez, O., 2004, "Electrical current measurement based on elastic waves propagation through dielectric materials," Universities Power Engineering Conference, 2004. UPEC 2004. 39th International, IEEE, **3,** pp. 1274-1277.

[4] Grunwald, A., 2007, "Design and Optimization of Magnetostrictive Actuator," PhD Thesis, Dublin City University, .

[5] Goldman, A., 2005, "Modern ferrite technology," Springer Science Business Media, .

[6] Rafferty, A., Prescott, T., and Brabazon, D., 2008, "Sintering Behaviour of Cobalt Ferrite Ceramic," Ceramics International, **34**(1) pp. 15-21.

[7] Prescott, T., 2002, "Magnetostrictive Material Characterisation," AE1266, Cedrat Technologies S.A., .

[8] Prescott, T., 2005, "Magnetostrictive Material Characterisation," AAE1934, Cedrat Technologies S.A., .

[9] Kim, W., Yoon, S., and Kim, K., 1994, "Effects of Sintering Conditions of Sintered Ni-Zn Ferrites on Properties of Electromagnetic Wave Absorber," Materials Letters, **19**(3) pp. 149-155.

[10] Murthy, S., 2002, "Low Temperature Sintering of NiCuZn Ferrite and its Electrical, Magnetic and Elastic Properties," Journal of Materials Science Letters, **21**(8) pp. 657-660.

[11] Igarashi, H., and Okazaki, K., 1977, "Effects of Porosity and Grain Size on the Magnetic Properties of NiZn Ferrite," Journal of the American Ceramic Society, **60**(1-2) pp. 51-54.

[12] Bashkirov, S. S., Liberman, A. B., Khasanov, A. M., 1988, "Effect of the Sintering Temperature on the Crystalline and Magnetic Structure of Nickel-Zinc Ferrites (in English)," Soviet Powder Metallurgy and Metal Ceramics, **27**(5) pp. 367-370.

[13] Yan, M. F., 1981, "Microstructural Control in the Processing of Electronic Ceramics," Materials Science and Engineering, **48**(1) pp. 53-72.

[14] Kulikowski, J., and Leśniewski, A., 1980, "Properties of Ni-Zn Ferrites for Magnetic Heads: Technical Possibilities and Limitations," Journal of Magnetism and Magnetic Materials, **19**(1–3) pp. 117-119.

[15] Sawatzky, G., Van Der Woude, F., and Morrish, A., 1968, "Cation Distributions in Octahedral and Tetrahedral Sites of the Ferrimagnetic Spinel $CoFe_2O_4$," Journal of Applied Physics, **39**(2) pp. 1204-1205.

[16] Bozorth, R., Tilden, E. F., and Williams, A. J., 1955, "Anisotropy and Magnetostriction of some Ferrites," Physical Review, **99**(6) pp. 1788.

[17] Chen, Y., Snyder, J., Schwichtenberg, C., 1999, "Metal-Bonded Co-Ferrite Composites for Magnetostrictive Torque Sensor Applications," Magnetics, IEEE Transactions On, **35**(5) pp. 3652-3654.

[18] Lo, C., Ring, A., Snyder, J., 2005, "Improvement of Magnetomechanical Properties of Cobalt Ferrite by Magnetic Annealing," Magnetics, IEEE Transactions On, **41**(10) pp. 3676-3678.

[19] Paulsen, J., Ring, A., Lo, C., 2005, "Manganese-Substituted Cobalt Ferrite Magnetostrictive Materials for Magnetic Stress Sensor Applications," Journal of Applied Physics, **97**(4) pp. 044502-044502-3.

[20] Caltun, O., Dumitru, I., Feder, M., 2008, "Substituted Cobalt Ferrites for Sensors Applications," Journal of Magnetism and Magnetic Materials, **320**(20) pp. e869-e873.

[21] Caltun, O., Rao, G., Rao, K., 2007, "The Influence of Mn Doping Level on Magnetostriction Coefficient of Cobalt Ferrite," Journal of Magnetism and Magnetic Materials, **316**(2) pp. e618-e620.

[22] Melikhov, Y., Snyder, J. E., Jiles, D. C., 2006, "Temperature Dependence of Magnetic Anisotropy in Mn-Substituted Cobalt Ferrite," Journal of Applied Physics, **99**(8) pp. 08R102-08R102-3.

[23] Lo, C. C., 2007, "Compositional Dependence of the Magnetomechanical Effect in Substituted Cobalt Ferrite for Magnetoelastic Stress Sensors," Magnetics, IEEE Transactions On, **43**(6) pp. 2367-2369.

[24] Song, S., Lo, C., Lee, S., 2007, "Magnetic and Magnetoelastic Properties of Ga-Substituted Cobalt Ferrite," Journal of Applied Physics, **101**(9) pp. 09C517-09C517-3.

[25] Hou, C., Yu, H., Zhang, Q., 2010, "Preparation and Magnetic Property Analysis of Monodisperse Co–Zn Ferrite Nanospheres," Journal of Alloys and Compounds, **491**(1) pp. 431-435.

[26] Kambale, R., Shaikh, P., Harale, N., 2010, "Structural and Magnetic Properties of $Co_{1-x}Mn_xFe_2O_4$ ($0 \leq x \leq 0.4$) Spinel Ferrites Synthesized by Combustion Route," Journal of Alloys and Compounds, **490**(1) pp. 568-571.

[27] Chinnasamy, C., Senoue, M., Jeyadevan, B., 2003, "Synthesis of Size-Controlled Cobalt Ferrite Particles with High Coercivity and Squareness Ratio," Journal of Colloid and Interface Science, **263**(1) pp. 80-83.

[28] Ai, L., and Jiang, J., 2010, "Influence of Annealing Temperature on the Formation, Microstructure and Magnetic Properties of Spinel Nanocrystalline Cobalt Ferrites," Current Applied Physics, **10**(1) pp. 284-288.

[29] Kashevsky, B. E., Agabekov, V. E., Kashevsky, S. B., 2008, "Study of Cobalt Ferrite Nanosuspensions for Low-Frequency Ferromagnetic Hyperthermia," Particuology, **6**(5) pp. 322-333.

[30] Shaikh, P., Kambale, R., Rao, A., 2010, "Structural, Magnetic and Electrical Properties of Co–Ni–Mn Ferrites Synthesized by Co-Precipitation Method," Journal of Alloys and Compounds, **492**(1) pp. 590-596.

[31] Mathew, D. S., and Juang, R., 2007, "An Overview of the Structure and Magnetism of Spinel Ferrite Nanoparticles and their Synthesis in Microemulsions," Chemical Engineering Journal, **129**(1) pp. 51-65.

[32] Olabi, A., and Grunwald, A., 2008, "Design and Application of Magnetostrictive Materials," Materials & Design, **29**(2) pp. 469-483.

[33] Cedeño-Mattei, Y., and Perales-Pérez, O., 2009, "Synthesis of High-Coercivity Cobalt Ferrite Nanocrystals," Microelectronics Journal, **40**(4) pp. 673-676.

[34] Grunwald, A., and Olabi, A., 2008, "Design of a Magnetostrictive (MS) Actuator," Sensors and Actuators A: Physical, **144**(1) pp. 161-175.

[35] Kim, D., Nikles, D. E., Johnson, D. T., 2008, "Heat Generation of Aqueously Dispersed $CoFe_2O_4$ nanoparticles as Heating Agents for Magnetically Activated Drug Delivery and Hyperthermia," Journal of Magnetism and Magnetic Materials, **320**(19) pp. 2390-2396.

[36] Baldi, G., Bonacchi, D., Franchini, M. C., 2007, "Synthesis and Coating of Cobalt Ferrite Nanoparticles: A First Step Toward the Obtainment of New Magnetic Nanocarriers," Langmuir, **23**(7) pp. 4026-4028.

[37] Amiri, S., and Shokrollahi, H., 2013, "The Role of Cobalt Ferrite Magnetic Nanoparticles in Medical Science," Materials Science and Engineering: C, **33**(1) pp. 1-8.

[38] Morais, P., 2009, "Photoacoustic Spectroscopy as a Key Technique in the Investigation of Nanosized Magnetic Particles for Drug Delivery Systems," Journal of Alloys and Compounds, **483**(1) pp. 544-548.

[39] Shinkai, M., 2002, "Functional Magnetic Particles for Medical Application," Journal of Bioscience and Bioengineering, **94**(6) pp. 606-613.

[40] Ritter, J. A., Ebner, A. D., Daniel, K. D., 2004, "Application of High Gradient Magnetic Separation Principles to Magnetic Drug Targeting," Journal of Magnetism and Magnetic Materials, **280**(2) pp. 184-201.

[41] Pita, M., Abad, J. M., Vaz-Dominguez, C., 2008, "Synthesis of Cobalt Ferrite Core/Metallic Shell Nanoparticles for the Development of a Specific PNA/DNA Biosensor," Journal of Colloid and Interface Science, **321**(2) pp. 484-492.

[42] Baldi, G., Bonacchi, D., Innocenti, C., 2007, "Cobalt Ferrite Nanoparticles: The Control of the Particle Size and Surface State and their Effects on Magnetic Properties," Journal of Magnetism and Magnetic Materials, **311**(1) pp. 10-16.

[43] Wagner, J., Autenrieth, T., and Hempelmann, R., 2002, "Core Shell Particles Consisting of Cobalt Ferrite and Silica as Model Ferrofluids [$CoFe_2O_4$–SiO_2 core Shell Particles]," Journal of Magnetism and Magnetic Materials, **252**pp. 4-6.

[44] Bonini, M., Wiedenmann, A., and Baglioni, P., 2006, "Synthesis and Characterization of Magnetic Nanoparticles Coated with a Uniform Silica Shell," Materials Science and Engineering: C, **26**(5) pp. 745-750.

[45] Caillot, T., Pourroy, G., and Stuerga, D., 2004, "Microwave Hydrothermal Flash Synthesis of Nanocomposites Fe–Co Alloy/Cobalt Ferrite," Journal of Solid State Chemistry, **177**(10) pp. 3843-3848.

[46] Shi, Y., Ding, J., and Yin, H., 2000, "$CoFe_2O_4$ nanoparticles Prepared by the Mechanochemical Method," Journal of Alloys and Compounds, **308**(1) pp. 290-295.

[47] Franco Júnior, A., Celma de Oliveira Lima, Emília, Novak, M. A., 2007, "Synthesis of Nanoparticles of $Co_xFe_{(3-x)}O_4$ by Combustion Reaction Method," Journal of Magnetism and Magnetic Materials, **308**(2) pp. 198-202.

[48] Gharagozlou, M., 2009, "Synthesis, Characterization and Influence of Calcination Temperature on Magnetic Properties of Nanocrystalline Spinel Co-Ferrite Prepared by Polymeric Precursor Method," Journal of Alloys and Compounds, **486**(1) pp. 660-665.

[49] Thang, P. D., Rijnders, G., and Blank, D. H., 2005, "Spinel Cobalt Ferrite by Complexometric Synthesis," Journal of Magnetism and Magnetic Materials, **295**(3) pp. 251-256.

[50] Pillai, V., and Shah, D., 1996, "Synthesis of High-Coercivity Cobalt Ferrite Particles using Water-in-Oil Microemulsions," Journal of Magnetism and Magnetic Materials, **163**(1) pp. 243-248.

[51] Calero-DdelC, V. L., and Rinaldi, C., 2007, "Synthesis and Magnetic Characterization of Cobalt-Substituted Ferrite ($Co_xFe_{3-x}O_4$) Nanoparticles," Journal of Magnetism and Magnetic Materials, **314**(1) pp. 60-67.

[52] Meron, T., Rosenberg, Y., Lereah, Y., 2005, "Synthesis and Assembly of High-Quality Cobalt Ferrite Nanocrystals Prepared by a Modified Sol–gel Technique," Journal of Magnetism and Magnetic Materials, **292**pp. 11-16.

[53] Ajroudi, L., Villain, S., Madigou, V., 2010, "Synthesis and Microstructure of Cobalt Ferrite Nanoparticles," Journal of Crystal Growth, **312**(16) pp. 2465-2471.

[54] Hanh, N., Quy, O., Thuy, N., 2003, "Synthesis of Cobalt Ferrite Nanocrystallites by the Forced Hydrolysis Method and Investigation of their Magnetic Properties," Physica B: Condensed Matter, **327**(2) pp. 382-384.

[55] de Biasi, R., Figueiredo, A., Fernandes, A., 2007, "Synthesis of Cobalt Ferrite Nanoparticles using Combustion Waves," Solid State Communications, **144**(1) pp. 15-17.

[56] Montemayor, S. M., García-Cerda, L., and Torres-Lubián, J., 2005, "Preparation and Characterization of Cobalt Ferrite by the Polymerized Complex Method," Materials Letters, **59**(8) pp. 1056-1060.

[57] Millot, N., Le Gallet, S., Aymes, D., 2007, "Spark Plasma Sintering of Cobalt Ferrite Nanopowders Prepared by Coprecipitation and Hydrothermal Synthesis," Journal of the European Ceramic Society, **27**(2) pp. 921-926.

[58] Chen, Y., Ruan, M., Jiang, Y., 2010, "The Synthesis and Thermal Effect of $CoFe_2O_4$ nanoparticles," Journal of Alloys and Compounds, **493**(1) pp. L36-L38.

[59] Caizer, C., and Stefanescu, M., 2002, "Magnetic Characterization of Nanocrystalline Ni–Zn Ferrite Powder Prepared by the Glyoxylate Precursor Method," Journal of Physics D: Applied Physics, **35**(23) pp. 3035.

[60] Liu, X., Fu, S., Xiao, H., 2005, "Synthesis of Nanocrystalline Spinel $CoFe_2O_4$ via a Polymer-Pyrolysis Route," Physica B: Condensed Matter, **370**(1) pp. 14-21.

[61] Li, S., Liu, L., John, V. T., 2001, "Cobalt-Ferrite Nanoparticles: Correlations between Synthesis Procedures, Structural Characteristics and Magnetic Properties," Magnetics, IEEE Transactions On, **37**(4) pp. 2350-2352.

[62] Lan, N. T., Duong, N. P., and Hien, T. D., 2011, "Influences of Cobalt Substitution and Size Effects on Magnetic Properties of Coprecipitated Co–Fe Ferrite Nanoparticles," Journal of Alloys and Compounds, **509**(19) pp. 5919-5925.

[63] Rana, S., Philip, J., and Raj, B., 2010, "Micelle Based Synthesis of Cobalt Ferrite Nanoparticles and its Characterization using Fourier Transform Infrared Transmission Spectrometry and Thermogravimetry," Materials Chemistry and Physics, **124**(1) pp. 264-269.

[64] Lopez Perez, J., Lopez Quintela, M., Mira, J., 1997, "Advances in the Preparation of Magnetic Nanoparticles by the Microemulsion Method," The Journal of Physical Chemistry B, **101**(41) pp. 8045-8047.

[65] Wang, J., Deng, T., Lin, Y., 2008, "Synthesis and Characterization of $CoFe_2O_4$ magnetic Particles Prepared by Co-Precipitation Method: Effect of Mixture Procedures of Initial Solution," Journal of Alloys and Compounds, **450**(1) pp. 532-539.

[66] Li, X., and Kutal, C., 2003, "Synthesis and Characterization of Superparamagnetic $Co_xFe_{3-x}O_4$ nanoparticles," Journal of Alloys and Compounds, **349**(1) pp. 264-268.

[67] Zhao, D., Wu, X., Guan, H., 2007, "Study on Supercritical Hydrothermal Synthesis of $CoFe_2O_4$ nanoparticles," The Journal of Supercritical Fluids, **42**(2) pp. 226-233.

[68] Moumen, N., Veillet, P., and Pileni, M., 1995, "Controlled Preparation of Nanosize Cobalt Ferrite Magnetic Particles," Journal of Magnetism and Magnetic Materials, **149**(1) pp. 67-71.

[69] Olsson, R. T., Salazar-Alvarez, G., Hedenqvist, M. S., 2005, "Controlled Synthesis of Near-Stoichiometric Cobalt Ferrite Nanoparticles," Chemistry of Materials, **17**(20) pp. 5109-5118.

[70] Sorescu, M., Grabias, A., Tarabasanu-Mihaila, D., 2001, "From Magnetite to Cobalt Ferrite," Journal of Materials Synthesis and Processing, **9**(3) pp. 119-123.

[71] El-Shobaky, G., Turky, A., Mostafa, N., 2010, "Effect of Preparation Conditions on Physicochemical, Surface and Catalytic Properties of Cobalt Ferrite Prepared by Coprecipitation," Journal of Alloys and Compounds, **493**(1) pp. 415-422.

[72] El-Okr, M., Salem, M., Salim, M., 2011, "Synthesis of Cobalt Ferrite Nano-Particles and their Magnetic Characterization," Journal of Magnetism and Magnetic Materials, **323**(7) pp. 920-926.

[73] Bensebaa, F., Zavaliche, F., L'Ecuyer, P., 2004, "Microwave Synthesis and Characterization of Co–ferrite Nanoparticles," Journal of Colloid and Interface Science, **277**(1) pp. 104-110.

[74] Zi, Z., Sun, Y., Zhu, X., 2009, "Synthesis and Magnetic Properties of $CoFe_2O_4$ ferrite Nanoparticles," Journal of Magnetism and Magnetic Materials, **321**(9) pp. 1251-1255.

[75] Cedeño-Mattei, Y., Perales-Perez, O., Tomar, M., 2008, "Tuning of Magnetic Properties in Cobalt Ferrite Nanocrystals," Journal of Applied Physics, **103**(7) pp. 07E512-07E512-3.

[76] Jiao, Z., Geng, X., Wu, M., 2008, "Preparation of $CoFe_2O_4$ nanoparticles by Spraying Co-Precipitation and Structure Characterization," Colloids and Surfaces A: Physicochemical and Engineering Aspects, **313**pp. 31-34.

[77] Xiao, S. H., Jiang, W. F., Li, L. Y., 2007, "Low-Temperature Auto-Combustion Synthesis and Magnetic Properties of Cobalt Ferrite Nanopowder," Materials Chemistry and Physics, **106**(1) pp. 82-87.

[78] Maaz, K., Mumtaz, A., Hasanain, S., 2007, "Synthesis and Magnetic Properties of Cobalt Ferrite ($CoFe_2O_4$) Nanoparticles Prepared by Wet Chemical Route," Journal of Magnetism and Magnetic Materials, **308**(2) pp. 289-295.

[79] Lu, H., Zheng, W., and Jiang, Q., 2007, "Saturation Magnetization of Ferromagnetic and Ferrimagnetic Nanocrystals at Room Temperature," Journal of Physics D: Applied Physics, **40**(2) pp. 320.

[80] Kodama, R. H., Berkowitz, A. E., McNiff, J., EJ, 1996, "Surface Spin Disorder in $NiFe_2O_4$ nanoparticles," Physical Review Letters, **77**(2) pp. 394-397.

[81] Coey, J. M. D., 1971, "Noncollinear Spin Arrangement in Ultrafine Ferrimagnetic Crystallites," Physical Review Letters, **27**(17) pp. 1140-1142.

[82] Toksha, B., Shirsath, S. E., Patange, S., 2008, "Structural Investigations and Magnetic Properties of Cobalt Ferrite Nanoparticles Prepared by Sol–gel Auto Combustion Method," Solid State Communications, **147**(11) pp. 479-483.

[83] Zhao, L., Zhang, H., Xing, Y., 2008, "Studies on the Magnetism of Cobalt Ferrite Nanocrystals Synthesized by Hydrothermal Method," Journal of Solid State Chemistry, **181**(2) pp. 245-252.

[84] Tahar, L. B., Smiri, L., Artus, M., 2007, "Characterization and Magnetic Properties of Sm- and Gd-Substituted $CoFe_2O_4$ nanoparticles Prepared by Forced Hydrolysis in Polyol," Materials Research Bulletin, **42**(11) pp. 1888-1896.

[85] Gul, I., Amin, F., Abbasi, A., 2007, "Physical and Magnetic Characterization of Co-Precipitated Nanosize Co–Ni Ferrites," Scripta Materialia, **56**(6) pp. 497-500.

[86] Maaz, K., Karim, S., Mashiatullah, A., 2009, "Structural Analysis of Nickel Doped Cobalt Ferrite Nanoparticles Prepared by Coprecipitation Route," Physica B: Condensed Matter, **404**(21) pp. 3947-3951.

[87] Köseoğlu, Y., Alan, F., Tan, M., 2012, "Low Temperature Hydrothermal Synthesis and Characterization of Mn Doped Cobalt Ferrite Nanoparticles," Ceramics International, **38**(5) pp. 3625-3634.

[88] Köseoğlu, Y., Oleiwi Oleiwi, M. I., Yilgin, R., 2012, "Effect of Chromium Addition on the Structural, Morphological and Magnetic Properties of Nano-Crystalline Cobalt Ferrite System," Ceramics International, .

[89] Sharma, R. K., Suwalka, O., Lakshmi, N., 2005, "Synthesis of Chromium Substituted Nano Particles of Cobalt Zinc Ferrites by Coprecipitation," Materials Letters, **59**(27) pp. 3402-3405.

[90] Cojocariu, A. M., Soroceanu, M., Hrib, L., 2012, "Microstructure and Magnetic Properties of Substituted (Cr, Mn)-Cobalt Ferrite Nanoparticles," Materials Chemistry and Physics, .

[91] Duong, G., Hanh, N., Linh, D., 2007, "Monodispersed Nanocrystalline $Co_{1-x}Zn_xFe_2O_4$ particles by Forced Hydrolysis: Synthesis and Characterization," Journal of Magnetism and Magnetic Materials, **311**(1) pp. 46-50.

[92] Zhao, L., Yang, H., Zhao, X., 2006, "Magnetic Properties of $CoFe_2O_4$ ferrite Doped with Rare Earth Ion," Materials Letters, **60**(1) pp. 1-6.

[93] Parker, F. T., Foster, M. W., Margulies, D. T., 1993, "Spin Canting, Surface Magnetization, and Finite-Size Effects in γ-Fe_2O_3 particles," Physical Review B, **47**(13) pp. 7885-7891.

[94] Lin, D., Nunes, A., Majkrzak, C., 1995, "Polarized Neutron Study of the Magnetization Density Distribution within a $CoFe_2O_4$ colloidal Particle II," Journal of Magnetism and Magnetic Materials, **145**(3) pp. 343-348.

[95] Martínez, B., Obradors, X., Balcells, L., 1998, "Low Temperature Surface Spin-Glass Transition in γ-Fe_2O_3 nanoparticles," Physical Review Letters, **80**(1) pp. 181-184.

[96] Haneda, K., and Morrish, A., 1988, "Noncollinear Magnetic Structure of $CoFe_2O_4$ small Particles," Journal of Applied Physics, **63**(8) pp. 4258-4260.

[97] Concas, G., Spano, G., Cannas, C., 2009, "Inversion Degree and Saturation Magnetization of Different Nanocrystalline Cobalt Ferrites," Journal of Magnetism and Magnetic Materials, **321**(12) pp. 1893-1897.

[98] Moumen, N., and Pileni, M., 1996, "Control of the Size of Cobalt Ferrite Magnetic Fluid," The Journal of Physical Chemistry, **100**(5) pp. 1867-1873.

[99] Yáñez-Vilar, S., Sánchez-Andújar, M., Gómez-Aguirre, C., 2009, "A Simple Solvothermal Synthesis of MFe_2O_4 (M = Mn, Co and Ni) Nanoparticles," Journal of Solid State Chemistry, **182**(10) pp. 2685-2690.

[100] Rondinone, A. J., Samia, A., and Zhang, Z. J., 2000, "Characterizing the Magnetic Anisotropy Constant of Spinel Cobalt Ferrite Nanoparticles," Applied Physics Letters, **76**(24) pp. 3624-3626.

[101] Kim, Y. I., Kim, D., and Lee, C. S., 2003, "Synthesis and Characterization of $CoFe_2O_4$ magnetic Nanoparticles Prepared by Temperature-Controlled Coprecipitation Method," Physica B: Condensed Matter, **337**(1) pp. 42-51.

[102] Lerouge, F., Cerveau, G., and Corriu, R. J., 2006, "Supramolecular Self-Organization in Non-Crystalline Hybrid Organic–inorganic Nanomaterials Induced by Van Der Waals Interactions," New Journal of Chemistry, **30**(10) pp. 1364-1376.

[103] Jones, R.W., 1989, "Fundamental Principles of Sol-Gel Technology," The Institute of Metals, London, pp. 128.

[104] Corriu, R., and Trong Anh, N., 2009, "Molecular Chemistry of Sol-Gel Derived Nanomaterials," John Wiley & Sons, UK, .

[105] Brinker, C.J., and Scherer, G.W., 1990, "Sol-Gel Science : The physics and chemistry of sol-gel processing," Academic Press, San Diego, CA, .

[106] O'Brien, S., Brus, L., and Murray, C. B., 2001, "Synthesis of Monodisperse Nanoparticles of Barium Titanate: Toward a Generalized Strategy of Oxide Nanoparticle Synthesis," Journal of the American Chemical Society, **123**(48) pp. 12085-12086.

[107] Lee, J., Park, J. Y., and Kim, C. S., 1998, "Growth of Ultra-Fine Cobalt Ferrite Particles by a Sol–gel Method and their Magnetic Properties," Journal of Materials Science, **33**(15) pp. 3965-3968.

[108] Gopalan, E. V., Joy, P., Al-Omari, I., 2009, "On the Structural, Magnetic and Electrical Properties of Sol–gel Derived Nanosized Cobalt Ferrite," Journal of Alloys and Compounds, **485**(1) pp. 711-717.

[109] Gul, I., and Maqsood, A., 2008, "Structural, Magnetic and Electrical Properties of Cobalt Ferrites Prepared by the Sol–gel Route," Journal of Alloys and Compounds, **465**(1) pp. 227-231.

[110] Aghav, P., Dhage, V. N., Mane, M. L., 2011, "Effect of Aluminum Substitution on the Structural and Magnetic Properties of Cobalt Ferrite Synthesized by Sol–gel Auto Combustion Process," Physica B: Condensed Matter, **406**(23) pp. 4350-4354.

[111] Singhal, S., Jauhar, S., Singh, J., 2012, "Investigation of Structural, Magnetic, Electrical and Optical Properties of Chromium Substituted Cobalt Ferrites ($CoCr_xFe_{2-x}O_4$, $0 \leq X \leq 1$) Synthesized using Sol Gel Auto Combustion Method," Journal of Molecular Structure, **1012**pp. 182-188.

[112] Hashim, M., Kumar, S., Koo, B., 2012, "Structural, Electrical and Magnetic Properties of Co–Cu Ferrite Nanoparticles," Journal of Alloys and Compounds, **518**pp. 11-18.

[113] Kulal, S. R., Khetre, S. S., Jagdale, P. N., 2012, "Synthesis of Dy Doped Co-Zn Ferrite by Sol-Gel Auto Combustion Method and its Characterization," Materials Letters, .

[114] Sen, R., Das, G. C., and Mukherjee, S., 2010, "X-Ray Diffraction Line Profile Analysis of Nano-Sized Cobalt in Silica Matrix Synthesized by Sol–gel Method," Journal of Alloys and Compounds, **490**(1) pp. 515-523.

[115] Huang, X., and Chen, Z., 2004, "Sol–gel Preparation and Characterization of $CoFe_2O_4$–SiO_2 nanocomposites," Solid State Communications, **132**(12) pp. 845-850.

[116] Zhang, S., Dong, D., Sui, Y., 2006, "Preparation of Core Shell Particles Consisting of Cobalt Ferrite and Silica by Sol–gel Process," Journal of Alloys and Compounds, **415**(1) pp. 257-260.

[117] Silva, J. d., Diniz, C., Ardinson, J., 2004, "Cobalt Ferrite Dispersed in a Silica Matrix Prepared by Sol–gel Process," Journal of Magnetism and Magnetic Materials, **272**pp. E1851-E1853.

[118] Vejpravová, J., Plocek, J., Nižňanský, D., 2005, "Sol-gel fabricated $CoFe_2O_4/SiO_2$ nanocomposites: synthesis and magnetic properties," Magnetics Conference, 2005. INTERMAG Asia 2005. Digests of the IEEE International, Anonymous pp. 887-888.

[119] Cheng, F., Liao, C., Kuang, J., 1999, "Nanostructure Magneto-Optical Thin Films of Rare Earth (RE= Gd, Tb, Dy) Doped Cobalt Spinel by Sol–gel Synthesis," Journal of Applied Physics, **85**(5) pp. 2782-2786.

[120] Cheng, F., Peng, Z., Liao, C., 1998, "Chemical Synthesis and Magnetic Study of Nanocrystalline Thin Films of Cobalt Spinel Ferrites," Solid State Communications, **107**(9) pp. 471-476.

[121] Lee, E. K., Kim, W. S., Lee, K. W., 2009, "Enhanced Coercivity in Sponge Magnets with Three Dimensionally Ordered Nanopores," Solid State Communications, **149**(1) pp. 37-40.

[122] Kolar, D., 2000, "Chemical Research Needed to Improve High-Temperature Processing of Advanced Ceramic Materials (Technical Report)," Pure and Applied Chemistry, **72**(8) pp. 1425-1448.

[123] Mürbe, J., and Töpfer, J., 2006, "Ni-Cu-Zn Ferrites for Low Temperature Firing: II. Effects of Powder Morphology and Bi_2O_3 addition on Microstructure and Permeability," Journal of Electroceramics, **16**(3) pp. 199-205.

[124] Jean, J., Lee, C., and Kou, W., 1999, "Effects of Lead (II) Oxide on Processing and Properties of Low-Temperature-Cofirable Ni-Cu-Zn Ferrite," Journal of the American Ceramic Society, **82**(2) pp. 343-350.

[125] Hsu, J., Ko, W., Shen, H., 1994, "Low Temperature Fired NiCuZn Ferrite," Magnetics, IEEE Transactions On, **30**(6) pp. 4875-4877.

[126] Barba, A., Clausell, C., Felíu, C., 2004, "Sintering of $(Cu_{0.25}Ni_{0.25}Zn_{0.50})Fe_2O_4$ ferrite," Journal of the American Ceramic Society, **87**(4) pp. 571-577.

[127] Chen, I., and Wang, X., 2000, "Sintering Dense Nanocrystalline Ceramics without Final-Stage Grain Growth," Nature, **404**(6774) pp. 168-171.

[128] Kumar, A., Watabe, M., and Kurokawa, K., 2011, "The Sintering Kinetics of Ultrafine Tungsten Carbide Powders," Ceramics International, **37**(7) pp. 2643-2654.

[129] Nlebedim, I., Ranvah, N., Williams, P., 2009, "Influence of Vacuum Sintering on Microstructure and Magnetic Properties of Magnetostrictive Cobalt Ferrite," Journal of Magnetism and Magnetic Materials, **321**(17) pp. 2528-2532.

[130] Oubaha, M., Etienne, P., Calas, S., 2005, "Sol–Gel Derived Organic and Inorganic Hybrid Materials for Photonic Applications: Contribution to the Correlation between the Material Structure and the Transmission in the Near Infrared Region," Journal of Sol-Gel Science and Technology, **33**(2) pp. 241-248.

[131] Varma, P., Colreavy, J., Cassidy, J., 2009, "Effect of Organic Chelates on the Performance of Hybrid Sol–gel Coated AA 2024-T3 Aluminium Alloys," Progress in Organic Coatings, **66**(4) pp. 406-411.

[132] George, M., Nair, S. S., John, A. M., 2006, "Structural, Magnetic and Electrical Properties of the Sol-Gel Prepared $Li_{0.5}Fe_{2.5}O_4$ fine Particles," Journal of Physics D: Applied Physics, **39**(5) pp. 900.

[133] Ding, J., McCormick, P., and Street, R., 1995, "Magnetic Properties of Mechanically Alloyed $CoFe_2O_4$," Solid State Communications, **95**(1) pp. 31-33.

[134] Berkowitz, A., and Schuele, W., 1959, "Magnetic Properties of some Ferrite Micropowders," Journal of Applied Physics, **30**pp. S134.

[135] Grigorova, M., Blythe, H., Blaskov, V., 1998, "Magnetic Properties and Mössbauer Spectra of Nanosized $CoFe_2O_4$ powders," Journal of Magnetism and Magnetic Materials, **183**(1) pp. 163-172.

[136] Benyounis, K. Y., Olabi, A. G., and Hashmi, M. S. J., 2008, "Multi-Response Optimization of CO_2 laser-Welding Process of Austenitic Stainless Steel," Optics & Laser Technology, **40**(1) pp. 76-87.

[137] Olabi, A., Benyounis, K., and Hashmi, M., 2007, "Application of Response Surface Methodology in Describing the Residual Stress Distribution in CO_2 laser Welding of AISI304," Strain, **43**(1) pp. 37-46.

[138] Benyounis, K., and Olabi, A., 2008, "Optimization of Different Welding Processes using Statistical and Numerical approaches–A Reference Guide," Advances in Engineering Software, **39**(6) pp. 483-496.

[139] Montgomery, D.C., 1984, "Design and analysis of experiments, 2nd Edition," John Wiley & Sons, New York, pp. 538.

[140] Khuri, A.I., and Cornell, J.A., 1996, "Response Surfaces: Designs and Analyses, 2nd Edition," Marcel Dekker Incorporated, New York, pp. 510.

[141] Myers, R.H., and Montgomery, D.C., 1995, "Response surface methodology: process and product optimization using designed experiments," John Wiley & Sons, New York, pp. 700.

[142] Design-Expert Software, 2000, "User's Guide, Technical Manual," Stat-Ease Inc., Minneapolis, MN, **7**.

[143] Silva, J. B., Brito, W. d., and Mohallem, N. D., 2004, "Influence of Heat Treatment on Cobalt Ferrite Ceramic Powders," Materials Science and Engineering: B, **112**(2) pp. 182-187.

[144] Sunde, T. O. L., Einarsrud, M., and Grande, T., 2013, "Solid State Sintering of Nano-Crystalline Indium Tin Oxide," Journal of the European Ceramic Society, **33**pp. 565-574.

[145] McColm, I.J., and Clark, N.J., 1988, "Forming, shaping, and working of high performance ceramics," Blackie, Glasgow, pp. 345.

Appendix A

Scientific Achievements

Peer Reviewed Journal Articles:

- **M. Sajjia**, M. Oubaha, T. Prescott, A.G. Olabi, Development of cobalt ferrite powder preparation employing the sol–gel technique and its structural characterisation, Journal of Alloys and Compounds 506 (2010) 400–406
- **M. Sajjia**, K.Y. Benyounis, A.G. Olabi, The simulation and optimisation of heat treatment of cobalt ferrite nanoparticles prepared by the sol–gel technique, Powder Technology 222 (2012) 143–151
- M. Hasanuzzman, **M. Sajjia**, A. G. Olabi, Thermal behaviour of Zircon/ Zirconia added chemically durable borosilicate porous glass, Thermochimica Acta, 2012, accepted

Peer Reviewed Journal Articles under Progress:

- M. Sajjia, M. Oubaha, M. Hasanuzzaman, A.G. Olabi, Structural and magnetic analyses of developed cobalt ferrite nanoparticles prepared by the sol-gel process, 2013, under review
- M. Sajjia, M. Hasanuzzaman, A.G. Olabi, Review paper: Cobalt ferrite, the magnetostrictive material; the preparation by chemical methods; the structural and magnetic characterisations, 2013, submitted
- M. Sajjia, A.G. Olabi, The sintering behaviour of cobalt ferrite nanoparticles, 2013, being written

Conference Proceedings:

- Structural characterisation of cobalt ferrite nanoparticles, Workshop & International Conference on Smart Materials "WICSM2010" 22/09/2010 until 24/09/2010 in Ireland
- Cobalt ferrite nanoparticles, the mutual relation between morphology and synthesis parameters, Powder Metallurgy World Congress & Exhibition "PM2010" 10/10/2010 until 14/10/2010 in Italy
- Heat treatment of cobalt ferrite powder prepared by the sol-gel method, The 15th European Conference on Composite Materials "ECCM15" 24/06/2012 until 28/06/2012 in Italy

Symposiums:

- The internal conference held at the School of Mechanical and Manufacturing Engineering, DCU in 29/05/2008
- Symposium for mechanical engineering research and practice 2009 held at the School of Mechanical and Manufacturing Engineering, DCU in 28/05/2009
- The internal conference held at the School of Mechanical and Manufacturing Engineering, DCU in 12/05/2011
- Faculty Research Day 2012 held at the School of Mechanical and Manufacturing Engineering, DCU in 12/09/2012

Involvements:

- Attended Powder Metallurgy training course from 21/06/2008 until 29/06/2008 in Italy
- Participated in preparation of the 3rd International Conference on Sustainable Energy & Environmental Protection (SEEP 2009) which was held at the School of Mechanical and Manufacturing Engineering, DCU from 12/8/2009 until 15/8/2009
- Was assigned as a member in the organising committee for the Workshop & International Conference on Smart Materials "WICSM2010" which was held at the School of Mechanical and Manufacturing Engineering, DCU from 22/09/2010 until 24/09/2010
- One of his research papers got the second best at Young Engineers Paper Prize Competition, Engineers Ireland. It was presented at a joint meeting of members of Engineers Ireland and Institution of Mechanical Engineers in 07/06/2011
- Was assigned as a member in the organising committee of the 5th International Conference on Sustainable Energy & Environmental Protection (SEEP 2012) which was held at the School of Mechanical and Manufacturing Engineering, DCU from 05/06/2012 until 08/06/2012

Appendix B

Density of water as a function of temperature

When measuring density of sintered disc samples employing Archimedes Method Kit, the temperature of water was measured in the beginning and in the end of the experiment. The mean temperature was calculated and the respective density was taken from the following table. This density was needed to calculate the density of disc samples using the equation stated in Chapter 3. The following table includes density of water at a range of different temperatures (10 to 30 °C).

Density of H_2O at Temperature T (in °C)

T/°C	0.0	0.1	0.2	0.3	0.4	0.5	0.6	0.7	0.8	0.9
10.	0.99973	0.99972	0.99971	0.99970	0.99969	0.99968	0.99967	0.99966	0.99965	0.99964
11.	0.99963	0.99962	0.99961	0.99960	0.99959	0.99958	0.99957	0.99956	0.99955	0.99954
12.	0.99953	0.99951	0.99950	0.99949	0.99948	0.99947	0.99946	0.99944	0.99943	0.99942
13.	0.99941	0.99939	0.99938	0.99937	0.99935	0.99934	0.99933	0.99931	0.99930	0.99929
14.	0.99927	0.99926	0.99924	0.99923	0.99922	0.99920	0.99919	0.99917	0.99916	0.99914
15.	0.99913	0.99911	0.99910	0.99908	0.99907	0.99905	0.99904	0.99902	0.99900	0.99899
16.	0.99897	0.99896	0.99894	0.99892	0.99891	0.99889	0.99887	0.99885	0.99884	0.99882
17.	0.99880	0.99879	0.99877	0.99875	0.99873	0.99871	0.99870	0.99868	0.99866	0.99864
18.	0.99862	0.99860	0.99859	0.99857	0.99855	0.99853	0.99851	0.99849	0.99847	0.99845
19.	0.99843	0.99841	0.99839	0.99837	0.99835	0.99833	0.99831	0.99829	0.99827	0.99825
20.	0.99823	0.99821	0.99819	0.99817	0.99815	0.99813	0.99811	0.99808	0.99806	0.99804
21.	0.99802	0.99800	0.99798	0.99795	0.99793	0.99791	0.99789	0.99786	0.99784	0.99782
22.	0.99780	0.99777	0.99775	0.99773	0.99771	0.99768	0.99766	0.99764	0.99761	0.99759
23.	0.99756	0.99754	0.99752	0.99749	0.99747	0.99744	0.99742	0.99740	0.99737	0.99735
24.	0.99732	0.99730	0.99727	0.99725	0.99722	0.99720	0.99717	0.99715	0.99712	0.99710
25.	0.99707	0.99704	0.99702	0.99699	0.99697	0.99694	0.99691	0.99689	0.99686	0.99684
26.	0.99681	0.99678	0.99676	0.99673	0.99670	0.99668	0.99665	0.99662	0.99659	0.99657
27.	0.99654	0.99651	0.99648	0.99646	0.99643	0.99640	0.99637	0.99634	0.99632	0.99629
28.	0.99626	0.99623	0.99620	0.99617	0.99614	0.99612	0.99609	0.99606	0.99603	0.99600
29.	0.99597	0.99594	0.99591	0.99588	0.99585	0.99582	0.99579	0.99576	0.99573	0.99570
30.	0.99567	0.99564	0.99561	0.99558	0.99555	0.99552	0.99549	0.99546	0.99543	0.99540

Appendix C

The preparation of cobalt ferrite employing oxides, validation of results

Cobalt ferrite was prepared by firing mixed (Cobalt Oxide, CoO, Sigma-Aldrich) and (Iron(III) Oxides, Fe_2O_3, Sigma-Aldrich) powders in air at 1000 °C. Both precursors were initially dispersed in de-ionised water as an interface. Using a magnetic stirrer, resultant reactant was left constantly stirring for 24 hours to allow for a very homogeneous mixture. The colour of the mixture was sepia. The mixture was dried afterwards at 110 °C for 8 hours and ground later on using a mortar and pestle. The resultant sample of powder was subjected to a heat treatment in a Horizontal Tube Furnace (Carbolite Ltd., Sheffield, UK) at 1000 °C for 72 hours.

This experiment was done to validate the results obtained from the literature [6] and to approve the legitimacy of the XRD results obtained from other chemical experiments. The XRD pattern of the resultant powder showed a complete conversion of both oxides into cobalt ferrite as shown in the following Figure.

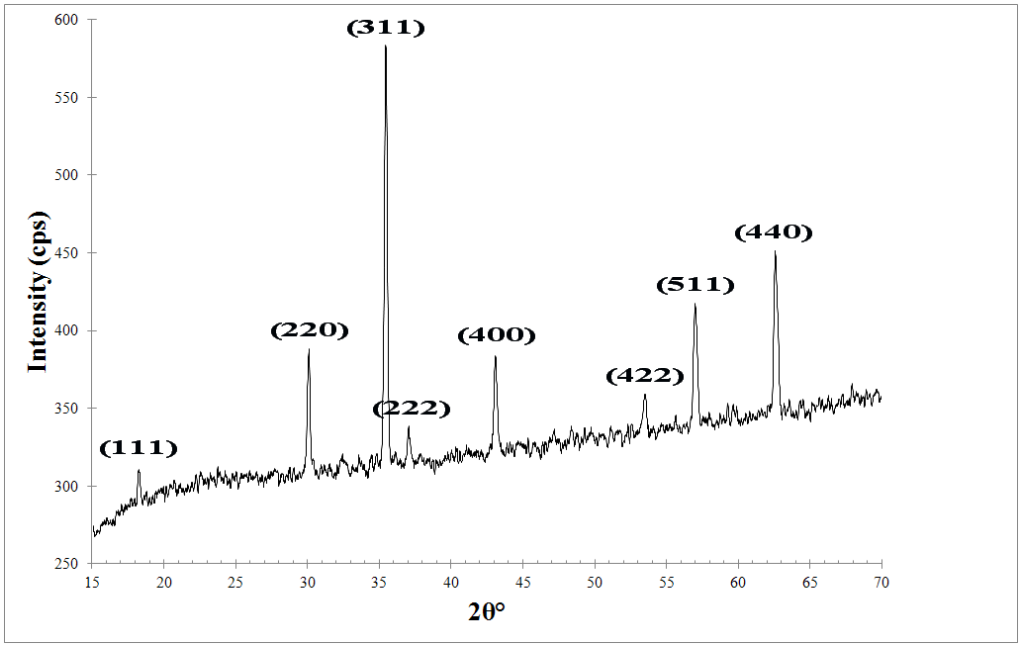

Appendix D

Energy dispersive X-ray analysis

Cobalt ferrite powder EDX Analysis

Spectrum processing:

No peaks omitted

Processing option: All elements analysed (Normalised)

Element	Weight%	Atomic%
O K	24.76	54.16
Fe K	49.42	30.47
Co K	25.82	15.37
Totals	100.00	

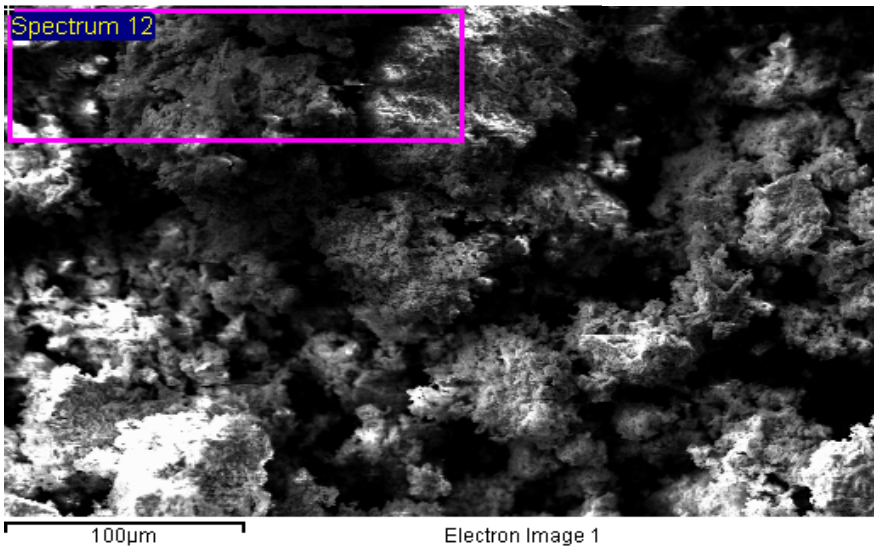

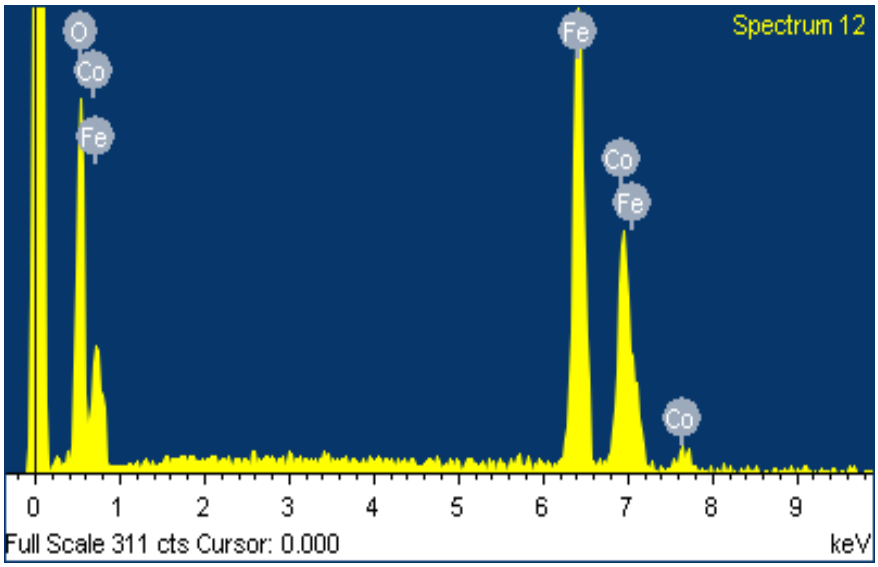

Comment: No other elements were detected.

Appendix E

Density of cobalt ferrite nanoparticles measured using two different helium gas Pycnometer

The density of cobalt ferrite nanoparticles was measured using (AccuPyc 1330 V1.02) helium gas pycnometer at the University Laboratory. The density value of 4.93 g/cm^3 was recorded. The following two Figures show the calibration report and obtained results:

AccuPyc 1330 V1.02
Serial Number: 393
Calibration Report

Volume of Calibration Standard: 6.3722 cc
Number of Purges: 10 Equilibration Rate: 0.0050 psig/min

Run Pair#	Cell Volume cc	Deviation cc	Expansion Volume cc	Deviation cc
1	12.1223	0.0046	8.4578	0.0019
2	12.1239	0.0061	8.4612	0.0054
3	12.1192	0.0014	8.4563	0.0004
4	12.1195	0.0018	8.4572	0.0013
5	12.1181	0.0003	8.4565	0.0006
6	12.1174	-0.0003	8.4567	0.0008
7	12.1158	-0.0019	8.4548	-0.0011
8	12.1142	-0.0035	8.4530	-0.0029
9	12.1140	-0.0037	8.4533	-0.0026
10	12.1129	-0.0048	8.4520	-0.0039

Average Cell Volume: 12.1177 cc Standard Deviation: 0.0036 cc
Average Expansion Volume: 8.4559 cc Standard Deviation: 0.0027 cc

AccuPyc 1330 V1.02
Serial Number: 393
Density and Volume Report

Sample ID: 1111
Number of Purges: 25
Cell Volume: 12.1177 cc
Sample Weight: 3.1427 g
Equilibration Rate: 0.0050 psig/min
Expansion Volume: 8.4559 cc

Run#	Volume cc	Deviation cc	Density g/cc	Deviation g/cc
1	0.6401	0.0026	4.9095	-0.0197
2	0.6361	-0.0014	4.9403	0.0110
3	0.6371	-0.0005	4.9331	0.0039
4	0.6369	-0.0007	4.9347	0.0055
5	0.6376	0.0001	4.9286	-0.0006

Average Volume: 0.6376 cc Standard Deviation: 0.0015 cc
Average Density: 4.9293 g/cc Standard Deviation: 0.0118 g/cc

The same sample of nanoparticles was sent outside the University Laboratory in order to measure its density. The density was measured using (AccuPycII 1340 V1.05) helium gas pycnometer. A value of 4.95 g/cm^3 was recorded. The following Figures show the calibration report and the obtained results:

AccuPycII 1340 V1.05
Serial Number: 2214
Calibration Report

Started: 14/11/12 13:05:39 Completed: 14/11/12 13:31:19
Temperature: 20.3 °C
Volume of Calibration Standard: 6.371499 cm3
Number of Purges: 10 Equilibration Rate: 0.0050 psig/min

Cycle#	Cell Volume cm3	Deviation cm3	Expansion Volume cm3	Deviation cm3
1	11.7356	0.0021	8.4853	0.0015
2	11.7337	0.0002	8.4839	0.0001
3	11.7343	0.0008	8.4844	0.0006
4	11.7334	-0.0000	8.4838	-0.0000
5	11.7334	-0.0001	8.4837	-0.0001
6	11.7325	-0.0009	8.4831	-0.0007
7	11.7339	0.0004	8.4841	0.0003
8	11.7337	0.0002	8.4840	0.0001
9	11.7320	-0.0014	8.4828	-0.0010
10	11.7323	-0.0012	8.4830	-0.0008

Average Offset: 0.0029 cm3 Standard Deviation: 0.0008 cm3
Average Scale Factor: 0.9993 Standard Deviation: 0.0001
Average Cell Volume: 11.7335 cm3 Standard Deviation: 0.0010 cm3
Average Expansion Volume: 8.4838 cm3 Standard Deviation: 0.0007 cm3

AccuPycII 1340 V1.05
Serial Number: 2214
Density and Volume Report

Sample ID: black powder 01 Started: 14/11/12 13:58:58
Sample Mass: 4.4848 g Completed: 14/11/12 14:35:05
Temperature: 20.3 °C
Number of Purges: 25 Equilibration Rate: 0.0050 psig/min
Cell Volume: 11.7330 cm3 Expansion Volume: 8.4838 cm3

Cycle#	Volume cm3	Deviation cm3	Density g/cm3	Deviation g/cm3	Elapsed Time	Temperature °C
1	0.9053	-0.0009	4.9540	0.0048	0:22:25	20.2
2	0.9060	-0.0002	4.9502	0.0009	0:25:58	20.2
3	0.9065	0.0004	4.9472	-0.0020	0:29:24	20.2
4	0.9061	-0.0001	4.9496	0.0003	0:32:41	20.2
5	0.9069	0.0007	4.9454	-0.0039	0:35:58	20.3

Average Volume: 0.9062 cm3 Standard Deviation: 0.0005 cm3
Average Density: 4.9493 g/cm3 Standard Deviation: 0.0029 g/cm3